PROBING NANOSCALE ADHESION AND STRUCTURE AT SOFT INTERFACES

By

Kenneth Patrick Ritchie

B. Sc. (Physics) University of Waterloo

M. Sc. (Physics) University of Waterloo

A THESIS SUBMITTED IN PARTIAL FULFILLMENT OF

THE REQUIREMENTS FOR THE DEGREE OF

DOCTOR OF PHILOSOPHY

in

THE FACULTY OF GRADUATE STUDIES

PHYSICS

We accept this thesis as conforming

to the required standard

THE UNIVERSITY OF BRITISH COLUMBIA

September, 1998

© Kenneth Patrick Ritchie, 1998

In presenting this thesis in partial fulfilment of the requirements for an advanced degree at the University of British Columbia, I agree that the Library shall make it freely available for reference and study. I further agree that permission for extensive copying of this thesis for scholarly purposes may be granted by the head of my department or by his or her representatives. It is understood that copying or publication of this thesis for financial gain shall not be allowed without my written permission.

Physics
The University of British Columbia
2075 Wesbrook Place
Vancouver, Canada
V6T 1Z1

Date: Sept. 11, 1998

Abstract

Physical measurement at soft interfaces presents special problems. The compliance of the interface makes positional accuracy of secondary importance to force sensitivity. Only minuscule forces are required to displace a soft surface or to slowly overcome a small energetic barrier in an aqueous environment. The thesis is organized according to three aspects of measurement at soft interfaces and the parts are labelled by Roman numerals I–III. Each of these parts (I–III) contains results conclusions and discussions specific to the particular topic of the segment.

I) To test adhesion and probe compliance at soft interfaces, the developement of a general, ultra-sensitive force measurement technique is described. The technique exploits a tunable force transducer comprised of a biomembrane capsule held under tension chemically bonded to a glass microsphere probe. The technique has a high sensitivity (in the range of pico- to nano-Newtons) and a large span of force loading rates.

II) To demonstrate nanoscale mechanical testing of interfacial compliance, the ultra-sensitive force probe was used to determine the thickness compressibility of the human red blood cell membrane. The membrane was found to be 100-fold softer than an ideal rubber. The minimum thickness of the red cell membrane was 58 ± 4 nm. This thickness implies that there are large proteins associated with the membrane that act to expand the tethered spectrin network.

III) To demonstrate nanoscale testing of molecular adhesive strength, the probe has been used to rupture single receptor-ligand bonds (avidin-biotin). Recognizing that thermal activation underlies dissociation of weak bonds, a theory for the force-driven failure

of point physical bonds is presented. The predictions from theory are verified by Brownian dynamics simulation. Bond failure is a kinetic process. The experimentally measured strength of the bond depends on the rate which force is applied to the linkage. A universal logarithmic rate dependence regime reveals information about the underlying bonding potential along the force-driven reaction pathway. The form of the strength over a spectrum of loading rates gives the position and height of major energetic barriers along the bond failure pathway. Complex bonding potentials can thus be partially reconstructed and compared to the structures of the bonding species, if available.

Table of Contents

Abstract ii

List of Tables vii

List of Figures viii

Acknowledgement x

Dedication xi

1 General Introduction 1

I Ultra-sensitive Force Measurement Technique Design 3

2 Introduction 4

3 The Force Transducer/Probe Assembly 7

4 Vertical Instrument Design 12

4.1 Transducer Translation and Probe Position Sensor 12

4.2 The Complete Assembly 15

5 Horizontal Mode Instrumentation 18

5.1 Microsphere Probe Tracking 20

5.2 The Complete Setup 20

5.3 Fast Frame Rate Version 23

6 Summary 25

II Nanoscale Compliance of Soft Interfaces 26

7 Introduction 27

8 Methods 31

8.1 Probe Preparation 31

8.1.1 Cleaning of Microspheres 31

8.1.2 Silanization 31

8.1.3 Attachment of Biotin 32

8.1.4 Avidin Conjugation 32

8.2 Preparation of Transducer 33

8.3 Sample Preparation — Ghosting 33

8.4 Compression Measurement Protocol 34

9 Results and Discussion 35

9.1 Membrane Thickness 38

9.2 Membrane Compressibility 39

III Strength of Molecular Surface Bonds 45

10 Experimental Bond Strength Measurement 46

11 Introduction to Bond Strength Analysis 52

12 Dissociation of Single Bonds 55

12.1 Inverse Power Law Potential 60

12.2 Harmonic Well Potential 62
12.3 Effect of a Linear Loading Rate 64

13 Computational Experiments **67**
13.1 Monte Carlo Methods 67
13.1.1 The Metropolis Method 67
13.1.2 The Smart Monte Carlo Method 69
13.1.3 Computational Single Bond Failure under Ramped Force 72
13.2 Results 75
13.3 Discussion 81
13.4 Small-Number-of-Atom Simulation 84

14 Multiple Bond Failure **94**
14.1 Serial Loading — Serial Failure 95
14.1.1 Molecular Switch 96
14.2 Parallel Loading — Random Deletion 102
14.3 Parallel Loading — Sequential Failure 102
14.4 Summary 104

15 Conclusions **107**

Bibliography **109**

List of Tables

13.1 Intrinsic Force 79

List of Figures

3.1 Force Transducer/Probe Assembly 8

3.2 Mean Square Fluctuations of Probe 10

4.3 Pattern Generation in RICM 13

4.4 The Complete Vertical Assembly 16

5.5 Schematic of Horizontal Apparatus 19

5.6 Image from Horizontal Apparatus 21

5.7 Complete Horizontal Apparatus 22

7.8 Cartoon of the Red Cell Membrane 28

7.9 Schematic of the Compression Test 30

9.10 Compression Cycle for Two Single Washed Ghosts 36

9.11 Compression Cycle for Two Triple Washed Ghosts 37

9.12 The Hertz Model 40

9.13 The Network of Springs Model 43

10.14Experimental Approach and Retraction Trajectories in Tests of Bond Strength 48

10.15Experimental Bond Strength Histogram 50

10.16Bond Strength Spectrum 51

12.17Energy Landscape of a Bound System 57

12.18Effect of Applied Load on the Energy Landscape 58

12.19Theoretical Probability Density for Bond Rupture Strength 65

13.20Flowchart of the SMC Algorithm 71
13.21Comparison of Last to First Passage Time 74
13.22Force Histograms from Computational Experiments 76
13.23Apparent Offrate for Driven Dissociation 78
13.24Strength of the Inverse Power Law Bond 80
13.25Comparison of Strength Between the Inverse Power Law and Harmonic Well Bond 82
13.26Strength of Inverse Power Law Bond in Three Dimensions 83
13.27Potential Energy Profile for the Avidin-biotin System 86
13.28Geometry of Extended Simulation 88
13.29Renormalization of Potential by Fluctuations 89
13.30Randomly Selected Configuration Potentials 90
13.31Comparison of Strength at Frozen and Finite Temperatures 92

14.32Strength Probability Density for Failure of Serial Bonds 97
14.33Strength of a Molecular Switch 98
14.34Strength Probability Density for a Molecular Switch 100
14.35Phase Diagram of the Molecular Switch 101
14.36Parallel Failure of a Field of Bonds 103
14.37Sequential Failure of a Field of Bonds 105

Acknowledgement

I would like to thank Dr. Evan Evans, for his support and guidance. He has been a great supervisor and friend. I hope to have gained some of his vast insight into physics during my brief stay in his laboratory.

I would also like thank my supervisory committee for their scholarly help: Dr. Thomas Tiedje, Dr. Myer Bloom and Dr. David Boal.

I am indebted to all the members of the lab, throughout my stay, for their help, especially: Andrew Leung, a friend and confidant; Wieslawa Rawicz, who brightens up the lab by just being there; Pierre Nassoy, Kendo 1-kyu, who was of great support in the finishing years (and who knows great wine); Hans-Günther Döbereiner who's scientific method was (and is) inspiring (and who knows great beer); Tony Yeung for his support (and his gossip); and Mike Mitton for helping with the early MC work (*Hey Guido, it's all so clear to me now*).

I must also thank my kendo teachers, Hiro Okusa and David Harding, and my Soto-shu Zen teacher, Hosaka-sensei, for showing me a more philisophical (dynamic and static) side of life.

Finally, I thank my wife, Sayuri, for always being there when I needed her.

Dedication

I dedicate

this thesis to my mother,

Marion Ritchie

Chapter 1

General Introduction

Interfacial physics is of great interest in many fields of research. The most obvious examples come from hard condensed matter. The fabrication of modern solid state devices requires extensive knowledge of interfacial roughness, surface electronic states and surface structure. The performance of the solid state device is directly related to the surface structure. Hence much research has been done in the modern era on hard interfaces.

A recent and important field of interfacial research involves soft condensed matter. Soft condensed matter is usually associated with a non-crystalline (or liquid crystalline) surface with a soft mechanical compliance. Specific examples include polymer grafted surfaces, liquid interfaces, and biological (living) cells. The area of soft interfacial research has opened up new horizons for device fabrication as well as a deeper understanding of biological and polymeric media.

In general, soft interfaces are thermally roughened causing an ambiguity to the position of the interface not present in hard materials. Binding energies in weak adhesion are also on the order of the thermal energy. Thermal energy at room temperature, k_BT ($= 1/40$ eV), is the important energetic scale in soft matter. For interactions that range over nanometers, forces of $k_BT/1$ nm ~ 4 pN are expected.

First, a general force measurement apparatus was developed to experimentally study bond failure and perform nano-mechanical testing at surfaces. The development and implementation of two related instruments to perform ultra-sensitive force measurement

at soft interfaces is presented here.

In the next sections, demonstrations of the general force probe instrument is given. Local compliance measurements were performed on a complex soft interface (the human red blood cell membrane) and the strength of a point-adhesive bond was probed. A thorough analysis of force-driven, point-adhesive failure in an overdamped environment is given with the last section including verification of the analysis through a Brownian dynamics simulation.

Thus a complete method for the study of soft interfaces is presented. The methods and approaches followed in this thesis are not limited to the examples present here but are applicable to a wide range of interesting problems. The examples here are specific applications to biological substrates.

Part I

Ultra-sensitive Force Measurement Technique Design

Chapter 2

Introduction

Experimental determination of adhesive strength and surface compliance requires a technique that has a high level of force sensitivity and can span several orders of magnitude in loading rate. This section describes two related experimental techniques developed to perform ultra-sensitive force measurements at interfaces in aqueous solution. The experimental techniques form a general force measurement apparatus that can be applied to many problems.

The level of sensitivity required to measure forces at soft interfaces can be estimated. The important energy scale to displace a soft interface or disrupt a weak bond is the thermal energy, k_BT, where k_B is the Boltzmann constant and T is the absolute temperature ($k_BT = 4 \times 10^{-21}\text{J} = 4$ pN $\cdot$ nm at room temperature). As a lower bound of force sensitivity, a probe must apply force over a length scale of Angstroms to overcome energy barriers of the thermal energy. Thus a piconewton-level force sensitivity is required to accurately probe a soft interface. Experimentally, forces in the piconewton range have recently been measured in biological systems. For example, the force required to rupture a non-covalent biochemical linkage has been reported in the 10's–100's of piconewton range (Evans *et. al.*, 1991; Florin *et al.*, 1994; Lee *et al.*, 1994; Moy *et al.*, 1994; Williams *et al.*, 1996; Merkel *et al.*, 1998). Further, the force required to rupture a single hydrogen bond was reported as 10 pN (Hoh *et al.*, 1992). Myosin and kinesin molecular motors generate forces in the piconewton range (Ashkin *et al.*, 1990; Ishijima *et al.*, 1991; Kuo and Sheetz, 1993). Although a force sensitivity of piconewtons is required, forces can

range to near nanonewton levels and a force probe must be able to span this range to be effective.

At soft surfaces, interfacial roughness lowers expectations of positional accuracy normal to the surface. Thermal fluctuation of a soft interface sets the level of positional resolution required to nanometer-level resolution.

Instrumental design, to achieve piconewton-level force resolution, has its roots in a mechanical technique that stand out in the realm of force measurement at surfaces, the atomic force microscope (AFM) (Binnig *et al.*, 1986). The AFM technique depends on the detection of the deflection of a spring to measure applied force. The AFM uses a microfabricated cantilever that has a spring constant as low as 50 pN/nm (1 pN/nm $\equiv$ 1 mN/m). Precise measurement of cantilever deflection by laser reflection or interferometry allows for accurate force measurement. The instrument described here was designed to have an increased force sensitivity. The positional accuracy is lower than that of the Angstrom resolution AFM, the nanometer resolution is high enough for measurement at soft interfaces.

In our present design, the microfabricated cantilever of the AFM is replaced by a biomembrane-capsule force-transducer like a human red blood cell (RBC). A surface probe is formed from a glass microsphere biochemically *glued* to the capsule membrane. Pressurized into a spherical form by pipet aspiration of the capsule, the membrane tension sets the spring constant of the transducer. Displacement of the microsphere normal to the capsule surface is proportional to applied force. Surprisingly, the stiffness of the RBC capsule can be controlled over nearly two orders-of-magnitude at a level as much as 1000 fold lower than that of the common AFM cantilever.

The design elements required for accurate control of the force probe are precise control of the transducer position and detection of the probe position in real time. These elements are implemented in two related versions of the force measurement apparatus:

1) a vertical version with a high positional accuracy and 2) a horizontal version with greater versatility and a higher temporal resolution. Each version exploits the use of the tunable biomembrane-capsule force-transducer. Such control allows precise application of force over a wide dynamic range of force loading rates. The rates at which force can be applied range from 0.1 pN/s to upwards of 50,000 pN/s. This wide range of accessible force loading rates opens the ability to perform dynamical studies in force measurement.

Chapter 3

The Force Transducer/Probe Assembly

The spring transducer element of both versions of the force probe technique is the force-transducer/probe assembly shown in figure 3.1. The base is a glass micropipet that is driven along its symmetry axis to/from a test surface. A human red blood cell is held in the open mouth of the micropipet under sufficient suction pressure to make the cell into a smooth sphere. The pressure is precisely controlled between 1 μatm and 0.1 atm by a micrometer-driven water manometer or piston syringe. A glass microsphere is *glued* biochemically to the pole opposite the holding pipet on the capsule surface[1].

Along the axis of symmetry, the transducer behaves as a one-dimensional harmonic spring under small displacements of the probe. As such, a spring constant k characterizes the response of the transducer to force through $f = k \cdot \delta$. For small displacements, a red blood cell capsule, swollen to a nearly spherical geometry as in figure 3.1 has a stiffness given by (Evans *et al.*, 1991)

$$k = \tau \cdot 2\pi / \log(4R_O^2/R_C R_P) \tag{3.1}$$

where R_O is the equatorial radius of the RBC transducer, R_C is the radius of contact between the microsphere-probe and the RBC transducer and R_P is the inside radius of the pipet. The stiffness of the transducer depends directly on the isotropic tension τ characteristic of a fluid membrane. Since the red cell membrane possesses a small

[1]The current biochemical *glue* consists of bridging the protein avidin between biotin terminated polymers covalently bonded to the probe and red cell transducer surfaces. For more details see chapter 8 in Part II and Nassoy *et al.*, 1998.

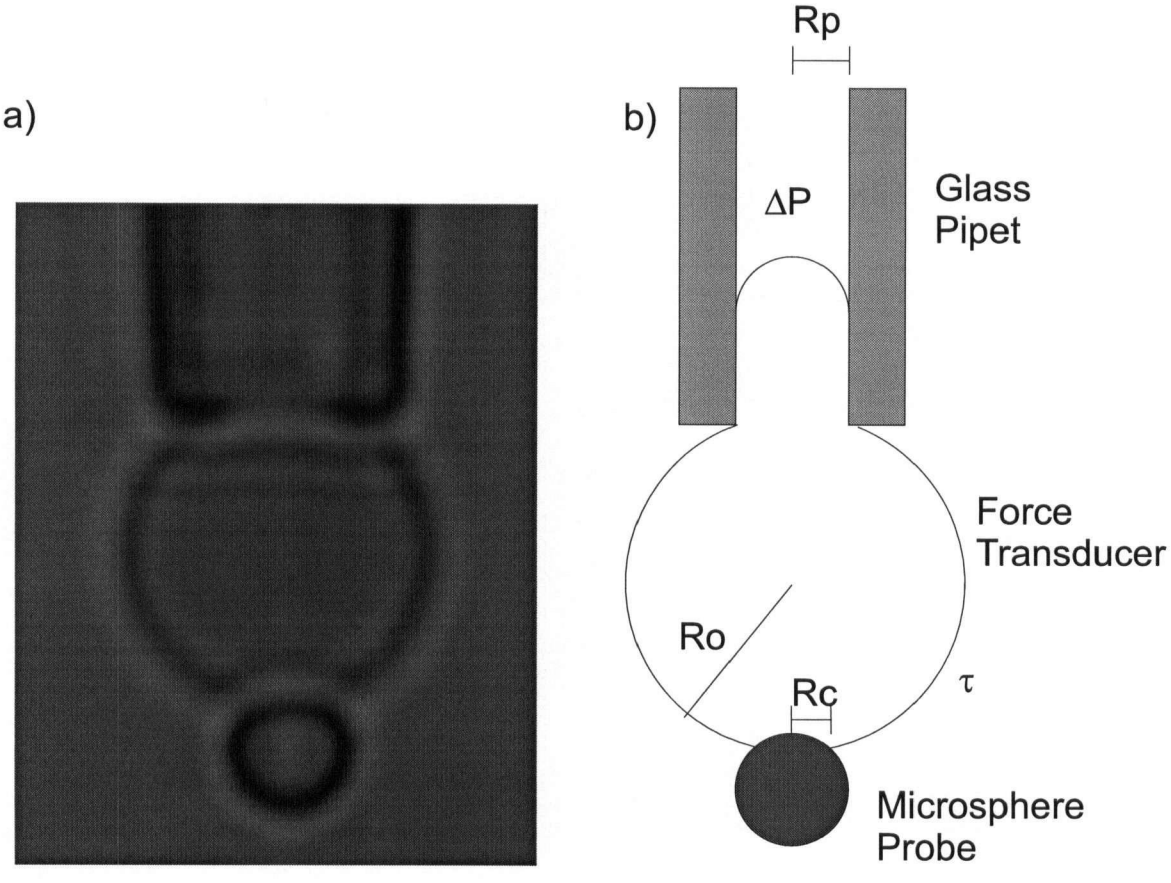

Figure 3.1: Force Transducer/Probe Assembly.
a) Bright-field image and b) schematic of the force transducer/probe assembly. A glass pipet of radius $R_P \sim 1\mu$m holds the membrane transducer of radius $R_O \sim 3\mu$m under suction pressure ΔP. The probe contacts the transducer over a radius of $R_C \sim 1\mu$m along the symmetry axis. Note: the dark borders around the cell, pipet entrance, and glass microsphere are due to diffraction with a width of $\sim 0.5\mu$m.

surface shear rigidity, μ, the transducer cell must be pressurized to an extent where $\tau \gg \mu$ ($\sim 10^{-2}$ mN/m (Waugh and Evans, 1979)), which is demonstrated clearly by the spherical shape outside the pipet in figure 3.1. The tension in the capsule-membrane is set by the suction pressure ΔP through (Evans and Skalak, 1980)

$$\tau = \frac{\Delta P \cdot R_P}{2(1 - R_P/R_O)} \tag{3.2}$$

The suction pressure, ΔP is experimentally controlled over a range of 0.5 – 15 mAtm (0.05–1.5 kPa). Using typical values for the geometric parameters ($R_0 \approx 3\mu$m, $R_C \approx 1\mu$m and $R_P \approx 1\mu$m) one sees that $k \approx c\Delta P R_P$ where $c \approx 1.3$. Through changes in the suction pressure, the spring constant can range over 5 pN/nm – 0.05 pN/nm. Force sensitivity is limited by thermal excitations through

$$f_{min} \approx \sqrt{k_B T \cdot k} \tag{3.3}$$

At the softest spring constant, force measurement is limited to $\geq$ 0.4 pN by thermal fluctuations unless signal averaged in some way.

Figure 3.2 confirms that the probe/transducer assembly constitutes a one-dimensional harmonic oscillator for small deflections δ along the axis of symmetry. The mean square fluctuations of an one-dimensional harmonic oscillator of spring constant k must follow $< \delta^2 >= k_B T/k$. Figure 3.2 displays the mean square fluctuations of the probe versus the inverse stiffness of the transducer as given by equation 3.1. The line shown has a slope of $k_B T$, as required.

Precise translation of the transducer/probe assembly to/from a sample substrate is accomplished through a computer-controlled piezo actuator in both versions of the apparatus. Inherent hysteresis in the translation of the pipet is removed by prior calibration. The piezo has a repeatable hysteresis loop upon successive cycles of approach. As such, a nonlinear voltage ramp is applied to the piezo crystal to result in linear translation of

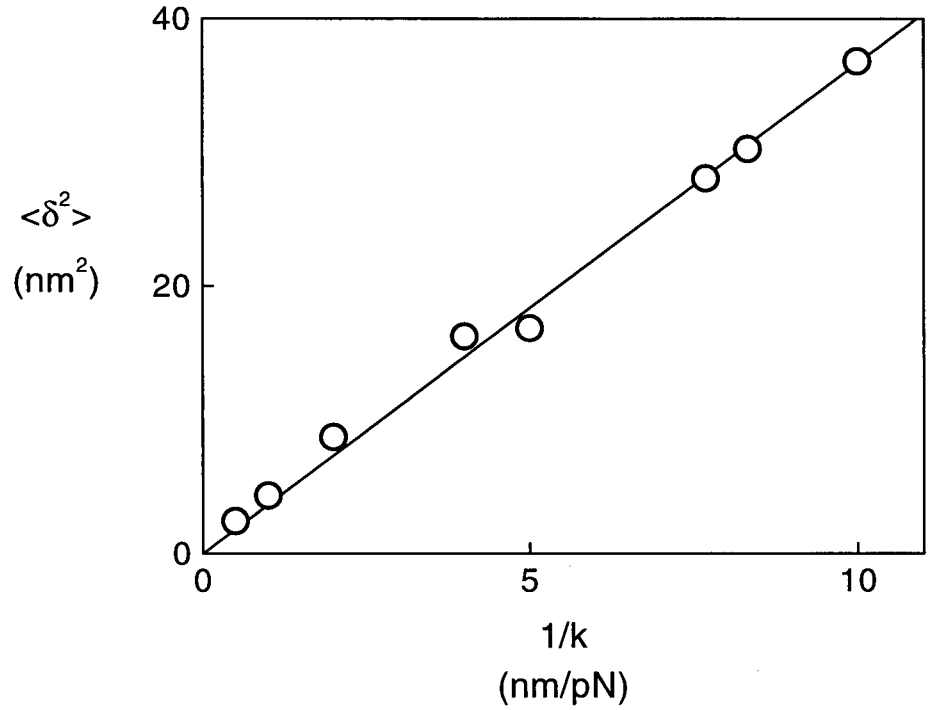

Figure 3.2: Mean Square Fluctuations of Probe.
Mean square fluctuation along the symmetry axis of the probe position δ as a function of the inverse spring constant k of the transducer. The linear relationship displays a slope of 3.7×10^{-21} J ($\sim k_B T$) confirming the force-transducer constitutes a one-dimensional harmonic oscillator.

the pipet. The non-linear ramp used is

$$V_i = V_{i-1} + \Delta V \frac{P_1}{P_1 + P_2 \exp\left((V_i - V_0)/P_3\right)} \tag{3.4}$$

where V_i is the voltage during the i^{th} step, ΔV sets the rate of translation and P_1, P_2 and P_3 are the calibrated parameters that correct the hysteresis.

Chapter 4

Vertical Instrument Design

4.1 Transducer Translation and Probe Position Sensor

Accurate positioning of the transducer holding pipet coupled to precise measurement of probe position is essential to determine transducer deflection and force. In this version of the apparatus, the transducer/probe assembly is oriented vertically above the sample. The sample is placed on the bottom of an aqueous buffer-filled container formed of cleaned cover glass. This chamber is mounted on the inverted microscope stage so the microscope objective looks through the sample. Coarse maneuvering of the transducer-holding pipet above the sample is accomplished by a mechanical 3-axis translator in series with the precise piezo actuator.

Precise force measurement requires the accurate recording of the probe position. Elevations of the probe above the glass base are found from reflection interference contrast (RIC) patterns imaged by the inverted microscope (Rädler and Sackmann, 1992; Rädler and Sackmann, 1993). The RIC image is created by epi-illuminating the probe through the objective. Reflection of the illumination beam from the top surface of the coverslip and from the bottom of the microsphere create the interference pattern, commonly known as Newton's rings, as shown in figure 4.3. The intensity variations $I(r, \theta : h)$ of the interference pattern produced by the probe follow

$$I(r, \theta : h) \sim \cos\left(\frac{4\pi n}{\lambda}(g(r) + h)\right) \tag{4.5}$$

for illumination wavelength λ through a buffer of refractive index n. The phase of the

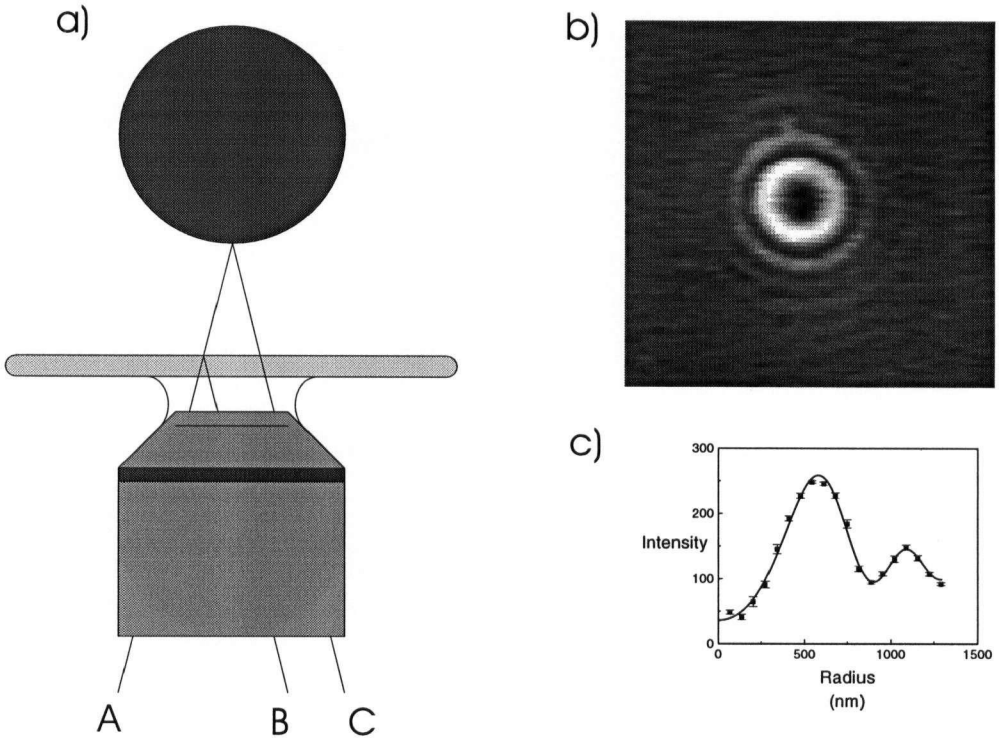

Figure 4.3: Pattern Generation in RICM.
a) Probe microsphere held above base coverglass (not to scale). Illumination beam A enters the oil immersion objective. Beams enter and emerge parallel to the optical axis. They are shown convergent for demonstration of the reflection only. The beam is reflected at the glass-buffer interface and at the buffer-probe surface. The two reflected beams B and C recombine to produce a Newton's ring pattern as in b). b) Image as digitized and analyzed in real video time (1/30 sec) by the dedicated computer. c) Fit to radial intensity profile of ring pattern in b).

ring pattern depends on the elevation of the probe above the glass base, h. The function $g(r)$ represents the geometrical height change of the spherical probe surface above the base at a radial distance of r from the center of the pattern. For a sphere of radius R

$$g(r) = R - \sqrt{R^2 - r^2} \tag{4.6}$$

Dedicated real-time video-image processing software was developed to control transducer position, determine the probe elevation and applied force in each video frame. During each frame, the fringe pattern is centered and circularly averaged to obtain the radial intensity profile of the probe. The circular averaging improves the signal to noise ratio. Fitting the theoretical profile of equation 4.5 to the radial profile yields the elevation of the probe above the base glass.

The change in distance between instantaneous probe position, z_b, and the piezo translation of the pipet, z_t, in the vertical direction specifies the applied force (*i. e.* $\delta = \Delta(z_t - z_b)$ and $f = k \cdot \delta$). By exploiting the spherical symmetry and fixed dimension of the probe, positions of the microsphere probe are determined to 1–5 nm accuracy at video framing speeds (30 Hz). At the lowest stiffness, this corresponds to a force resolution of $\sim$ 0.3 pN, comparable with the thermal resolution.

Real-time position and force information allows for decisions to be made during an experimental cycle. For instance, upon approach, the probe can be programmed to impinge the sample surface with a desired force. As such, a series of approach/retraction cycles can be made identical. Due to the high sensitivity in force measurement of the apparatus, the level of impingement can be set in the piconewton range. The extreme sensitivity to contact can allow the user to probe a soft surface with minimal disturbance to the surface.

4.2 The Complete Assembly

The complete vertical assembly is shown in figure 4.4. A Zeiss Axiovert 100 is fitted with a Antiflex Neofluar 63/1.25 oil immersion objective (Carl Zeiss, Oberkochen, Germany). Light from a 100W mercury arc lamp (Oriel, Stratford, CT, USA) is filtered to provide monochromatic light with a long coherence length of wavelength 546.1 ± 5 nm (Chroma, Battleboro, VT, USA).

Mounted on a gantry directly above the stage along the optical axis of the objective is the coarse 3-axis translator (Newport Corporation, Irvine, CA, USA) in series with the computer controlled piezo translator (Physik Instrumente, Waldbronn, Germany, 5 μm travel stacked piezo translator). Attached to the piezo translator is a chuck designed to hold the transducer micropipet connected by flexible water-filled tubing for accurate pressure control.

The micropipet aspiration technique used to hold the transducer cell is described in detail in (Waugh and Evans, 1979). In brief, borosilicate glass micropipets (Kimble, Vineland, NJ, USA, O.D. 0.7–1.0 mm, wall thickness 0.2 mm) are pulled and microforged to obtain a flat cylindrical opening with caliber of 2 μm. They are filled with buffer and attached to the chuck on the piezo actuator. When a transducer cell is aspirated into the open mouth, the suction pressure sets the tension in the transducer cell membrane as per equation 3.2 and hence the spring constant of the probe assembly.

The reflection interference image is collected through an existing camera port in the Axiovert 100 (100% of image intensity through port) by a Dage-MTI CCD72 (Dage-MTI, Michigan City, IN, USA) on manual gain and offset. The image is grabbed by an Intel based Pentium computer, 166 MHz, running Microsoft DOS 6.22 with an installed Matrox Meteor frame grabber board (Matrox, Dorval, Que, Canada). All software was

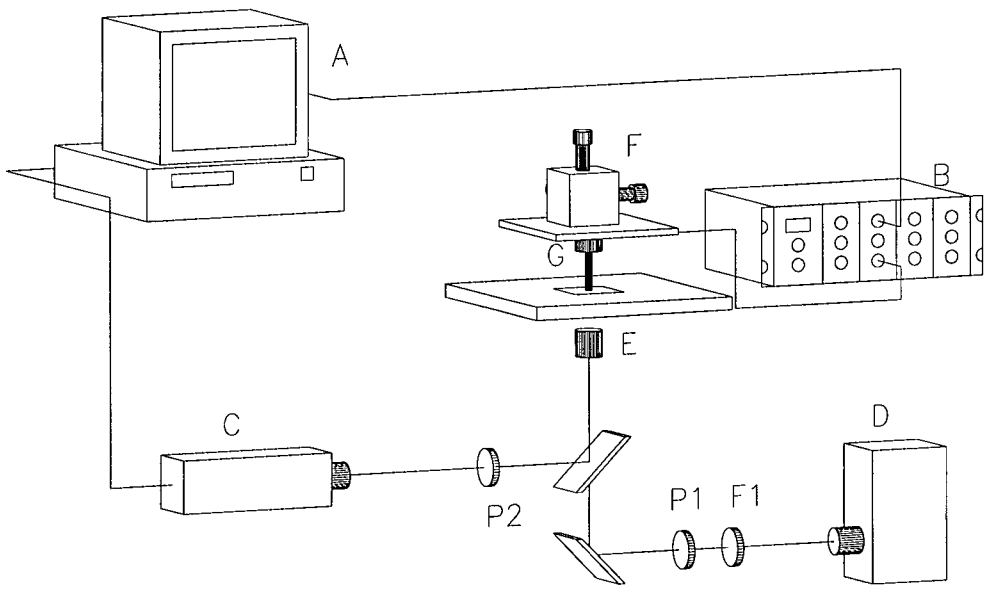

Figure 4.4: The Complete Vertical Assembly.
An epi-illuminated Antiflex microscope images the nanoscale positional changes of the probe microsphere. Light from arc lamp D is made monochromatic through filter F1 and linearly polarized through polarizer P1. The light travels through objective E to reflect from the sample container and probe microsphere and is recollected by the objective. An analyzer polarizer P2 enhances contrast before imaging by camera C and digitization and analysis by computer A. Simultaneously, computer A, using feedback from the analyzed image, controls the high voltage power supply B that drives piezo element G and hence controls the transducer probe assembly position above the sample.

personally designed incorporating routines supplied with the frame grabber board (Matrox MIL LITE 5.0, Matrox, Dorval, Que, Canada). Real time computer control of the piezo is performed through an Advantech PCL-818L Data Acquisition Card (American Advantech Corp., Sunnyvale, CA, USA) with steps in voltage applied every camera frame at 8 bit resolution.

A sample chamber is constructed for each experiment. Cleaned coverglass is glued with silicon grease (Dow-Corning, Midland, MI, USA) to an aluminum support to form an open topped container. The base coverglass may be chemically modified to present chemically or biologically interesting molecules to the probe, or be used as a platform to hold a sample. The sample chamber is filled with buffer (PBS, 0.15 M salts, 0.1% (w/v) BSA) which keeps the red cell transducer swollen to near spherical. Transducer cells and prepared probe microspheres are introduced to the chamber. Transducer/probe assemblies are then constructed just prior to tests performed.

Chapter 5

Horizontal Mode Instrumentation

Although the vertical setup has a high accuracy (1–5 nm) in measuring probe elevations due to the RICM interference technique employed, it is limited because the intervening test material must be thin and transparent. The vertical geometry is useful for examining molecules grafted onto the glass base or to thin, film-like samples (*i. e.* a thinly spread, activated platelet cell). The vertical geometry is difficult to use for tests of mechanical compliance in most living cells. A second apparatus has been developed and is in use to remedy this shortcoming. The capability of performing tests on thick structures allows the researcher to probe any cellular or synthetic material.

A schematic of the horizontal mode of the force-measuring apparatus is shown in figure 5.5. The BIP transducer/probe assembly of chapter 3 is again used as a force sensor. The probe holder pipet enters horizontally into a microchamber constructed of two parallel sections of cleaned coverglass separated by a support of $\sim$ 1.5 mm. The chamber contains buffer, transducer cells, probe microspheres and test substrates (side-by-side chambers on the same support can be used to separate test cells or to allow quick environmental change). A second pipet enters the opposing side of the chamber to hold a test substrate. The probe-to-sample separation distance is computer-controlled through piezo translation of the transducer or test surface holding pipet. With an accurate determination of the probe position (see next section) either the probe or the test surface is translated to make contact at a programmed force. Thus the general operation is similar to the operation of the vertical setup.

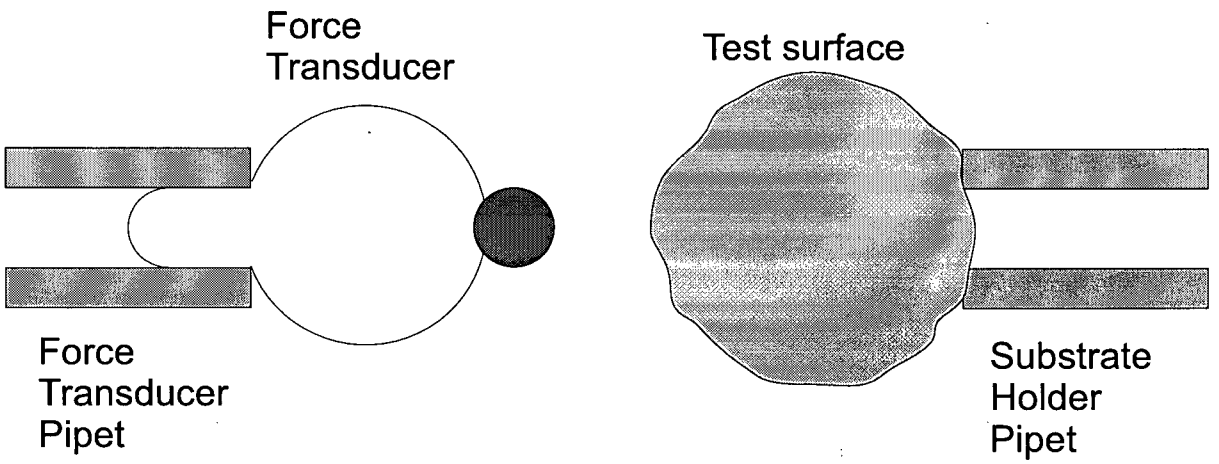

Figure 5.5: Schematic of Horizontal Apparatus.
In this design, the force transducer and substrate holder pipets enter horizontally, from opposing sides of the chamber, allowing thick, irregular test surfaces to be used.

5.1 Microsphere Probe Tracking

The horizontal geometry of this setup necessitates a new method for probe position determination. The image is collected as a bright-field image of the transducer/probe and test surface as shown in figure 5.6. The probe-microsphere, in bright-field microscopy, has a dark, thick diffraction limited edge with an approximately quadratic well in radial intensity. Exploiting the deep intensity well along the circumference of the probe, the probe is tracked by following the displacements of the minimum in intensity inside this dark ring. Four points are chosen to form a cursor in the shape of an x inside the dark ring of the probe. The fixed size of the probe allows the relative position of these four points to remain fixed. The fixed geometry minimizes effects of the sample surface while the probe and surface are in intimate contact. The accuracy to which the shifts in position of the probe can be detected is < 13 nm using the optics described in the following section. More accurate tracking is possible (8–10 nm). The position and resulting force are recorded by computer in real time. Decisions are made in real-time to terminate approach when a preprogrammed impingement force is reached.

5.2 The Complete Setup

The full horizontal assembly is shown in figure 5.7. A 3-axis translator (Newport Corporation, Irvine, CA, USA) is mounted on each side of the stage for coarse positioning of the two required pipets in the optical field of view. A Zeiss Aviovert 100 is fitted with a 40x 0.65 NA achrostigmat objective and 1.4 oil/ 0.9 air INA condenser (in air). Illumination is provided by a 200W mercury arc lamp (Oriel, Stratford, CT, USA) through a 546.1 ± 5 nm filter (Chroma, Battleboro, VT, USA) to provide the required transmission bright-field image. A piezo translator (Physik Instrumente, Waldbronn, Germany, 5 μm travel stacked piezo translator) is placed in series with one of the 3-axis translators. Both

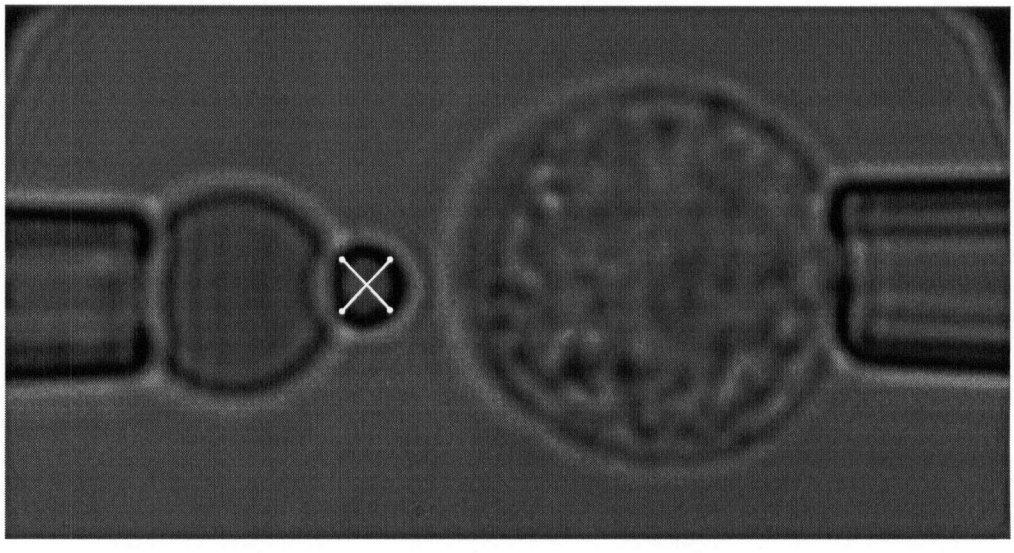

Figure 5.6: Image from Horizontal Apparatus.
Bright-field image as analyzed by a dedicated computer. A cursor (in white) is centered on the bead for every frame of video collected. Either the transducer (left) or sample (right) pipet is computer controlled via a piezo translator for precise approach and retraction.

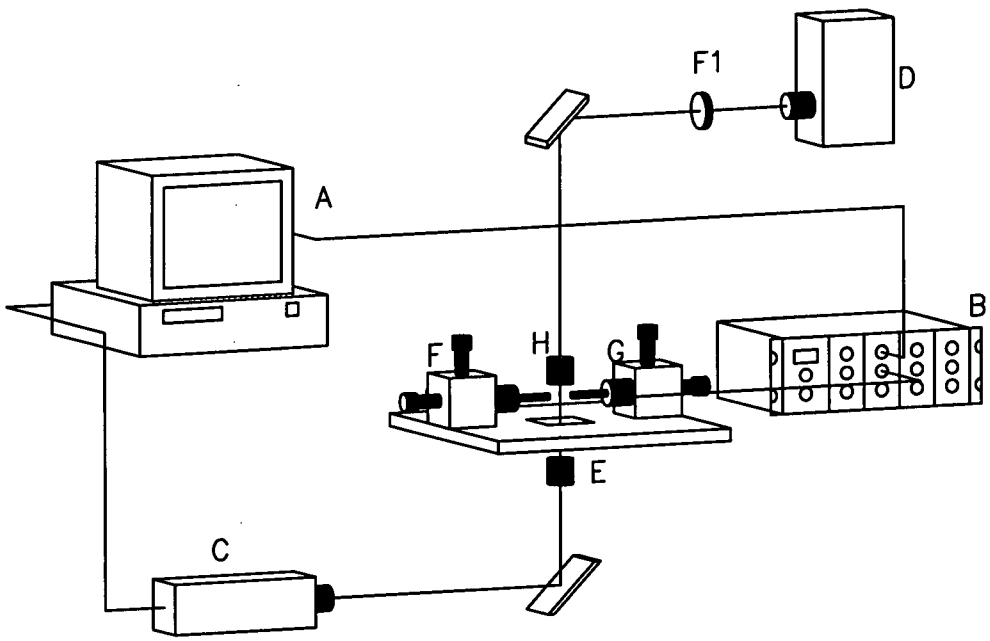

Figure 5.7: Complete Horizontal Apparatus.
The horizontal setup is imaged through a bright-field microscope. Light from arc lamp D, made monochromatic through filter F1, travels through condenser H and illuminates sample and probe. Objective E collects the image which is recorded by camera C and digitized and analyzed by computer A. Simultaneously, computer A using feedback from the analyzed image, controls the high voltage power supply B which drives piezo element G. Piezo element G sets the sample probe separation throughout an experiment.

translators have a chuck that in turn holds a micropipet connected by water-filled tubing to accurate pressure control. The micropipets used are identical to those of the vertical mode instrument.

The image is collected through an existing camera port by a Dage-MTI CCD72 camera (Dage-MTI, Michigan City, IN, USA) set on manual gain and offset. The camera is connected to an Intel based Pentium computer, 133 MHz, running Microsoft DOS 6.22 for image digitization through a Matrox Meteor frame grabber board (Matrox, Dorval, Que, Canada). Real-time computer-control of the piezo is performed through an Advantech PCL-818L Data Acquisition Card (American Advantech Corp., Sunnyvale, CA, USA) with steps in voltage applied every camera frame at 8 bit resolution.

5.3 Fast Frame Rate Version

A further limitation in both of the techniques described above is the 30 Hz frame rate of the standard video acquisition technology. The simplicity of the probe position algorithm used in the horizontal version allows for faster frame rates. The standard frame rate camera has been replaced by the Sensicam 360KL (PCO Computer Optics GmbH, Kelheim, Germany). The high speed camera has the ability to sustain frame rates upwards of 1000 frames per second for a reduced area of the CCD imaging array.

The control program has been upgraded to the Windows 95 operating system on a Pentium II, 300 MHz computer. Tracking of the probe now only involves following the shifts in the position of the intensity well at the pole opposite the the position where the test substrate makes contact. High speed movement of the piezo actuator is accomplished through a WSB-100 Waveform Synthesizer Board with the 12 bit analog-out module (Quatech, Inc., Akron, OH, USA). The waveform synthesizer board has the ability to output a series of voltages at rates up to 100 kHz, independent of the frame rate of the

attached camera.

The increased temporal sensitivity allows the horizontal version to attain loading rates up to 50,000 pN/s[1]. Loading rates as high as 50,000 pN/s match the slowest loading rates used in atomic force microscopy and thus allow direct comparison of results between the two distinct techniques. Direct comparison under similar loading rates are important in bond rupture tests as shown in Part III.

[1] At 10,000 pN/s and a frame rate of 1000 fps the sensitivity is still as low as 10 pN/frame.

Chapter 6

Summary

A highly soft and tunable biomembrane force transducer has been assembled into two related force probe instruments. The approaches compliment each other by allowing a wide range of accessible loading rates with a high force sensitivity at low rates with the vertical version and a high temporal resolution at high rates with the horizontal version.

The next section describes the application of the vertical version of the force measurement technique to measure mechanical compliance of a soft interface. Following the compliance test, experimental measurement of bond failure (by Pierre Nassoy and Andrew Leung (see Merkel *et al.*, 1998)) using both versions of the force probe technique is presented. Their bond failure tests were performed over an impressive 5 orders-of-magnitude range of loading rates spanning from the fastest loading rates that can be applied by optical tweezers to the loading rates attained by the atomic force microscope.

Part II

Nanoscale Compliance of Soft Interfaces

Chapter 7

Introduction

As a demonstration of the application of the force probe technique of Part I, the nano-mechanical compliance of the human red blood cell (erythrocyte) is tested. From a materials point of view, the human red blood cell is an amazing construction. The 8 μm diameter by 2 μm thick discocyte is simply a membrane encapsulated bag of liquid hemoglobin solution. Approximately 10^{13} cells travel through the circulation, squeezing through small capillaries for 120 days. As its primary function, it acts as a semi-permeable bag to transport oxygen from the lungs to the muscles and return carbon dioxide from the muscles to the lungs.

Much of the structure of the red cell membrane has been inferred from biochemical and pathological studies (see Mohandas and Evans, 1994, for an excellent overview). Emerging from these studies is a composite structure of the membrane. A simple cartoon of the membrane is shown in figure 7.8. The membrane consists of a thin liquid shell, the lipid bilayer, with a protein network pinned to its cytoplasmic (interior) side. The lipid bilayer shell is a two-dimensional liquid with embedded membrane bound proteins, some spanning the entire bilayer. Many of the bound proteins contain extracellular sialic acid groups forming a small *forest* of complex sugars that carry the blood group specificities.

The underlying network acts as a scaffolding. The network forms a triangular mesh-work, 70 nm on a side, of the highly flexible protein spectrin. Spectrin tetramers, 200 nm in length, are anchored to the liquid shell through the membrane bound proteins band 3 and glycophorin C and the cytoplasmic proteins band 4.1 and ankyrin (as well as possibly

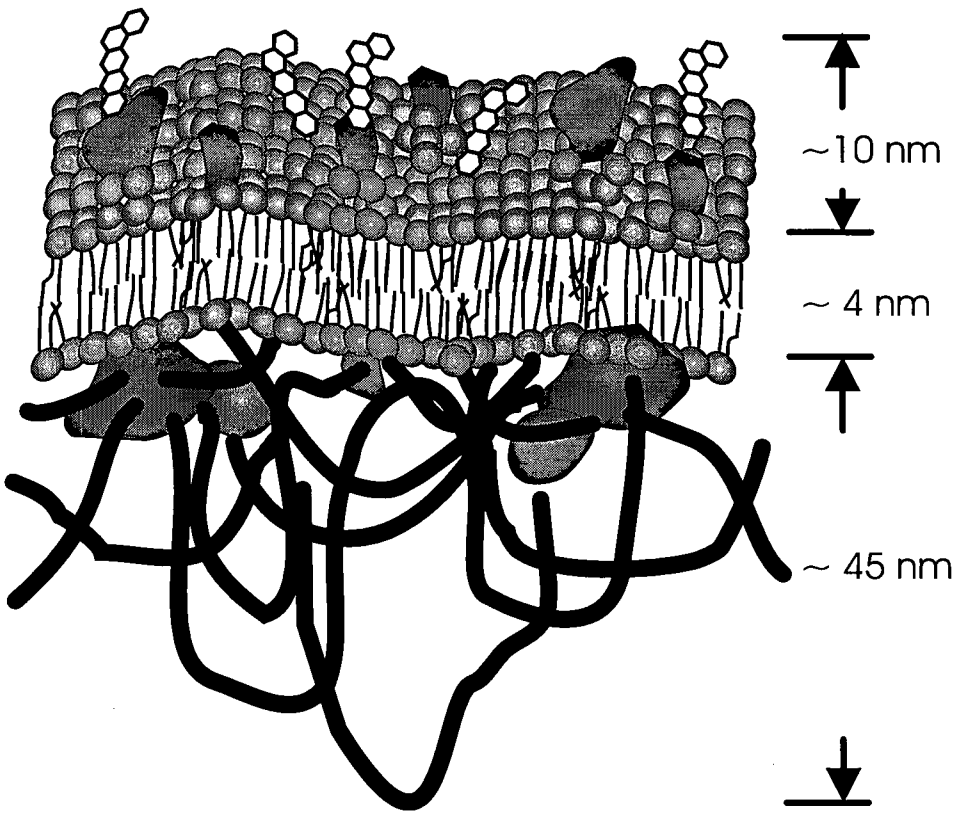

Figure 7.8: Cartoon of the Red Cell Membrane.
The red cell membrane interface consist of a composite of a liquid lipid bilayer with embedded protein and a hanging spectrin cytoskeletal network. The spectrin network forms a triangular scaffolding that gives the red cell interesting mechanical properties. The dimensions are values deduced from the measurements to be described in this section and other published data.

others).

The composite structure of the membrane gives the red cell interesting mechanical properties. The two-dimensional liquid shell of lipid surfactants has an essentially fixed total surface area (with area expansion modulus $\sim$ 500 dyn/cm (Evans, 1973a, 1973b)) and weakly resists interfacial bending (bending modulus, $k_c \sim 10^{-13} - 10^{-12}$ erg, (Evans, 1983)). The cytoskeletal scaffolding gives the interface its shear rigidity ($\mu \sim 10^{-2}$ dyn/cm, (Waugh and Evans, 1979)). This shear rigidity allows the red cell to return to its original shape after large extensional deformations.

Thickness compression measurements were performed with the vertical mode of the force probe technique of Part 1, as demonstrated in figure 7.9. The sample red blood cell was ghosted to remove the hemoglobin from its interior. Ghosting is a procedure in which the red cell membrane is lysed in order to release the contents of the red cell, which is mostly hemoglobin. After lysis, the membrane is resealed.[1] The ghost can be resealed with any solution in its interior. For these tests, a low ionic strength buffer was resealed inside the ghosts to osmotically flatten the sample cell at the ionic concentrations required by the force probe technique. The force was recorded as the probe approached the sample red cell ghost. After compression, the force continued to be recorded as the probe was retracted to complete a compression cycle.

[1]The lack of hemoglobin makes the cell difficult to see in bright-field microscopy since there is no index of refraction change except a weak change at the thin membrane of the cell. These hard to see cells are referred to as ghosts.

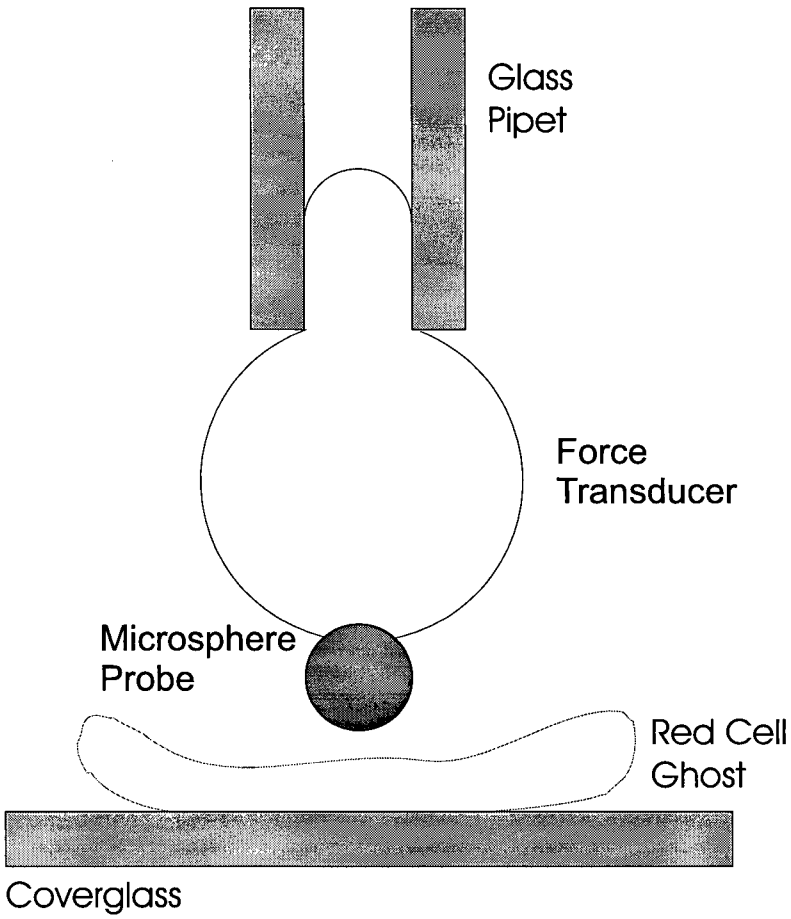

Figure 7.9: Schematic of the Compression Test.
The transducer/probe assembly approaches vertically from above a sample red cell ghost that sits freely on the base coverglass. The transducer was driven vertically through a computer-controlled piezo actuator to and from the sample ghost. Probe elevation and the applied force were measured as a function time.

Chapter 8

Methods

8.1 Probe Preparation

For all compression experiments, the probe was a $2.5 \pm 0.5\mu$m diameter borosilicate microsphere (Duke Scientific, Palo Alto, CA, USA) cleaned, silanized and functionalized with a polymer bound biotin. After covalent linkage to polymer-biotin, the beads are incubated with the protein avidin which has four binding pockets for biotin (Molecular Probes, Eugene, OR, USA). These microspheres were then attached to a biotinylated red cell for use as a transducer as described in section 8.2. Specifics are given below.

8.1.1 Cleaning of Microspheres

The cleaning method follows procedure G-1A of (Rosebury, 1965). Microspheres (30 mg) were boiled in a 5 % hydrogen peroxide (H_2O_2) solution at pH. 11.0 (adjusted with ammonium hydroxide, NH_4OH). Microspheres were next washed with 10 ml of distilled water (d-H_2O) thrice and resuspend to 10 % (w/v) solids in d-H_2O.

8.1.2 Silanization

Clean microspheres were washed in methanol to remove water. The microspheres were incubated with N-2-aminoethyl-3-aminopropyl-trimethoxy-silane (AEAPTMS) (United Chemicals Technologies, Inc., Bristol, PA, USA) under acidic conditions in methanol for 5 minutes. The microspheres were then washed in methanol, dried and heated for 5

minutes at 120 °C to enhance covalent bonding of the silane to the glass. In advance of the experiments, Microspheres were resuspended in aqueous buffer.

8.1.3 Attachment of Biotin

Silanized microspheres ($\sim$ 1 mg/ml) were incubated with NHS-PEG-biotin (a 3400 molecular weight polyethylene glycol polymer with a NHS reactive group (n-hydroxy-succinimide ester) terminating one end which binds to preferentially to primary amine groups, and a biotin terminating the other, Shearwater Polymers, Inc., Huntsville, AL, USA) at 4 mg/ml in 0.1 M carbonate-bicarbonate buffer[1] (pH 8.5). The microsphere-NHS-PEG-biotin conjugates were incubated 1 hour at room temperature. The suspension was then washed in Tris buffered saline (TBS, 25 mM Tris, 150 mM NaCl, pH 7.5), thrice, to terminate the binding reaction. The microspheres were washed in d-H_2O with 0.1 % (w/v) NaAz, thrice, to remove any excess NHS-PEG-biotin. The microspheres were preserved at this stage until use.

8.1.4 Avidin Conjugation

Prior to use, the microspheres were bound with the tetra-valent protein avidin by mixing 1.25 mg of the biotin conjugated microspheres with 4 μg of avidin in 750ml of phosphate buffered saline (PBS, 4.8 mM KH_2PO_4, 26 mM Na_2HPO_4, 120 mM NaCl, pH 7.4) for 30 minutes. The microspheres were washed thrice in 500 μ of PBS (150 mM salts) to remove excess avidin. This completed the preparation the probes.

[1]Make a 0.1 M sodium bicarbonate solution and titrate 0.1 M sodium carbonate to get pH 8.5.

8.2 Preparation of Transducer

Human red blood cell (RBC) to be used for transducer capsules were globally bound with a polymer terminating in a biotin moiety. Red cells were obtained from whole blood drawn by finger prick (6–7 μL) and washed once in PBS (150 mM salts). The cell pellet was then washed thrice in 0.1 M carbonate-bicarbonate (pH 8.5). A volume of 3 μL of packed RBC were mixed in 900 μL of 0.45 mM NHS-PEG-biotin (a 3400 molecular weight polyethylene glycol polymer with a NHS group terminating one end and a biotin terminating the other, Shearwater Polymers, Inc., Huntsville, AL, USA) and incubated 30 minutes at room temperature. After incubation, the cells were washed thrice in TBS (pH 7.5) and once in PBS (150 mM salts). The PEG-biotin decorated cells were stored in PBS (150 mM salts) with 0.5 % (w/v) bovine serum albumin (BSA, Sigma Chemical Co., St. Louis, MO, USA) until used. This completed the transducer preparation. As such, a probe microsphere prepared in the preceding section could be glued to the transducer cell by thousands of biotin-avidin bonds on contact.

8.3 Sample Preparation — Ghosting

The test sample used in the compression tests was a ghosted human red blood cell (ghost). Ghosts were produced by lysing the blood cell allowing the internal hemoglobin to escape. The *pinkness* of the ghost is reflected by the amount of hemoglobin remaining after resealing. The ghosting procedure followed the method of Dr. Ted Steck (University of Chicago, personal communication). Fresh whole blood was obtained by finger prick (50 μL). All washes in the following procedure were carried out for 2 minutes at 4500 g. Cells were washed in 5 ml of TS-PBS (5 mM phosphate buffer, pH 8.0, 150 mM NaCl) thrice. The cell pellet was then incubated at less then 4°C in cold lysis buffer (5 mM phosphate buffer, pH 8.0) for 5 minutes then spun down. This is labeled as *single* washed

ghosts. The pellet could then be resuspended and incubated in new, cold lysis buffer for 5 minutes 1 or 2 more times to make *double* and *triple* washed ghosts, respectively. After the final spin, the cell pellet was resuspended in resealing buffer (5mM phosphate buffer, pH 8.0, 15 mM NaCl) and incubated at 37°C for 10 minutes. Finally, the ghosts were washed thrice in TS-PBS and once in PBS (75 mM salts) with 0.5% (w/v) BSA before use.

8.4 Compression Measurement Protocol

Chambers to perform the compression were constructed upon to an aluminum support. Cleaned coverglass (dipped in pH $\sim$ 10 NaOH and washed extensively) were sealed to the support with silicon vacuum grease (Dow Corning Corp., Midland, MI, USA) to form an open top box. The base of the chamber was held in place with a *touch* of nail polish outside the grease barrier (to secure the base against creep). The ghosts, transducer cells and prepared microspheres were introduced to the chamber in PBS (0.075 mM salts) + 0.1% (w/v) BSA. A baffle separated the chamber into two sections such that the transducer cells and ghosts were kept separate. A pipet of approximately 1μm radius was set to zero pressure prior to aspirating a transducer cell. The transducer cell was then pushed onto the top of a probe microsphere to form adhesive contact. The probe-transducer assembly was then moved to the other section of the chamber where tests were performed on ghosts. First, the probe was pushed against the coverglass base (*i. e.* with no ghost) as a control then a ghost was compressed as shown in figure 9.10. Comparison of the bare surface compression to the ghost compression was used to determine the thickness compliance of the top and bottom ghost membranes.

Chapter 9

Results and Discussion

The red cell membrane is a complex structure that, on the scale of the area probed in these tests was neither a continuum nor isotropic. As such, results of the compression analysis of the human red blood cell have to be analyzed carefully and because of biological variability the results differ considerably from cell to cell. Still some general aspects can be gleaned from thickness compliance measurements. Figures 9.10 and 9.11 show examples of an approach/retraction cycle obtained in tests of 2 different single and triple washed cells. Shown along with the ghost compression curves is compression of the probe directly against the base coverglass, which exposed a small compliance of the molecular glue bound to the probe plus a coating of serum albumin used to inhibit adhesion to the clean coverglass base and transducer pipet. Both the single and triple washed ghosts exhibit an elastic response to compression with no obvious hysteresis in the force curve upon retraction at a velocity of 30 nm/s. The approach and retraction curves for the compression of the red cell membrane display many *bumps* along them. These *bumps* most probably reflect the coarseness of interfacial structures, perhaps arising from large molecules or molecular aggregates associated with the membrane cytoskeleton. The inconsistent appearance of the *bumps* implies that these structures are sparsely distributed in the membrane.

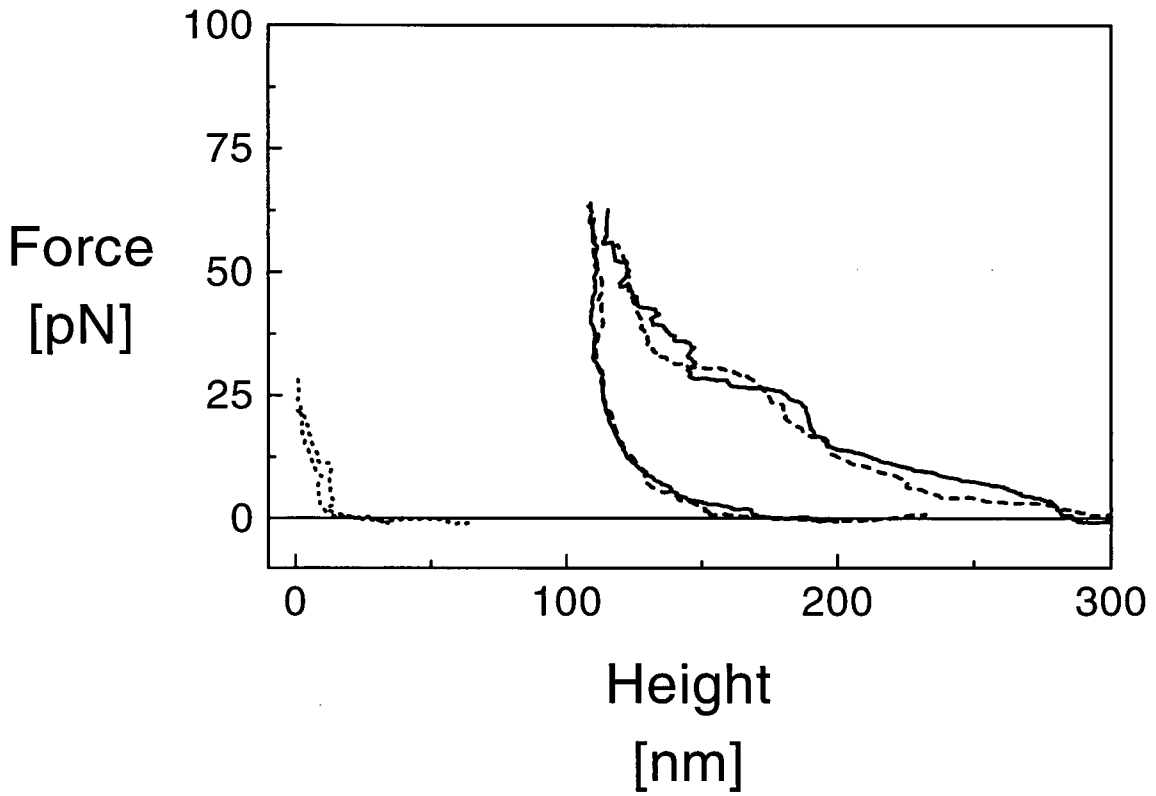

Figure 9.10: Compression Cycle for Two Single Washed Ghosts.
Approach (solid) and retraction (dashed) curves for compression of the single washed ghosts. The variability in the compression curves between samples is demonstrated. The dotted lines show the probe against the coverglass, which exposed the small compliance of molecular coatings on the probe and coverglass.

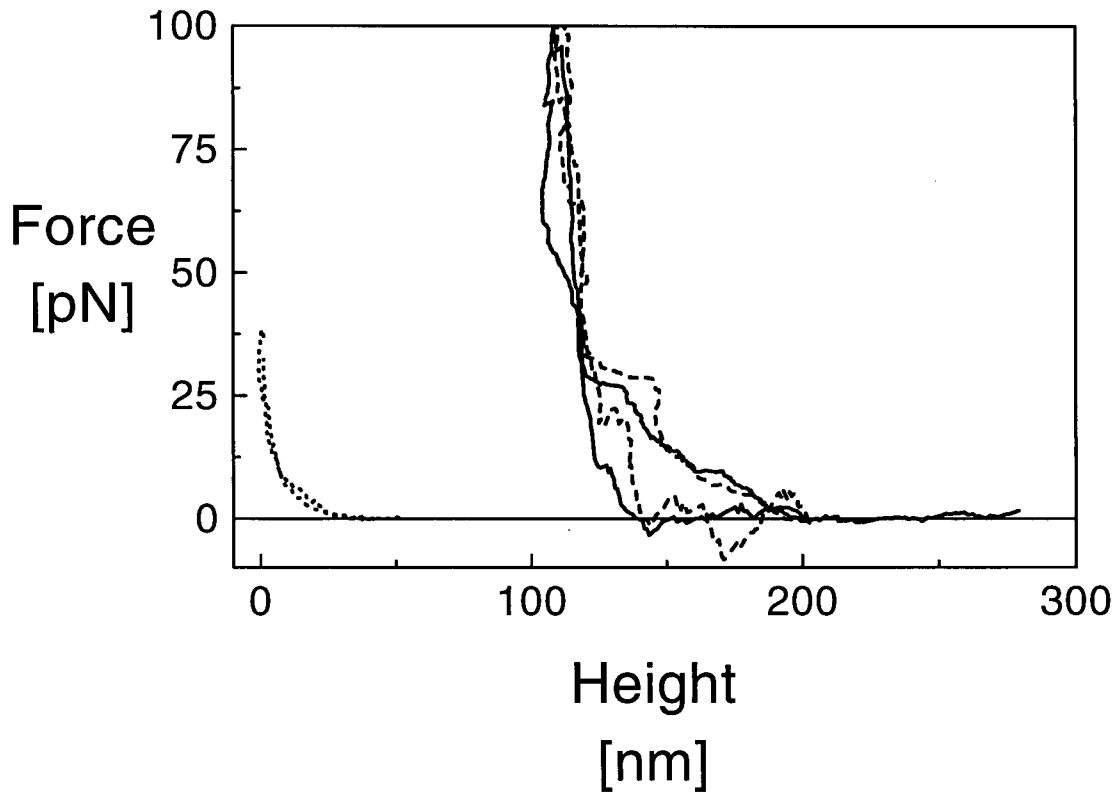

Figure 9.11: Compression Cycle for Two Triple Washed Ghosts.
Approach (solid) and retraction (dashed) curves for compression of the triple washed ghosts. The variability in the compression curves between samples is demonstrated. The dotted lines show the probe against the coverglass, which exposed the small compliance of molecular coatings on the probe and coverglass.

9.1 Membrane Thickness

The onset of force, corresponding to the initial thickness of the top and bottom ghost membranes, occurs at a thickness of 208 ± 14 nm for triple washed ghosts and at 211 ± 11 nm for single washed cells where all errors are given as the standard error (S. E.) of the mean. Thus there appeared to be no change in the initial thickness of the ghost membrane after repeated dilution of the ghost interior which was clearly apparent as a reduction in *pink* color. Thus the rest thickness of a single red cell membrane is $\sim$ 105 nm.

Under a compression of greater than 50 pN, the thickness of the red cell ghost appeared to resist appreciable change. The minimum thickness under compression for the triple washed ghosts is found to be 116 ± 8 nm (S. E.) and for single washed ghosts is 136 ± 8 nm (S. E.). The minimum membrane thickness for a single interface is thus found as $\sim$ 58 nm and $\sim$ 68 nm for the triple and single washed membrane, respectively. By comparison, Bull *et al.* (1986) estimated membrane thickness to be 57 ± 4 nm (S. E.) by examining electron micrographs of intact red blood cells strapped like *saddle bags* over spider web strands in a flow field. Chemically fixed to hold its shape after removal of the flow field, Bull *et al.* found that under high stress, the total red cell thickness reaches a minimum of 114 ± 8 nm but that under relaxed conditions the two membranes were much thicker at $\sim$ 213 nm. In other work, Fischer (1988) estimated the thickness by examining electron micrographs of osmotically thinned red cells which were cross bonded by heat and chemical treatment. Fischer found a range of single membrane thicknesses of 40–120 nm.

The bilayer and external glycocalyx is thought to be about 14 nm in thickness. Thus the cytoskeleton and membrane-associated proteins appear to be $\sim$ 44 nm in thickness under compression for triple washed ghosts and about $\sim$ 91 nm when unstressed. In computer simulations of a model network for the spectrin cytoskeleton, Boal (1994)

predicted that the rest thickness of the spectrin network was 30 nm (with an average thickness of about 15 nm). Thus, the membrane is much thicker than expected from the size and geometry of the spectrin network. This indicates the large proteins in the network may act to expand the interface or to separate the network from the lipid bilayer. Some of the thickening is probably due to bound hemoglobin (Shaklai *et al.*, 1977) which can be removed by persistent washing, as seen in the thinning the membrane of triple washed ghosts. Also, the cytoplasmic (internal) domain of the membrane protein Band 3, an anion transporter implicated in anchoring the spectrin network, could project as much as 60 nm into the interior of the red cell if in a fully extended configuration (Bull *et al.*, 1986), which could also contribute significantly to the thickness.

9.2 Membrane Compressibility

To determine a compression modulus for the red cell interface, a model for the interface must be chosen. As a simplest approximation, consider the interface a semi-infinite half-space with isotropic elastic properties being impinged by a hard sphere as in figure 9.12. The force required to indent a distance δ into a semi-infinite half-space by a sphere of radius, R, was first solved by Hertz in 1882 (see Landau and Lifshitz (1986) chapter 9 for the more general solution). The result is

$$F = \frac{4}{3}\sqrt{R}\tilde{E}\delta^{3/2} \tag{9.7}$$

where the elastic coefficient $\tilde{E}$ is given by

$$\begin{aligned} \tilde{E} &= \frac{E}{1-\sigma^2} \\ &= \frac{4\mu(3K+\mu)}{(3K+4\mu)} \end{aligned} \tag{9.8}$$

where E is the Young's modulus, σ is the Poisson's ratio, K is the compression modulus and μ is the shear modulus. For an incompressible material ($K \gg \mu$), $\tilde{E}$ goes to 4μ. For

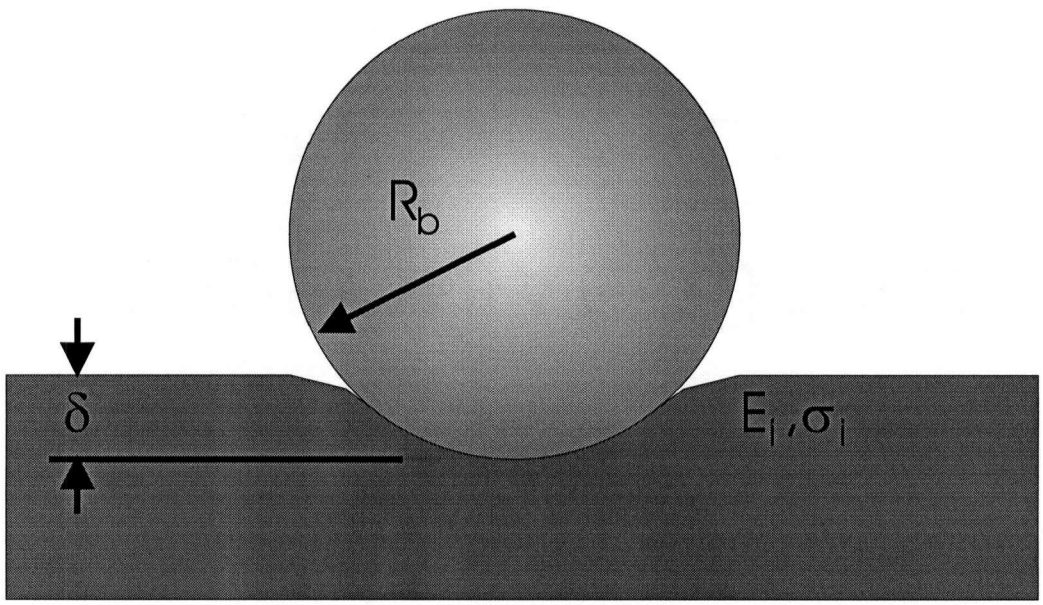

Figure 9.12: The Hertz Model.
A hard probe of radius R_b is compressed a distance δ into a semi-infinite isotropic half-space characterized by a Young's modulus, E_i and Poisson ratio σ_i.

a small compression modulus, $\tilde{E}$ goes to μ. Thus $\tilde{E}$ approximately measures the shear modulus of the semi-infinite half-space.

The use of the Hertz model requires careful examination. The Hertz model represents the response to compression of an isotropic, semi-infinite half-space. The red cell membrane is not infinitely thick nor isotropic as demonstrated by the asymptotic rise in stiffness in the compression curves of figures 9.10 and 9.11. In the Hertz theory, the displacement field drops off as the inverse of the distance from the interface with a characteristic decay length of $\sqrt{f/\tilde{E}}$ under a compression force, f, applied to a medium of compression modulus $\tilde{E}$. Hence for a 20 pN compression into a medium of $\tilde{E} = 2 \times 10^{-3}$ pN/nm^2 yields a decay length of about 100 nm. This decay length is comparable to the thickness of the compressed red cell. Thus only an initial small compression at the start of an approach cycle will be considered and the results are taken to be marginal at best.

The result of fitting the Hertz model to the small compression phase of single washed ghosts yielded a value[1] for $\tilde{E}$ of $(2.3 \pm 0.5) \times 10^4$ dyn/cm^2 (2.3 ± 0.5 kPa), while triple washed ghosts yielded a value for $\tilde{E}$ of $(3.2 \pm 1.7) \times 10^4$ dyn/cm^2 (3.2 ± 1.7 kPa). Comparing this to the compression modulus for an ideal rubber of about 10^6 dyn/cm^2 (100 kPa), the extreme softness of the red cell membrane is exposed. In the computer simulations of a model network for the spectrin cytoskeleton of Boal (1994), a compression modulus of $(2.0 \pm 0.1) \times 10^4$ dyn/cm^2 (2.0 ± 0.1 kPa) was found. This modulus shows close correspondence to the value measured here by direct red cell compression. Thus, although the spectrin network is further from the membrane than expected, due to embedded protein, the elastic response of the membrane is due to the spectrin network alone. The embedded protein, under low compression, does not effect the elastic response of the network.

A second, discrete model for the response of the red cell membrane to compression is

[1] All errors are quoted as the standard error of the mean in this section.

to consider the cytoskeleton as a uniform, two-dimensional array of independent polymer springs as shown in figure 9.13. As the probe impinges the surface, the individual springs are compressed along the contour of the probe. The total reaction force is the sum of the individual spring responses. A probe of spherical geometry has a radial profile of

$$\delta(r) = R - \sqrt{R^2 - r^2} \tag{9.9}$$

where R is the radius of the probe. If the probe indents the soft interface by δ_m, then the radius of contact, r_{δ_m}, is

$$r_{\delta_m} = \sqrt{R^2 - (R - \delta_m)^2} \tag{9.10}$$

The reaction force from the springs at a constant number density per area of ρ inside the contact is

$$F = 2\pi\rho \int_0^{r_{\delta m}} f_s(\delta(r)) r dr \tag{9.11}$$

where $f_s(\delta(r))$ is the spring restoring force for a top and bottom spring in series. A spring restoring force of an ideal polymer under compression is chosen. For two identical springs in series, the total restoring force is

$$f_s(\delta(r)) = \frac{4k_BT}{b} \frac{R_{ee}^2}{(2R_{ee} - \delta)^2} \tag{9.12}$$

where R_{ee} represents the size of a single polymer spring and b is the monomer size or correlation length of the polymer. From equations 9.10–9.12, the total reaction force to the bead impingement is thus

$$F = 8\pi R_{ee}^2 \rho \frac{k_BT}{b} \left[\ln\left(\frac{2R_{ee}}{2R_{ee} - \delta_m}\right) + \frac{2R_{ee} - R}{2R_{ee}} - \frac{2R_{ee} - R}{2R_{ee} - \delta_m} \right] \tag{9.13}$$

Results from fitting equation 9.13 to the red cell ghost compression data yielded values of $\rho(k_BT/b)$ of 80 ± 40 dyn/cm^2 for triple washed ghosts and 56 ± 24 dyn/cm^2 for single washed ghosts. An equivalent Young's modulus, E, can be found through

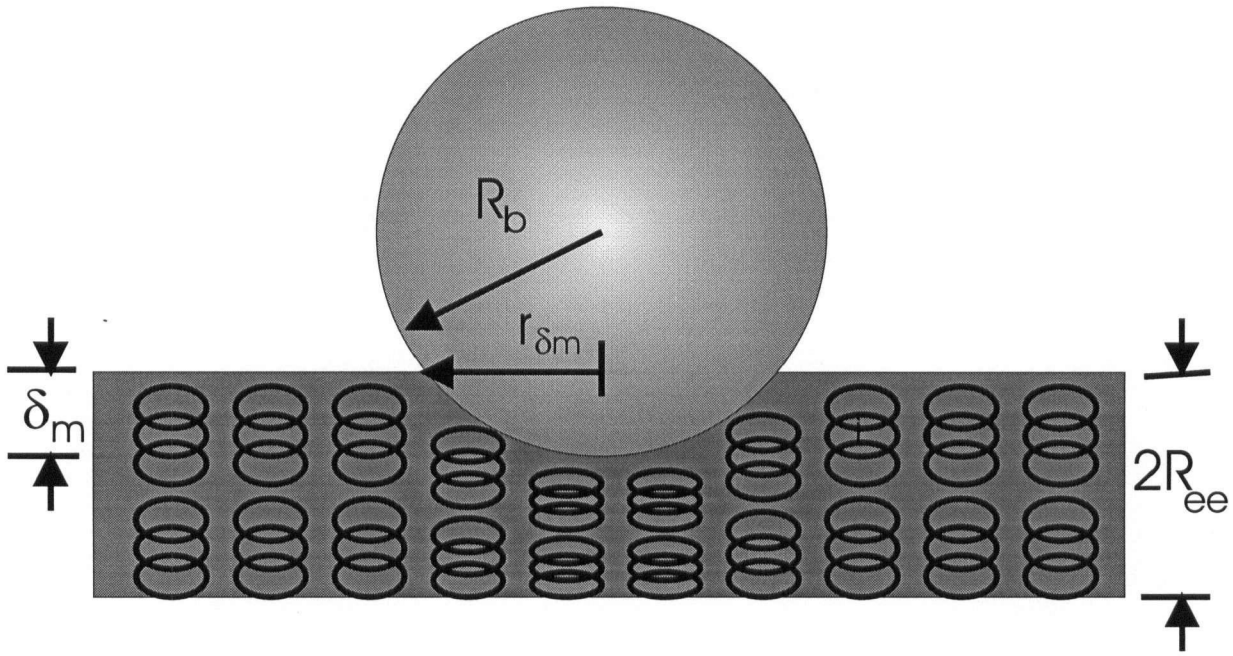

Figure 9.13: The Network of Springs Model.
A probe of radius R_b indents the $2R_{ee}$ thick sample a distance δ_m, making contact over a radius of r_{δ_m}. Each independent spring has a response to compression of $f = (k_B T/b)R_{ee}^2/(2R_{ee} - \delta_m)^2$. The springs in the model are equally spaced over the sample.

$E \sim -\rho[\frac{\partial f_s}{\partial \delta_m}]_{\delta_m=0} 2R_{ee}$ which gives a value for the modulus of $E \sim 2\rho(k_B T/b)$. Hence the Young's modulus derived for the membrane compression from this model was $\sim$ 160 dyn/cm^2 ($\sim$ 0.16 kPa) for triple washed ghosts and $\sim$ 110 dyn/cm^2 ($\sim$ 0.11 kPa) for single washed ghosts.

The polymer size, R_{ee}, was left as a fitting parameter in equation 9.13. The value of the polymer size yields a measure of the thickness of the region under compression (*i. e.* hard elements such as the lipid bilayer are not included in the initial spring length). The thickness by this measure of the region under compression for triple washed ghosts is 75 ± 11 nm and for single washed ghosts is 95 ± 10 which is much greater than the 30 nm size predicted from the computer simulations of Boal (1994). This, again, points to the existence of large assemblies acting to expand the membrane's spectrin cytoskeleton.

Part III

Strength of Molecular Surface Bonds

Chapter 10

Experimental Bond Strength Measurement

The advent of highly sensitive force measurement techniques (such as the surface forces apparatus in 1978 (Israelachvili and Adams, 1978) and the atomic force microscope in 1986 (Binnig *et al.*, 1986)) have allowed experimental measurement of the force required to separate weak biochemical linkages. Techniques such as the atomic force microscope (AFM) (Hoh *et al.*, 1992; Radmacher *et al.*, 1992; Lee *et al.*, 1994; Florin *et al.*, 1994; Moy *et al.*, 1994; Williams *et. al.* , 1996), optical tweezers (OT) (Ashkin *et al.*, 1990; Kuo and Sheetz, 1993; Finer *et al.*, 1994) and our own probe technique of Part I (Evans *et al.*, 1994; Evans *et. al.* , 1995; Merkel *et al.*, 1998) have the ability to measure forces in the range expected for weak bonds (*i. e.* 1–1000 pN) in biology.

Much of the key initial experimental work has been done on the avidin-biotin complex. Avidin, and its closely related cousin streptavidin, is a protein with four high affinity binding sites for the vitamin biotin (see (Savage *et al.*, 1992) for a thorough review of avidin-biotin technology). With a reported $35k_BT$ binding energy, the system is expected to be strongly adherent and having been modeled in atomic detail by molecular dynamics (Grubmüller *et al.*, 1996; Izrailev *et al.*, 1997) presents a useful test system.

Early reports of breakage of the streptavidin-biotin complex give a single force as the strength at which the bond dissociates (257 pN for Moy *et al.*, 1994, 340 pN for Lee *et al.*, 1994). No mention of the rate at which the bond was loaded was given. Experiments performed with the AFM attain loading rates upward of 50000 pN/s. Recognizing that bond failure is a kinetic process and that the mean lifetime of the bond will depend on

the rate of force-loading, the effect of the loading rate on the measured strength is likely to be very important (as will be shown by the following experimental data and analysis).

Application of the force probe instrument of Part I to bond strength measurement has been performed by Pierre Nassoy and Andrew Leung in our lab (see Merkel *et al.*, 1998). Their results are presented here to demonstrate experimental data for bond breakage and to set the stage for the theoretical analysis of the next section.

Bond breakage measurements were performed on the biotin-avidin system.[1] The test and probe surface were both glass microspheres covalently linked with a biotin terminating polymer. Avidin was bound to the probe microsphere as the *glue* for attachment to the transducer (a biotin conjugated human red blood cell) and as the receptor for attachment to a biotinylated test microsphere to form the linkage to be tested.

To obtain the strength of a bond, repeated approach/retraction cycles are performed between the probe and test substrate. Since both the probe and test microspheres are saturated with avidin, a biotin-avidin linkage forms infrequently as a result of a few free exposed biotins on either surface. The sparse amount of available biotins on the probe ensures that less than 10% of all cycles performed actually form a bond. The placement of receptors and ligands are random on their respective surfaces. For controlled contacts with infrequent attachments, the probability of a match of receptor and ligand between the surfaces should be governed statistically by a Poisson probability distribution. Thus, if 10% of all attempts actually form bonds, then 95% of those bonds are a single bond.[2] The instrument of Part I ensures that each cycle is an equivalent attempt through controlling the impingement force and the rate of retraction.

Two examples of approach/retraction cycles are shown in figure 10.14. The figure

[1]The biotin-streptavidin system was also probed in (Merkel *et al.*, 1998), but those results are not discussed here.

[2]If the frequency of attachment increases to 50% then one expects 69.4% of these are single bonds, 24% are double bonds and 6.6% are triple or greater.

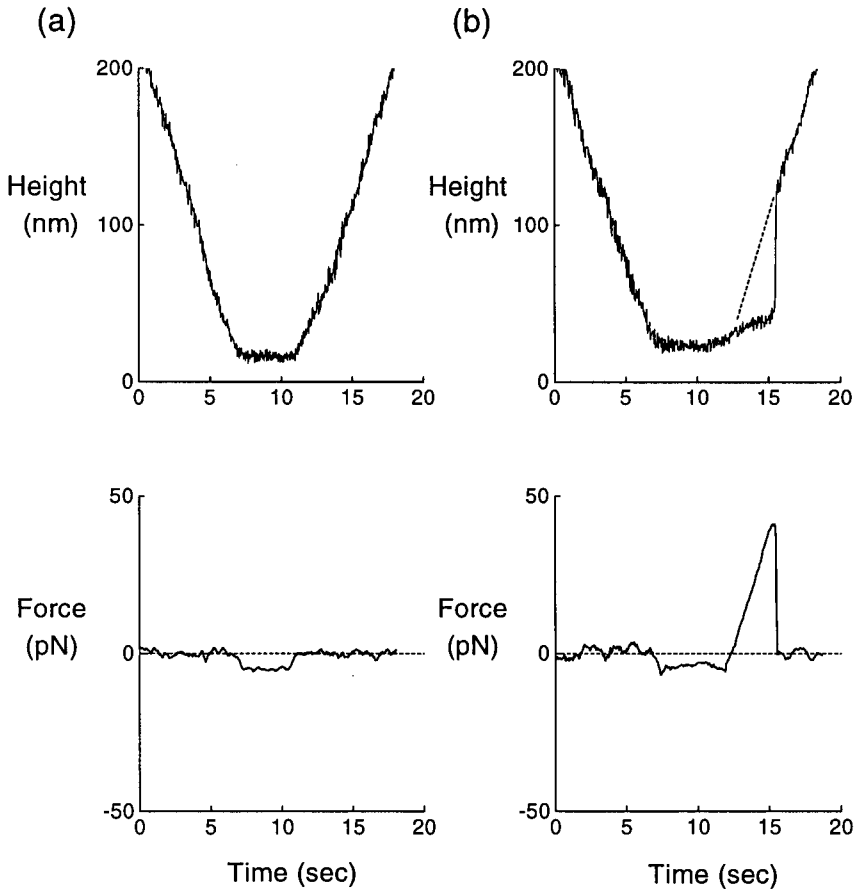

Figure 10.14: Experimental Approach and Retraction Trajectories in Tests of Bond Strength.

Probe tip position and force versus time in the vertical mode for approach – pause – retraction a) without bond formation and b) with bond formation. Bond failure is signaled by rapid recoil of the probe. Rupture strength, from the maximum transducer extension, is 57 pN in this case. Both cycles were performed at a loading rate of 18 pN/s in this example. The experiment was performed by Pierre Nassoy.

displays the probe position as a function of time through each cycle. One cycle shows contact without bond formation and the other shows contact followed by attachment then bond rupture. The maximum force reached prior to the precipitous failure of the bond defines the breakage force of the attachment. After repeated cycles, a histogram of the breakage forces is obtained for bond failure at a particular force loading rate. Figure 10.15 shows a typical bond strength histogram performed at a loading rate of 1000 pN/s. A total of 713 cycles were performed with 54 randomly interspersed bonding events. The rest of the cycles showed no bond formation or attachment force as in figure 10.14a. Note the peak in the distribution is used to define the most frequent strength of the bond at the set loading rate. Force histograms were collected at varying loading rates (over 5 orders-of-magnitude) for the biotin-avidin system to yield a plot of most frequent strength *vs.* logarithm of the loading rate $\dot{f}$ as shown in figure 10.16. The striking features of figure 10.16 are the distinct linear regimes of strength dependence on the logarithm of the force loading rate.

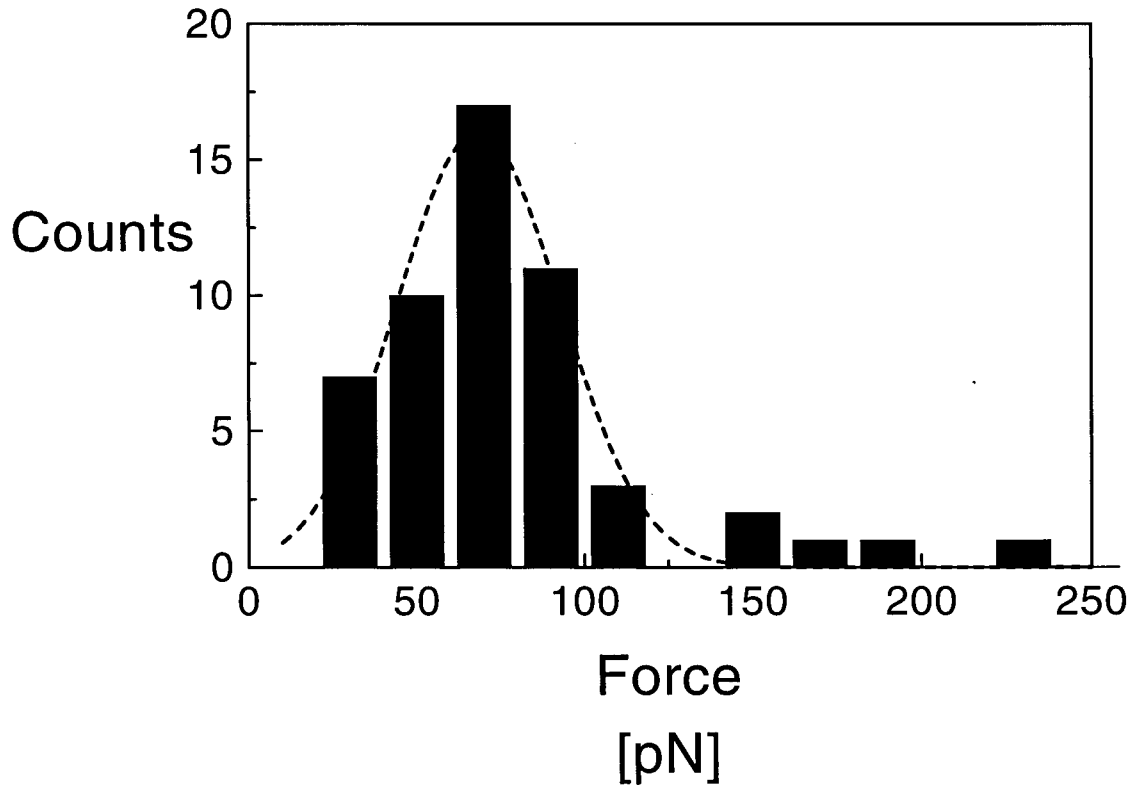

Figure 10.15: Experimental Bond Strength Histogram.
Bond strength histogram for the breakage of the biotin-avidin linkage at a loading rate of 1000 pN/s. A Gaussian curve (dashed) is fit to aid in viewing the peak and width. The frequency of bonding was 0.08 (54 bonding events out of 713 events).

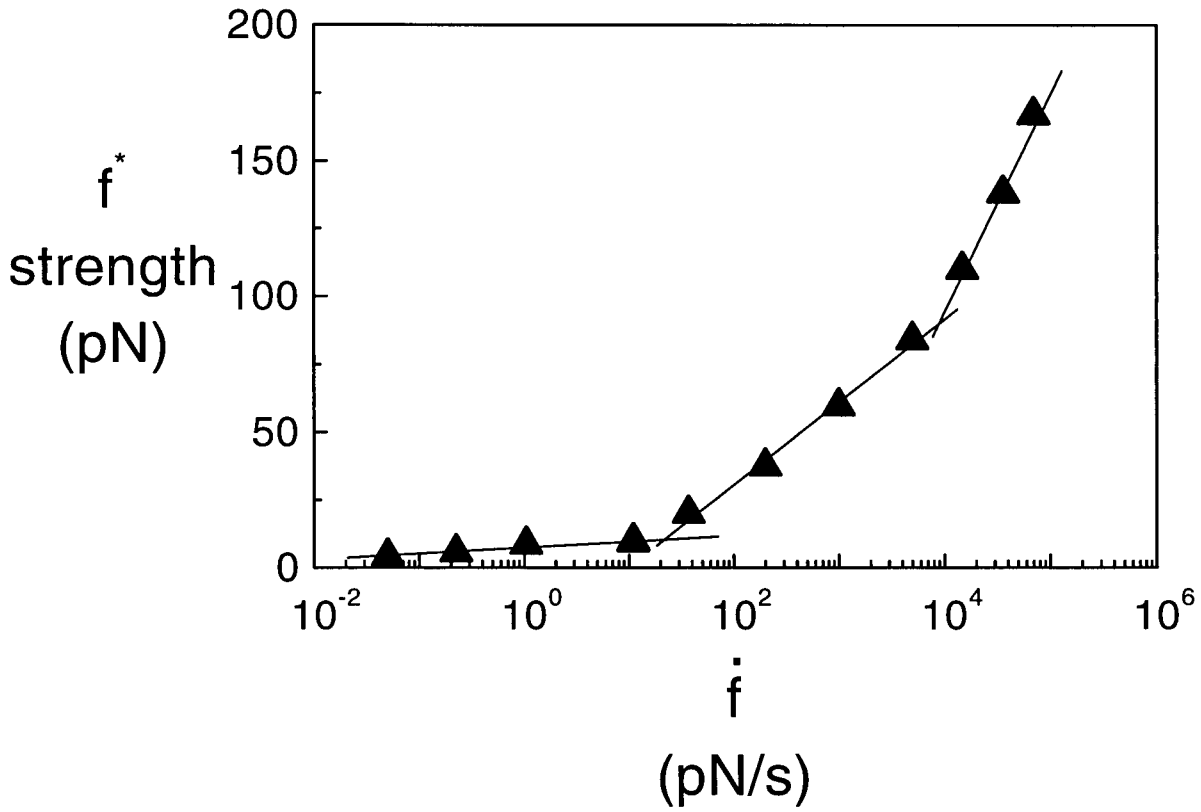

Figure 10.16: Bond Strength Spectrum.
Bond strength vs. the logarithm of the loading rate $\dot{f}$ for the biotin-avidin linkage at a loading rates spanning 5 orders-of-magnitude. Three distinct linear regions are easily noticeable.

Chapter 11

Introduction to Bond Strength Analysis

How does one define, and what determines, the strength of a weak chemical bond? This section of the thesis is concerned with the physical mechanisms and properties that determine strength in a weakly bonded molecular assembly. By weakly bonded system, it is meant that the binding energy is on the order of tens of the thermal energy, k_BT. With the exception of the covalent linkages defined as strong bonds, such as the backbone of protein molecules, all molecules and macromolecular assemblies in biology interact through weak interactions in an aqueous environment. A prominent example of weak bonds are molecular connections in cell-cell and cell-substrate adhesion.

Realizing that the force is ramped in time in experimental measurements of bond strength, through extension of a spring, the kinetics of bond dissociation must first be examined. Elucidating the important factors in the rate of simple chemical reactions (specifically chemical dissociation) has been a goal since the early work of Van't Hoff and Arrhenius in the late 19^{th} century. Empirically, the reaction rate follows the *Arrhenius* formula $k \sim \exp(-E/k_BT)$. Reaction rate theory was studied intensely in the early part of this century. Major theoretical contributions were made independently by both Eyring (Eyring, 1935) and Kramers (Kramers, 1940) (see the review by Hänggi *et al.* , 1990, for a detailed history of reaction rate theory).

The reaction rate theory of Eyring is rooted in quantum statistical mechanics. Eyring proposed the existence of an activated, or transition state along a single pathway between reactants and products. The transition state occurs at the saddle point in the energy

landscape of the decomposition (unbonding) process. Summing of the allowed translational, rotational and vibrational degrees of freedom in the reactant well and at the transition state yields the partition function for each state. This allows one to calculate the likelihood of reaching the transition state.

Eyring derived a reaction rate k of the form

$$k = \kappa \left(\frac{\mathcal{Z}^*_{TS}}{\mathcal{Z}_R} \right) \left(\frac{k_B T}{h} \right) \exp(-E_b / k_B T) \tag{11.14}$$

where $\mathcal{Z}_R$ is the partition function for the reactants including all their allowed translational, rotational and vibrational degrees of freedom, taken from ideal gas formulations. $\mathcal{Z}^*_{TS}$ is the partition function for the activated complex formed at the energy barrier, of height E_b. $\mathcal{Z}^*_{TS}$ does not include the degree of freedom through which the dissociation takes place. The factor $k_B T/h$ is a universal frequency that accounts for the thermalization of vibrational degrees of freedom for the activated complex along its reaction coordinate. The prefactor κ is to take into account that not all reactants that reach the transition state continue to the product state. Eyring's reaction rate theory is commonly known as *transition state theory* when $\kappa = 1$. For a simple one-dimensional system, the transition state theory predicts a reaction rate of

$$k_{TST} \approx \nu_0 \exp(-E_b / k_B T) \tag{11.15}$$

where ν_0 is set by the frequency of oscillations of the reactants in their potential well.

Eyring's formulation breaks down in liquid environments, where, due to damping, the frequency along the decomposition coordinate *in vacuo* is strongly modified. There can be many recrossings of the transition state during an escape attempt in a liquid. Kramers remedied this in his landmark paper of 1940 (Kramers, 1940).

Kramers considered the escape of a particle in a dissipative environment over an energy barrier due to Brownian impulses. The escape over a barrier models the dissociation

of a chemical bond in a viscous, liquid environment. Kramers determined the constant flux of thermalized particles out of the reactant well in an overdamped system. As a result the reaction rate was found as

$$k \approx \frac{\sqrt{\kappa_a \kappa_b}}{\gamma} \exp(-\beta E_b) \tag{11.16}$$

where E_b is the energy of the barrier to dissociation and $\beta \equiv (k_B T)^{-1}$ is the inverse of the thermal energy. The curvatures, κ_a and κ_b, represent the curvature of the potential about the bound and transition states, respectively (both are taken positive-valued). The prefactor in the rate of reaction is determined by the environment through the diffusivity γ of the solvent which is related to the diffusion constant through the Einstein relation, $D = k_B T/\gamma$. This explained why $k_B T/h$ was anomalously high in Eyring's expression and extended reaction rate theory to include reaction kinetics in liquids.

Since their pioneering work, no one has proposed an in-depth look at the force driven dissociation of weak molecular bonds. A phenomenological model was proposed by Bell (Bell, 1978) for the breakage of weak biochemical bonds. Bell had realized the importance of force in assisting the dissociation of molecular linkages. Using an Arrhenius-like relation, Bell proposed that the energy barrier would be decreased by an energy equal to $F \cdot x_b$ where F is the load applied to the bond and x_b is the assumed stationary effective length of the bond.

$$k = k_0 \exp\left[-\beta(E_b - F \cdot x_b)\right] \tag{11.17}$$

Even this simple *ad hoc* equation underlines the importance of an applied force on dissociation of a bond.

Bell had also realized that the time scale was important to the measured strength of a bond, remarking that a bond will dissociate even under zero force if given long enough. He never pursued the stochastic nature of bonding to define what is meant by *bond strength* as a consequence.

Chapter 12

Dissociation of Single Bonds

In order to model forced dissociation of weak biochemical linkages, a clear picture of the system is required. Consider two large molecules that only interact through complimentary parts. A specific realization may include a pocket in a receptor molecule that can house a small segment of the ligand molecule in such a way as to form an energetically favorable association. A weak bond formed between complimentary molecules may include such interactions as hydrogen bonds, ionic bonds, water bridges, hydrophobic interactions and steric effects, to name a few. These interactions combine to produce an energy landscape defining the bound state or a sequence of bound states. Now consider holding the receptor fixed and pulling on the ligand through a soft spring. The force, from the spring extension, is measured up to separation of the molecules and dissociation of the bond.

While bonded, the system is in a local energy minimum. As the molecules separate, they pass over an energy maximum in the energy landscape defined as the transition state. For a complicated, three dimensional bonding scenario, the energy barrier will contain many hills and valleys. Although many routes to dissociation may exist, the path over the lowest energy saddle point along the energy ridge will be most likely. Under force, the particle can not rebond after separation, due to the drift to infinity as a result of the applied force. The density of particles in the free state is zero due to its infinite dilution. Force driven dissociation is thus a non-equilibrium process.

Following Kramers' lead (Kramers, 1940), dissociation is described through the thermally activated escape of a particle from an energy well (bound state) over an energy barrier (transition state) to a global energy minimum (free state) as shown in figure 12.17. The rate of dissociation is determined from a constant flux of particles out of the bound state to the infinitely dilute free state. The reaction coordinate x idealizes the path through which the particle leaves the potential well (*i. e.* the most likely dissociation path through the energy barrier landscape). If a force f is applied to dissociate the bond, the energy landscape tilts by the factor $-f \cdot x$ as shown in figure 12.18.

Two simplified bonding potentials are shown in figure 12.18. The first potential follows an inverse power law of the form $-E_b/x^n$ (*e. g.* $n = 6$ for a van der Waals type interaction between point particles). The effect of the load on a power law bonding potential is three-fold. At low force, the major effect is that the transition state at x_{ts} shifts in towards the bound state at the local minimum at x_m from infinity. At higher force, there is considerable thinning of the barrier width about the transition state and a drop in barrier height. Next consider the harmonic well potential shown in figure 12.18 of the form $E_b(x-1)^2 - E_b, 0 \leq x \leq 2$. For this harmonic potential, the transition state is fixed and forms a sharp cusp under tension. As the force is increased the barrier height and width decreases and the position of the minimum travels outward toward the transition state.

Kramers theory is generalized to include dissociation under force. To simplify the form of the following equations, all variables are made unitless as follows: energies are normalized by k_BT, distances are normalized by a microscopic length x_a and forces are therefore scaled by a force $f_0 = k_BT/x_a$. The particle is thermalized within the potential well that forms the bond. The number of states to escape the potential well per unit time, J, along the reaction coordinate x in an overdamped environment follows a Smoluchowski

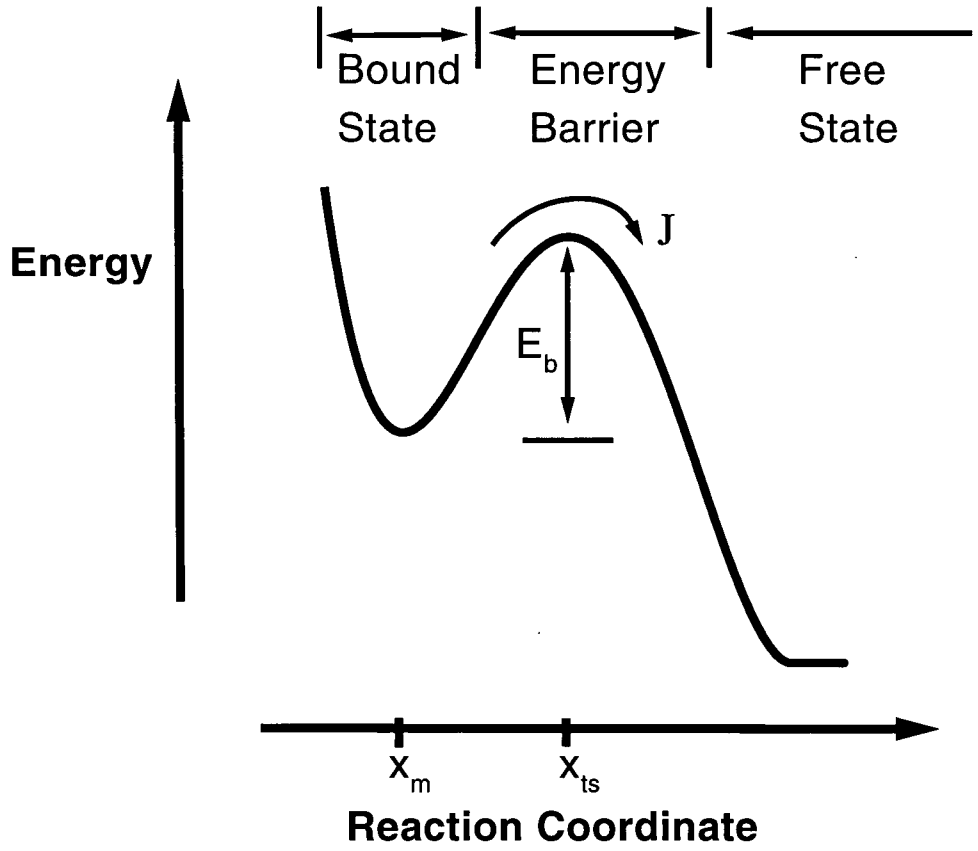

Figure 12.17: Energy Landscape of a Bound System.
In Kramers' approach, bond dissociation is described through a flux, J, of particles from a thermalized bound state at the local minimum at x_m, over an energy barrier E_b at x_{ts} to a global energy minimum in the free state.

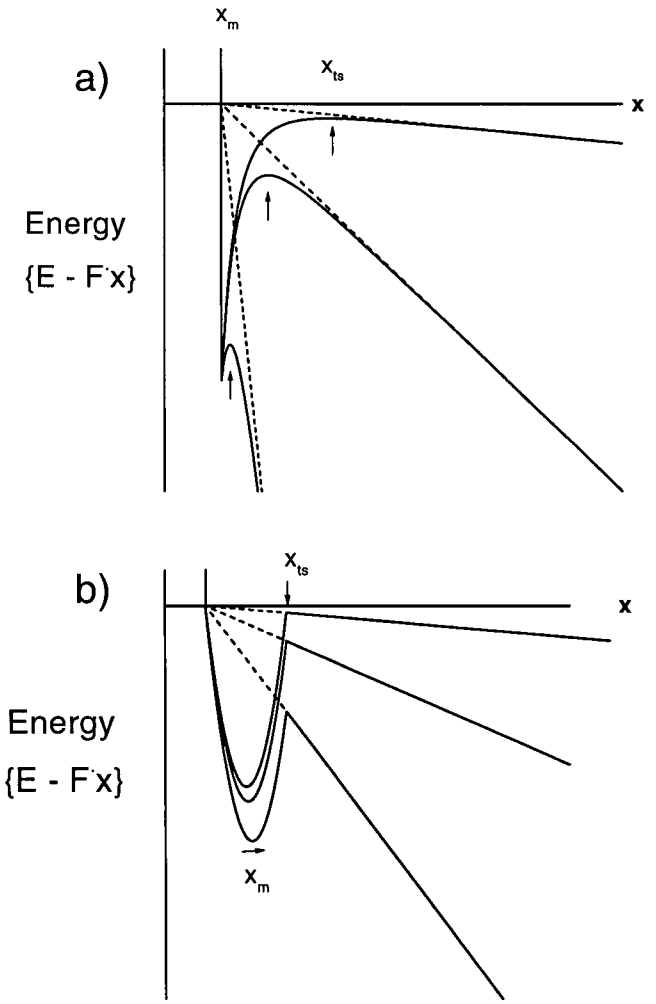

Figure 12.18: Effect of Applied Load on the Energy Landscape.
The applied load tilts the energy profile by $-f \cdot x$ as shown for an a) inverse power law and b) harmonic well potentials. The applied tension lowers the energy barrier, thins the barrier and draws the bound state at x_m and transition state at x_{ts} together.

equation of the form

$$J = D[(f - \frac{\partial E}{\partial x})\rho - \frac{\partial \rho}{\partial x}] \tag{12.18}$$

where ρ is the density of states per unit length along the reaction coordinate and D (made unitless by k_BT/x_a^2) is the (constant) diffusivity. For a stationary rate of escape of states from the bound state at x_m to a free state far away at x_f, integration of equation 12.18 yields

$$J = \frac{-\left(\rho e^{(E-f\cdot x)}\right)\Big|_{x_m}^{x_f}}{\int_{x_m}^{x_f} dx e^{(E-f\cdot x)}/D} \tag{12.19}$$

Because of the infinite dilution in the free state, the density of states is zero far from the transition state, $\rho(x_f) = 0$.

$$J = \frac{D\rho(x_m)e^{(E_m - f\cdot x_m)}}{\int_{x_m}^{x_f} dx e^{(E-f\cdot x)}} \tag{12.20}$$

$$= \frac{D\rho(x_m)e^{(E_m - f\cdot x_m - (E_{ts} - f\cdot x_{ts}))}}{\int_{x_m}^{x_f} dx e^{(E-f\cdot x-(E_{ts}-f\cdot x_{ts}))}} \tag{12.21}$$

introducing the energy, $E_{ts} - f \cdot x_{ts}$, at the transition state at x_{ts} in the exponentials in the numerator and denominator. The initial (zero-force) binding energy is set by the change in energy between the bound state and the transition state, $E_b = E_{ts} - E_m$. The density of states about x_m set the width of the bound state explored by a single particle through $\rho(x_m) = 1/l_a$. Applying a quadratic approximation with curvature κ_a to the energy profile of the well near its minimum

$$l_a = \int dx e^{(-\kappa_a x^2/2)} = \sqrt{2\pi/\kappa_a} \tag{12.22}$$

The integral in the denominator of equation 12.21 sets the diffusive length traveled across the energy barrier during escape as

$$l_b = \int_{x_m}^{x_f} dx e^{[\Delta(E-f\cdot x)_{ts}]} \tag{12.23}$$

with

$$\Delta(E - f\cdot x)_{ts} \equiv E(x) - E_{ts} - f(x - x_{ts}) \tag{12.24}$$

Thus a general form for the constant rate of escape of the states of a single particle called the offrate, commonly written as ν and equivalent functionally to J ($\nu = J$) is

$$\nu = \frac{D}{l_a l_b} e^{(-E_b + \Delta E_b(f))} \tag{12.25}$$

where $\Delta E_b = f(x_{ts} - x_m)$ gives the drop in barrier energy due to the applied force. We can rewrite equation 12.25 in a more informative form as

$$\nu = \nu_0 g(f) e^{\Delta E_b(F)} \tag{12.26}$$

where the function $g(f) \equiv 1/l_b(f)$ contains the force dependent barrier width and the prefactor $\nu_0 = (1/t_D)e^{-E_b}$ contains the Boltzmann factor for the likelihood of reaching the transition state under zero force scaled by the characteristic diffusive time $t_D \equiv l_a x_a / D$ for reaching the transition state. The prefactor of the offrate contains the diffusivity and hence sets the time scale of the unbonding. The dimensionless functions $g(f)$ and $\Delta E_b(f)$ are determined by the specific form of the potential well and transition state.

In order to study the effect of a strong hydrodynamic coupling, a position dependent diffusivity will be introduced. If the diffusivity depends on separation through a linear relationship such as for two spheres in close proximity (Batchelor, 1976),$D \approx D_0 x/\delta_0$, then the integral in the denominator of equation 12.19 that set $l_b(f)$ becomes

$$\frac{\delta_0 l_b}{D_0} = \int_{x_m}^{x_f} \frac{\delta_0 dx}{D_0 x} e^{[\Delta(E - f \cdot x)_{ts}]} \tag{12.27}$$

having an effect equivalent to increasing the dimensionality.

12.1 Inverse Power Law Potential

The first bonding potential to observe is that of a van der Waals-like attraction. This is an inverse power law of attraction defined as

$$E = \begin{cases} -E_b/x^n, & x \geq 1 \\ \infty & x < 1 \end{cases} \tag{12.28}$$

An exponent n of 6 corresponds to the van der Waals attraction between two small spheres. The minimum in this potential is a cusp at $x_m = 1$.

The transition state is defined as the maximum in the energy landscape described by $E - f \cdot x$. The position of the transition state is

$$x_{ts} = \left(\frac{f}{f_\infty}\right)^{\frac{-1}{n+1}} \tag{12.29}$$

where $f_\infty \equiv nE_b$ is the zero temperature strength of the bond.[1] This is the force at which the transition state and minimum coincide and hence the bonded state disappears. As expected the position of the transition state is force dependent.

The change in barrier height between the stationary well minimum and the transition state maximum at x_{ts} is

$$\Delta E_b = E_b\left[(n+1)(f/f_\infty)^{n/(n+1)} - n(f/f_\infty)\right] \tag{12.30}$$

The energy weighted width of the barrier l_b is found by saddle point integration of equation 12.23 about the transition state,

$$l_b \approx \sqrt{\frac{2\pi}{(n+1)f_\infty}} \cdot \left(\frac{f}{f_\infty}\right)^{\frac{-(n+2)}{2(n+1)}} \tag{12.31}$$

Thus, the one-dimensional constant diffusivity dissociation of an inverse power law type bond has an offrate given by

$$\nu(f) = \nu_0\sqrt{\frac{(n+1)f_\infty}{2\pi}} \cdot \left(\frac{f}{f_\infty}\right)^{\frac{n+2}{2(n+1)}} e^{E_b\left[(n+1)(f/f_\infty)^{n/(n+1)} - n(f/f_\infty)\right]} \tag{12.32}$$

The length l_a in the prefactor ν_0 of the offrate reflects the width explored in the potential well by the bonded particle. This is approximated as the width over which the potential well rises by k_BT about the minimum x_m. Thus

$$l_a \approx 1 - \left(\frac{E_b}{E_b - 1}\right)^{\frac{1}{n}} \approx \frac{1}{nE_b} \tag{12.33}$$

[1] Recall that all parameters are made unitless through the length x_a, the thermal energy k_BT and the force k_BT/x_a.

For large n the offrate closely follows the simple relation

$$\nu = \nu_0 \sqrt{(f/f_\beta)} e^{f/f_\beta} \tag{12.34}$$

where the thermal force f_β is the force required to lower the barrier height by $k_B T$ ($f_\beta \approx n/\{(n+1)[(n+1)E_b]^{1/n} - (n+1)\}$)

Consider the scenario where the bound particles have a strong hydrodynamic interaction through a diffusivity that changes with distance as $D = D_0(x/\delta_0) \approx D_0(x/l_a)$. The inclusion of a separation dependent diffusivity manifests itself as an effective increase in dimensionality, causing a modification to the apparent energy barrier. There is a shift in the position of the transition state defined as the maximum in $E - f \cdot x - \ln x$. The new transition state $x_{ts'}$ is found through numerical solution of

$$x_{ts'}^n = nE_b - f x_{ts'}^{n+1} \tag{12.35}$$

The reduction in the barrier height due to the separation dependent diffusivity at $x_{ts'}$ is modified to

$$\Delta E_b = f \cdot \left[\frac{n+1}{n} x_{ts'} - 1\right] + \ln(x_{ts'}) + \frac{1}{n} \tag{12.36}$$

The effective width of the transition state is found as

$$l_b \approx \frac{\sqrt{\frac{2\pi}{n}} x_{ts'}}{f x_{ts'} + n} + e^{-\frac{(f x_{ts'})^2}{f x_{ts'} + n}} \ln(1 + \frac{1}{f x_{ts'}}) \tag{12.37}$$

The offrate in one dimension with strong hydrodynamic coupling for an inverse power law potential is given by combining equations 12.35, 12.36 and 12.37 in the general formula given in equation 12.26.

12.2 Harmonic Well Potential

The inverse power law bonding potential of the previous section describes a soft, rounded energy profile about the transition state. To examine a sharp, cusp-like transition state,

the bonding potential is taken to be quadratic in profile

$$E = \begin{cases} \infty & x < 0 \\ E_b(x-1)^2 - E_b & 0 \leq x \leq 2 \\ 0 & x > 2 \end{cases} \tag{12.38}$$

Under vanishing force this describes a bound state with a barrier height of E_b, a minimum at $x_m = 1$ and a transition state at $x_{ts} = 2$ (unitless dimensions).

The transition state is kept stationary at all forces. The minimum is weakly shifted under increasing force toward the transition state as $x_m = 1 + f/f_\infty$, $f_\infty \equiv 2E_b$. The reduction in the barrier height relative to the shifted minimum under load f is

$$\Delta E_b = 2E_b \left[\left(\frac{f}{f_\infty} \right) - \frac{1}{2} \left(\frac{f}{f_\infty} \right)^2 \right] \tag{12.39}$$

Due to the sharpness of the cusp-like transition state, the diffusivity can be assumed constant across the barrier. The energy weighted width of the cusp-like barrier is found through

$$l_b = I_q + \frac{1}{f} \tag{12.40}$$

where I_q is the part of the integral in equation 12.23 below the transition state that needs to be numerically integrated.

$$I_q = \int_0^{1-f/f^\infty} dy e^{E_b y^2 - (2E_b - f)y} \tag{12.41}$$

In one dimension the quadratic well with the cusp transition state predicts an offrate that goes as

$$\nu = \nu_0 \frac{1}{I_q + 1/f} e^{2E_b[(f/f_\infty) - (f/f_\infty)^2/2]} \tag{12.42}$$

where ν_0 is set through $l_a \approx \sqrt{\pi/E_b}$. A linear approximation to the integral below the transition state in equation 12.41 gives an offrate close to

$$\nu = \nu_0 (f/f_\beta) e^{f/f_\beta} \tag{12.43}$$

with a thermal force scale of k_bT, $f_\beta \approx 1 + E_b/4$.

12.3 Effect of a Linear Loading Rate

Experimentally, force is applied through extension of a spring to load the bond. As the spring base is retracted, the tension on the bond increases linearly in time through $f = kvt$ where k is the spring constant of the force measuring apparatus and v is the velocity of retraction of the spring base. Rates of loading $\dot{f} = kv$ of experimental techniques range from 1–10 pN/s for optical tweezers, 1–10^4 pN/s for the probe technique described in Part I and 10^4–10^5 pN/s for the atomic force microscope. Molecular dynamics simulations can only consider extreme loading rates of 10^{12} pN/s.

Application of force in the laboratory occurs at time scales (10^{-3} – 1 s) much slower than the relaxation time for thermal impulses ($< 10^{-12}$ s). This separation of time scales allows us to represent the likelihood of bond dissociation under force as a first-order kinetic process with a time- and, hence, force-dependent rate of dissociation, $\nu[f(t)]$ The probability of bond dissociation is a product of the probability of bond survival and the probability density for failure at a given force. The probability density for bond failure at a force f is

$$P(f) = \frac{\nu(f)}{\dot{f}} e^{-\int_0^f \nu(f')\frac{df'}{\dot{f}}} \tag{12.44}$$

where the force depends on time through $f = \dot{f}t$. The general offrate of equation 12.26 yields

$$P(f) = \frac{g(f)}{r_f} e^{\Delta E_b(f)} e^{-\frac{1}{r_f}\int_0^f g(f')e^{\Delta E_b(f')}df'} \tag{12.45}$$

where $r_f \equiv \dot{f}/f_0\nu_0$ is the dimensionless loading rate.

Using the approximate offrate for escape from a quadratic well ($\nu = \nu_0(f/f_\beta)e^{f/f_\beta}$), figure 12.19 shows examples of the probability density at varying loading rates. The appearance of a peak is solely due to the time-dependent loading of the bond. If a constant force is applied instantaneously at time zero, bond survival is a simple exponential decay in time given by $P(t) \sim \exp(-\nu(f) \cdot t)$. The magnitude of a constant tension sets the

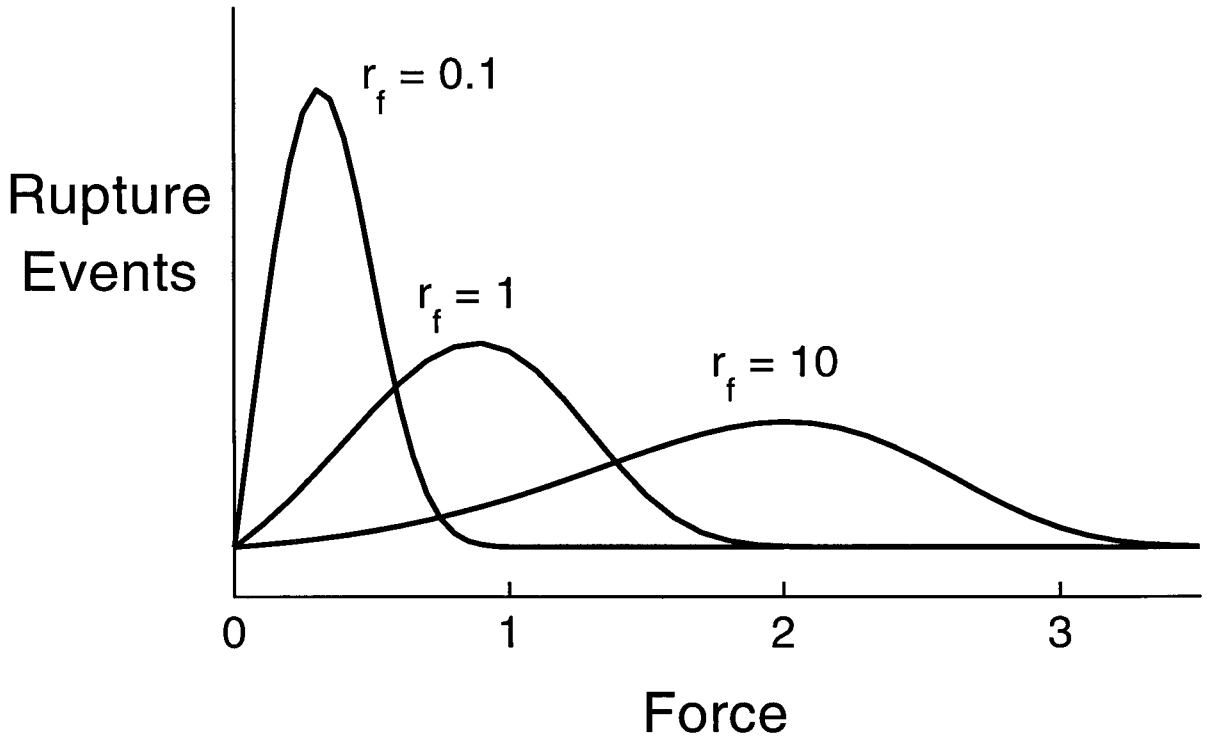

Figure 12.19: Theoretical Probability Density for Bond Rupture Strength.
As the dimensionless rate r_f is increased the distribution shifts to greater dimensionless forces. Also, there is a real width to the distribution at all rates. The strength, in units of f_0 is defined as the position of the peak in the profile.

mean lifetime of the bond only. The coupling of the force and time produce the peak in the distribution. The value of the force at the peak is termed the *strength* of the bond $f^\star$. Note there is a real width to the probability density. This width is a consequence of the finite temperature Brownian motion that drives the bond to dissociation.

The most striking feature of the probability density is the dependence of strength $f^\star$ on the dimensionless loading rate r_f. At faster loading rates the bond survives for shorter times but exists to higher forces due to the temporal nature of bond dissociation. The strength, $f^\star$ determined by $\partial P/\partial f = 0$ is found by solving

$$\left.\frac{\nu}{\nu_0}\right|_{f=f^\star} = r_f \left.\frac{\partial \ln \nu}{\partial f}\right|_{f=f^\star} \tag{12.46}$$

which, for the general offrate in equation 12.26, is equivalent to solving

$$\ln r_f = \Delta E_b(f^\star) + \ln g(f^\star) - \ln\left(\frac{\partial \ln g(f)}{\partial f} - \frac{\partial \Delta E_b(f)}{\partial f}\right)_{f=f^\star} \tag{12.47}$$

for the strength $f^\star$ as a function of the dimensionless loading rate. From the simplified approximations to the offrates for the inverse power law (IPL) and harmonic well (HW), the strength can be found by solving

$$\ln r_f = \begin{cases} \frac{f^\star}{f_\beta} + \frac{1}{2}\ln\left(\frac{f^\star}{f_\beta}\right) - \ln\left(\frac{1}{2f^\star/f_\beta} - 1\right) & \text{(IPL)} \\ \frac{f^\star}{f_\beta} + \ln\left(\frac{f^\star}{f_\beta}\right) - \ln\left(\frac{1}{f^\star/f_\beta} - 1\right) & \text{(HW)} \end{cases} \tag{12.48}$$

The loading rate dependence of the strength predicts a slow loading regime where the strength depends polynomially on rate. At higher rates, a universal regime where the strength of the bond is directly dependent on the logarithm of the loading rate. The full curves are shown with the analysis of the computational experiments of the next section.

Chapter 13

Computational Experiments

13.1 Monte Carlo Methods

The previous section predicts many striking features involved in force-driven dissociation of weak bonds. To verify these predictions, and expose more subtle features, a two-particle Monte Carlo-based (MC) simulation was performed. The MC-based algorithm allows the computational speed required to adequately generate approximations to the bond strength probability distributions for loading rates spanning 8 orders-of-magnitude.

The MC-based algorithm was designed to simulate Brownian dynamics equivalent to a viscous-limited Langevin equation of motion. The Brownian dynamics algorithm was derived from a Metropolis-like algorithm (Metropolis and Ulam, 1949) extended to include the random effects of the surrounding solvent molecules and drift though the solvent due to gradients in the local potential. As such, the simulation keeps correct temporal information where the time scale is set by the particle diffusivity and dimension. The algorithm was labeled the Smart Monte Carlo (SMC) scheme by its creators, Rossky, Doll and Freidman (Rossky *et al.*, 1978).

13.1.1 The Metropolis Method

To understand the SMC algorithm, one must begin with the basics of the classic Metropolis MC method. A Markovian chain of events is constructed in the MC simulation. The

MC algorithm requires a transition matrix T that satisfies

$$\sum_i \rho_i T_{ij} = \rho_j \tag{13.49}$$

$$\sum_j T_{ij} = 1 \tag{13.50}$$

where matrix element T_{ij} holds the probability of a change in state from i to j and ρ_i is the limiting probability of being in state i at long times (*i. e.* in equilibrium). In thermodynamic equilibrium, the limiting probability of being in state i is

$$\rho_i = \mathcal{Z}^{-1} \exp(-\beta U_i) \tag{13.51}$$

where $\mathcal{Z}$ is the partition function, β is the inverse of the thermal energy ($\beta = 1/k_B T$) and U_i is the energy of state i. Thus the ratio (ρ_j/ρ_i) is the Boltzmann factor for the transition

$$(\rho_j/\rho_i) = \exp(-\beta \Delta U_{ji}) \tag{13.52}$$

where ΔU_{ji} is the change in energy due to the transition.

Commonly, the strong constraint of microscopic reversibility is imposed. This requires, using summation notation,

$$\rho_i T_{ij} = \rho_j T_{ji} \tag{13.53}$$

Metropolis, *et al.*, (1953) proposed a solution to the transition matrix of the form

$$\begin{aligned} T_{ij} &= \alpha_{ij}, & \rho_j &\geq \rho_i, \quad i \neq j \\ T_{ij} &= \alpha_{ij}(\rho_j/\rho_i), & \rho_j &< \rho_i, \quad i \neq j \\ T_{ii} &= 1 - \textstyle\sum_{j \neq i} T_{ij} \end{aligned} \tag{13.54}$$

where α is an underlying stochastic matrix that must be symmetric. The transition matrix defined as above ensures microscopic reversibility.

The Metropolis method chooses a transition matrix to satisfy the strong condition of microscopic reversibility. Conventionally, the symmetrical matrix α_{ij} is uniform for

transitions to nearby states and zero for transitions to far states (*i. e.* a particle may move with equal likelihood within a small sphere about its current position). The acceptance of the transition is then set entirely by the energy of the transition. Energetically favorable transitions occur unconditionally. If the energy change is unfavorable the transition is accepted if $\exp(-\beta\Delta U_{ij})$ is greater than a random number chosen uniformly between 0 to 1. Using the FORTRAN statement `min`, as is commonly done, the probability of the transition occurring is $\texttt{min}(1, \exp(-\beta\Delta U_{ij}))$. Thus, the more unfavorable the energy, the less likely the excess energy can be taken from a hypothetical heat bath.

This prescription ensures averages of variables reach their correct thermodynamic limits at long times. It does not, however, provide useful information about the path with which they arrived at that limit.

13.1.2 The Smart Monte Carlo Method

Based upon the earlier work of Ermak (Ermak, 1975a, Ermak, 1975b), Doll and Dion (Doll and Dion, 1976), and Turq *et al.* (Turq *et al.*, 1977) employing Brownian dynamics to replace the solvent in molecular dynamics simulations, Rossky *et. al.* (Rossky *et al.*, 1978) developed the smart Monte Carlo (SMC) algorithm. In this prescription, the embedding solvent is taken into account by requiring the particles obey the overdamped Langevin equation

$$F = \Gamma\dot{x} + \mathcal{F} \tag{13.55}$$

where $\Gamma = k_B T/D$ is the friction coefficient associated with the diffusivity D. The force $F = -\nabla U$ is the gradient of the potential local to the particle and $\mathcal{F}$ is a stochastic force due to the thermal bombardment of the solvent. The stochastic force obeys the fluctuation-dissipation theorem.

$$\langle \mathcal{F}(t)\mathcal{F}(0)\rangle = 2\Gamma k_B T\delta(t) \tag{13.56}$$

$$\langle \mathcal{F}(t) \rangle = 0 \tag{13.57}$$

Bond dissociation in a liquid environment is an overdamped system and as such has no inertial term in equation 13.55. To satisfy the Langevin equation, the positional change of the particle at each time step is determined by

$$\Delta x = D\Delta t\beta F + X \tag{13.58}$$

where X is a Brownian based random step chosen in d dimensions from the distribution

$$W(X) = (4D\Delta t)^{-d/2} \exp(-X^2/4D\Delta t) \tag{13.59}$$

and where Δt is the time passed during the step. As $\Delta t \to 0$, the simulation goes exactly to the overdamped Langevin equation.

The underlying matrix of the transition is predicated on the likelihood of obtaining the Brownian based random step

$$\alpha_{ij} = \frac{\int dX W(X)\delta(\Delta x_{ij} - D\Delta t\beta F_i - X)}{\int d\Delta x \int dX W(X)\delta(\Delta x - D\Delta t\beta F_i - X)} \tag{13.60}$$

where $\Delta x_{ij} = x_j - x_i$ is the change in position of the particle during the time step. The choice of α_{ij} in equation 13.60 is not symmetric. To preserve microscopic reversibility the transformation matrix is modified to

$$\begin{aligned} T_{ij} &= \alpha_{ij}, & \alpha_{ji}\rho_j &\geq \alpha_{ij}\rho_i, \quad i \neq j \\ T_{ij} &= \alpha_{ij}(\alpha_{ji}\rho_j/\alpha_{ij}\rho_i), & \alpha_{ji}\rho_j &< \alpha_{ij}\rho_i, \quad i \neq j \\ T_{ii} &= 1 - \textstyle\sum_{j\neq i} T_{ij} \end{aligned} \tag{13.61}$$

where ρ_i is the Boltzmann factor as before.

The recipe for evolving the SMC simulation by one time step is shown in figure 13.20. Essentially, at the start of each time step, the force on a particle is calculated. The force, combined with a random Brownian displacement, sets a tentative new position which is

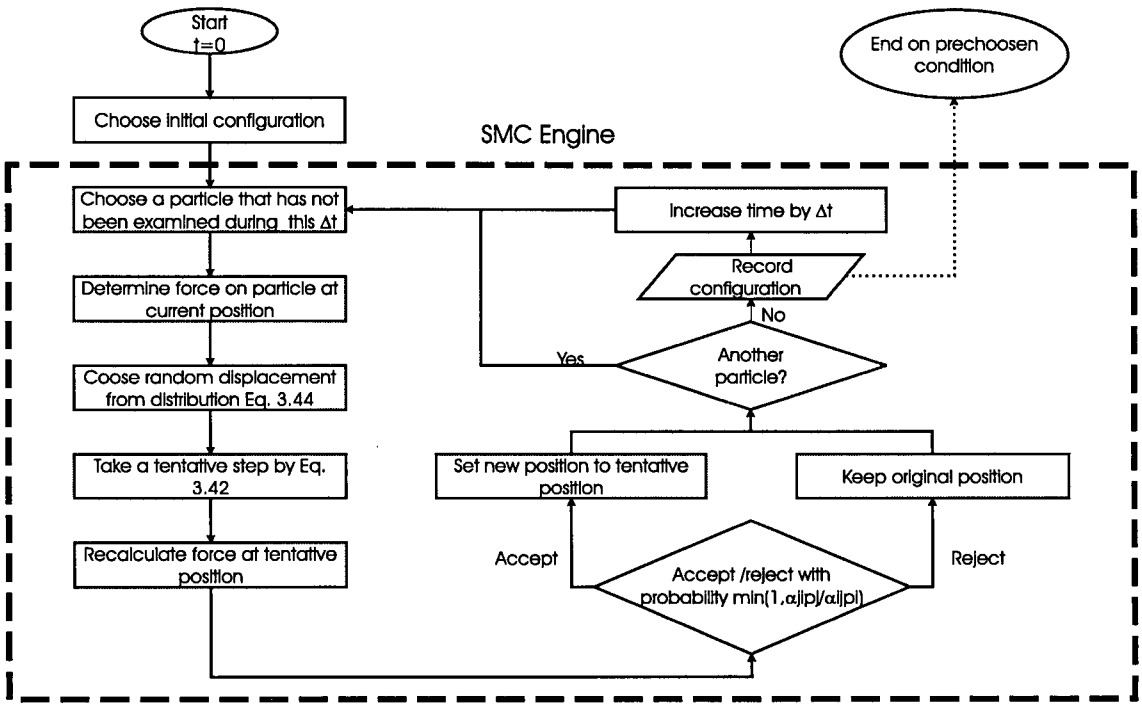

Figure 13.20: Flowchart of the SMC Algorithm.
This demonstrates the general SMC algorithm for a multi-particle simulation. The SMC engine ends on a prechosen condition, such as the breakage of a bond.

accepted or rejected with probability $\min(1, \alpha_{ji}\rho_j/\alpha_{ij}\rho_i)$. The transition matrix ensures that the evolution of the particle follows the overdamped Langevin equation with given diffusivity. The simulation is run until a prechosen condition is satisfied (*i. e.* that the particles have separated a given distance).

The magnitude of the time step in equation 13.58 and subsequent equations was chosen in the following simulations so that Δt was small with respect to the thermal force scale, f_β defined as the force required to lower the barrier by k_BT, over the force loading rate $\dot{f}$ ($\Delta t \ll f_\beta/\dot{f}$). Beyond that, choice of Δt generally follows the rule of thumb that too small a step takes too long to run the simulation and is unnecessary, and too large of a time step will cause the algorithm to reject too many steps and also slow down the algorithm. There is a wide range of time steps over which the simulation gives the same result on average. In order to span 8 orders-of-magnitude, the value of Δt was changed over a 100-fold at the slower rates. Overlap in loading rates was made between the two Δt values and no change in results were found.

13.1.3 Computational Single Bond Failure under Ramped Force

To explore the effect of force and the rate of loading on the failure of weak bonds, an idealized simulation was carried out, in which two particles bonded through a potential were separated under a force ramp in an overdamped environment. In each cycle of a simulation, one particle of radius $a/2$ was positioned stationary at the origin[1]. A mobile particle, of radius $a/2$, was set inside the bonding potential at the minimum of the potential well. The particle was allowed to equilibrate within a strongly attractive potential ($-80k_BT$ depth) for 1000 time steps prior to the beginning of the cycle. At the end of the equilibration period, the potential was changed to a prescribed depth of 5 k_BT. The force on the mobile particle was then increased linearly in time at a specified

[1]The diameter of the particles, a, set a natural length scale for the simulation.

loading rate.

Bond lifetime in a computational run was defined by the time when the mobile particle last transversed the transition state. The last passage was found by allowing the mobile particle to travel 10 times further away from the transition state before ending the simulation. The force at last passage was then found from the particle lifetime and force loading rate. Care was taken to use the last passage time as figure 13.21 shows the pitfall of defining the strength through the time of first passage across the transition state. In a liquid environment, the Brownian motion of the particle at the transition state causes the bound particle to recross the barrier frequently at the slower loading rates.

At each of the 55 loading rates spanning 8 orders of magnitude tested, 200 tests of bond dissociation were performed. The results were collected to form a force histogram at each rate. These histograms are statistical approximations to the strength probability distributions of chapter 12 and were analyzed to determine the strength of the bond (defined as the peak of the distribution) at each rate.

Two bonding potentials were investigated in these studies. The first potential was an inverse power law (IPL) attraction of the form

$$E = \begin{cases} -E_b/x^n, & x \geq 1 \\ \infty & x < 1 \end{cases} \tag{13.62}$$

in 1 and 3 dimensions where E_b was made unitless by k_BT. The power n was varied from 1 to 6 (only results for $n = 4$ are reported since the others show no new results). The depth of the potential was varied from 3 to 7 k_BT with predictable results (only results for $E_b = 5$ will be shown). The second binding potential was a quadratic well defined by

$$E = \begin{cases} \infty & x < 0 \\ E_b(x-1)^2 - E_b & 0 \leq x \leq 2 \\ 0 & x > 2 \end{cases} \tag{13.63}$$

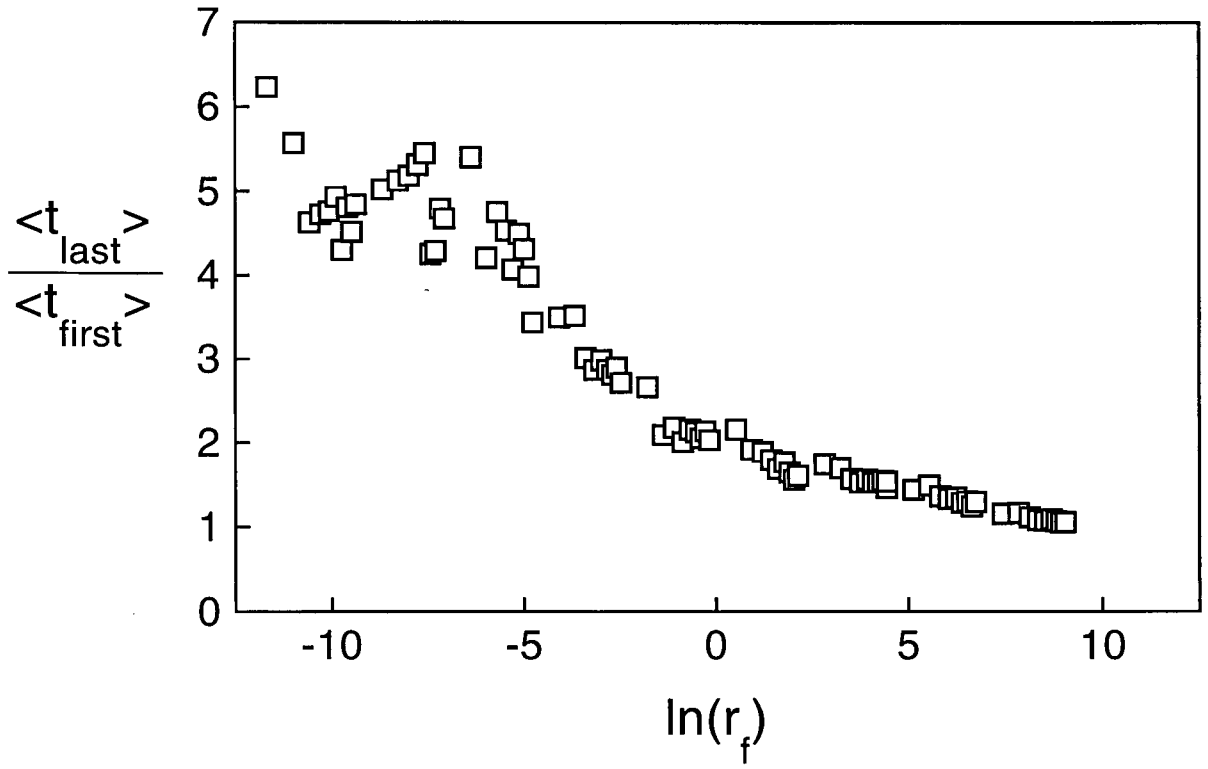

Figure 13.21: Comparison of Last to First Passage Time.
Shown is the ratio of the time when the mobile particle passes the transition state for the last and first time. At fast rates there is little difference between the two markers for bond dissociation (i.e. ratio of ~ 1). At low rates, the strength of the bond defined as the last passage is much greater than that defined by the first passage, by as much as 7 times. This is due to the strong effect of the solvent damping. The loading rate, r_f is in units of $\nu_0 f_0$.

in 1 dimension, where, again, E_b was set to $5k_BT$.

Hydrodynamic coupling of the two particles was studied by allowing the diffusion coefficient to be dependent on the radial distance between the particles which represents the stokes interaction between two spheres (Batchelor, 1976)

$$D = D_0 \frac{x}{\delta_0} \tag{13.64}$$

The parameter δ_0 was chosen to represent a small distance set as the minimum approach between the two test particles as the result of the thermal vibrations of the bonded pair. When this type of hydrodynamic coupling is included, the gradient of the diffusion coefficient must be added to the Langevin equation (see reference Doi and Edwards (1986) chapter 3 for an excellent discussion of Brownian motion and the Langevin equation). Thus, the modified equation of motion

$$F = \Gamma \dot{x} + \mathcal{F} + \frac{\Gamma}{2} \nabla D \tag{13.65}$$

was incorporated into the SMC algorithm.

13.2 Results

Computational experiments to determine the bond failure strength for two particle bound through the inverse power law in 1 and 3 dimensions, with and without the hydrodynamic coupling and for the quadratic well in 1 dimension with hydrodynamic coupling were performed. Each run of a computational experiment consisted of 200 bond dissociations where the force was increased at a given loading rate. A sample of the results at four different rates of loading is shown in figure 13.22. The solid lines are the predicted fits to the histograms. As already described in chapter 12 both the probability densities and the histograms display a rate dependent strength and at all rates of loading, both show a non-zero width.

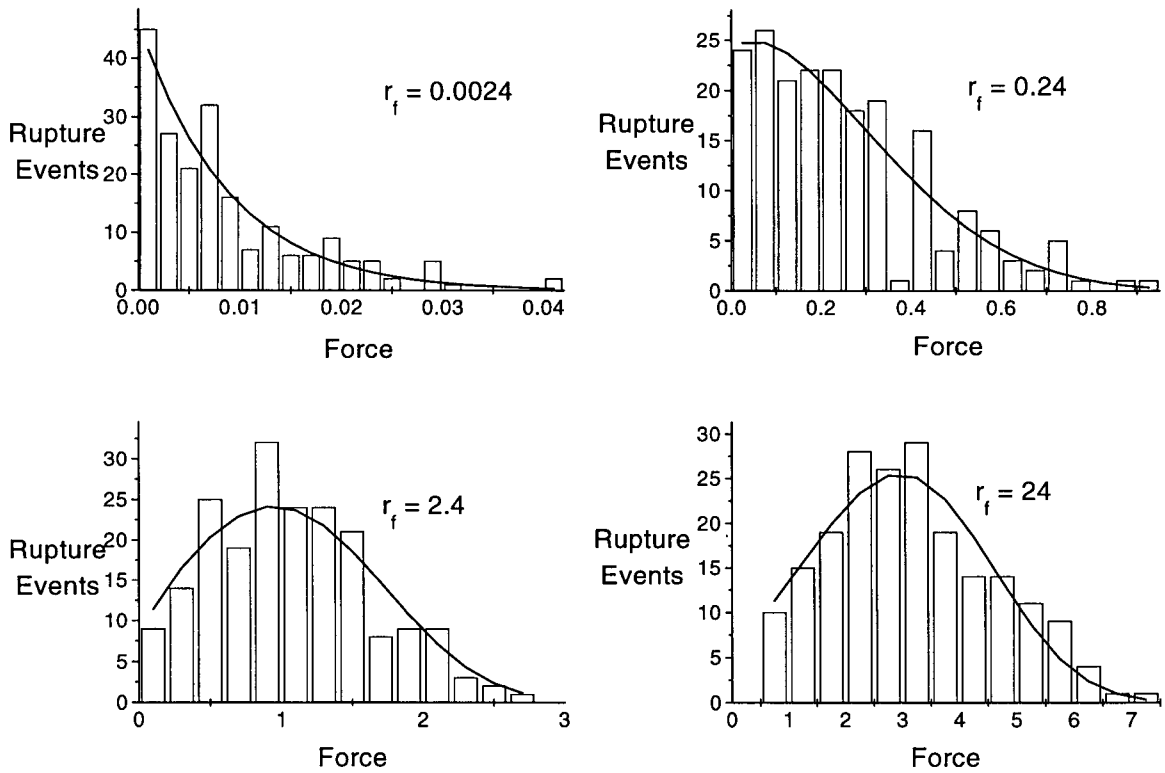

Figure 13.22: Force Histograms from Computational Experiments.
Each histogram contains the forces of rupture from 200 consecutive bond failures at the dimensionless rates shown. The bonding potential is the one dimensional harmonic well with hydrodynamic coupling. The solid lines are the predicted probability distributions from Chapter 12. Note the rate dependence of the strength, defined as the peak in the distribution. Also, the strength emerges at a rate between the lowest two rates shown. The loading rate, r_f is in units of $f_0\nu_0$ and the force f is in units of f_0.

A feature not previously mentioned is that at very low rates the breakage force histograms have no apparent peak where as the theory must go to zero probability of failure at zero force. This is due to the fact that Kramers' treatment breaks down at low force in one-dimension where the barrier width of equation 12.23 diverges. Three-dimensional characteristics of the unbonding kinetics and long range diffusion are usually taken into account in these situations (Hänggi *et al.*, 1990). Phenomenologically, spontaneous dissociation of an isolated bond can be postulated to be due to a transient repulsion resulting from the confinement of states to the region of strong attraction prior to the start of the bond breakage simulation. A small constant force f_i was added to the applied force (*i. e.* $\nu(f) \rightarrow \nu(f + f_i)$) to account for this transient repulsion. Spontaneous dissociation showed up in the breakage force histograms performed at very low rates where the histogram resembles an exponential-like decay. To determine if a peak exists in a breakage force histogram, it was necessary to examine this exponential-like decay. The decay parameter (in units of 1/force) multiplied by the loading rate provided an estimator of the apparent mean offrate. If the apparent mean offrate was independent of loading rate then the bond was in a regime where it was spontaneously dissociating and the loading rate must be below a critical rate where strength vanishes. As seen in figure 13.23 this apparent mean offrate is constant below a critical rate in the four cases shown — a) inverse power law with hydrodynamic coupling in 1-D, b) harmonic well with hydrodynamic coupling in 1-D, c) inverse power law without hydrodynamic coupling in 3-D, and d) inverse power law with hydrodynamic coupling in 3-D. The critical rates found through the apparent offrate corresponded to the rates where strength vanished in the force histograms, as will be seen in the coming section.

Dissociation force histograms were obtained from all sets of computational experiments spanning 8 orders-of-magnitude in force loading rate. The corresponding theoretical probability densities were fit to the histograms and the strength of the bond at

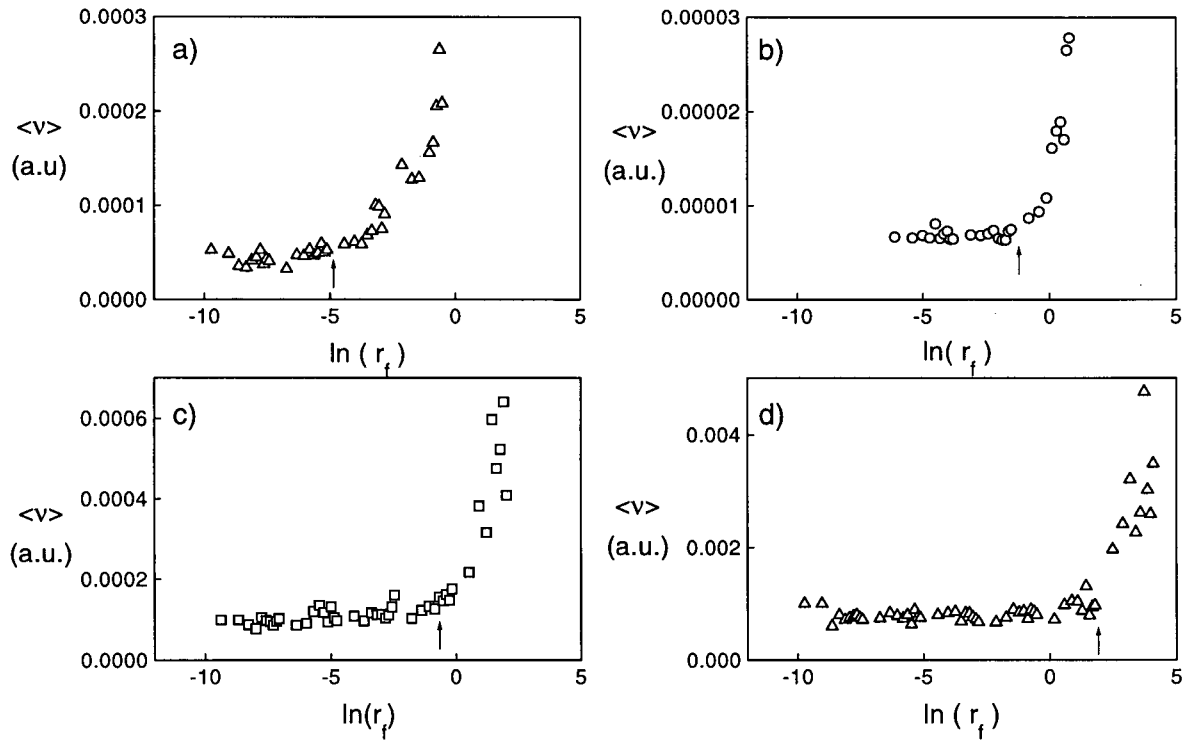

Figure 13.23: Apparent Offrate for Driven Dissociation.
The apparent offrate, defined as the reciprocal of the exponential decay time of the bond under the dynamic load, is shown for the a) inverse power law in 1-D with hydrodynamic coupling, b) harmonic well law in 1-D with hydrodynamic coupling, and c) and d) inverse power law in 3-D without and with hydrodynamic coupling, respectively. Note that there is a rate (arrow) below which the apparent offrate is approximately constant. The critical loading rate exposed through the apparent offrate is consistent with the critical loading rate at which strength vanishes in these systems. r_f is in units of $f_0\nu_0$.

Table 13.1: Intrinsic force as determined from the critical loading rates exposed in the various simulations performed. All forces are made dimensionless by $f_0 = k_B T/x_a$.

Bonding Potential	f_i
IPL, 1-D, no coupling	~ 0
IPL, 1-D, coupled	0.003
Quad, 1-D, coupled	0.18
IPL, 3-D, no coupling	0.32
IPL, 3-D, coupling	1.5

each rate was determined. Figure 13.24 exposes the effect of the rate of loading on bond strength for the inverse power law in 1-D without and with hydrodynamic coupling. Three plots are shown to display the different regimes of loading rates.

The solid lines in figure 13.24 are predicted curves from equation 12.47 derived using the simulation parameters (ν_0, f_0) and fitting for the intrinsic force f_i. The intrinsic force for all potentials tested are given in table 13.1. The hydrodynamically coupled case shows an onset of strength at a finite critical rate (see the log-log plot of figure 13.24). The intrinsic force found for the cases of figure 13.24 are ~ 0 for the absence of coupling and 0.003 for coupled particles. The intrinsic force here agrees with the critical rate found from the apparent offrate of figure 13.23.

A fast regime of loading is exposed in a linear-log plot of figure 13.24. The universal logarithmic regime where $\ln r_f \sim f$ is obvious and is comparable between both curves. A third ultrafast regime is shown in a linear-linear plot of figure 13.24. This regime displays a slight rate dependence on this scale and the previous details become compressed into a vertical line at $r_f = 0$. A maximum in strength is reached at high force loading rates . At these high rates, the transition state is completely overwhelmed nearly instantaneously.

Figure 13.25 compares the strength as found for the inverse power law potential well and the harmonic potential well in one dimension with strong hydrodynamic coupling.

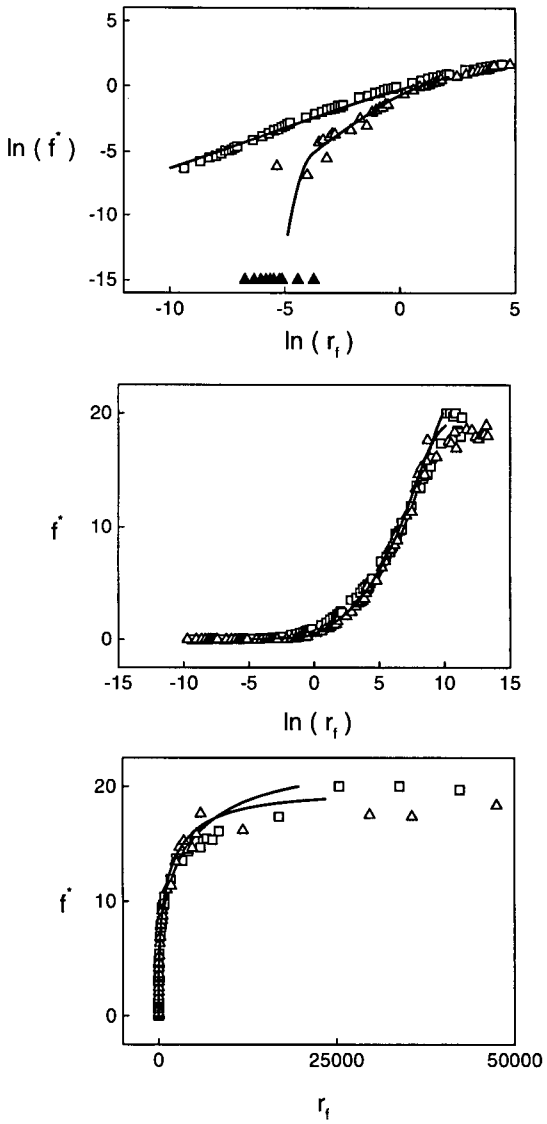

Figure 13.24: Strength of the Inverse Power Law Bond.
Comparison of the strength of the inverse power law bond in 1-D without (□) and with (△) hydrodynamic coupling. The lines are predictions from theory. Shown are a) a $\log(f^*) - \log(r_f)$, b) a $f^* - \log(r_f)$ and c) a $f^* - r_f$ plots. The closed symbols signify rates of loading with zero strength. The loading rate, r_f is in units of $f_0\nu_0$ and the force f is in units of f_0.

The predicted strengths are plotted as solid lines and agree with the computational results. The intrinsic force f_i is easily observed in the harmonic well case giving $f_i = 0.18$. The anomalous strength for the harmonic well potential at ultrafast loading rates (dashed line) is due to the stationary transition state. The minimum of the potential well travels to the transition state. The time for states to diffuse to the transition state accounts for the excess strength. This excess force in the ultrafast regime is not observed for the inverse power law well as the transition state moves to the minimum and the states need not diffuse to a stationary transition state to unbind.

Figure 13.26 shows the strength recorded from the computational experiments where the mobile particle is held in a 3-dimensional inverse power law potential with and without hydrodynamic coupling. The solid lines are predicted fits from the 1-D theory. The correspondence between the 3-D computational results and 1-D theory is not surprising. The application of tension along a direction tends to focus the escape trajectory about that direction. There is a saddle-point produced along the barrier in the direction of force. The path along the saddle-point becomes the most likely path of escape. At slow loading rates the focusing is not as strong. As a result the critical rate from the intrinsic repulsion force f_i is increased.

The addition of a strong hydrodynamic interaction increases the critical rate as expected due to an effective increase in dimension. This is also consistent with the inclusion of hydrodynamic coupling in 1-D bond dissociation where a critical rate emerges only in the presence of coupling.

13.3 Discussion

The results of the simple two atom Brownian dynamics simulation verify the theory of chapter 12. The prominent feature of the loading rate dependence of strength is the

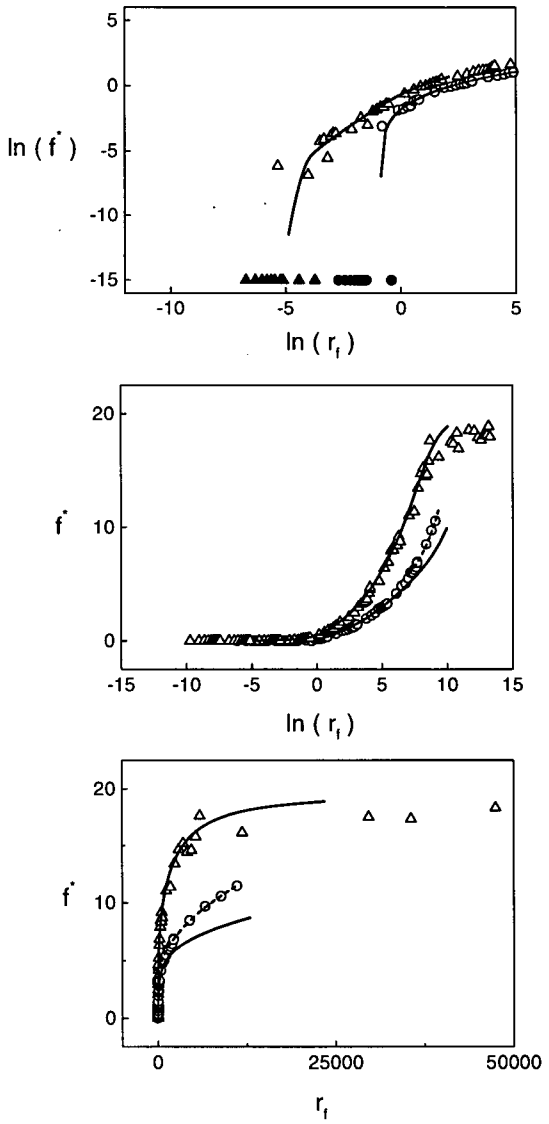

Figure 13.25: Comparison of Strength Between the Inverse Power Law and Harmonic Well Bond.
Both bonds (inverse power law (△) and harmonic well (◯) potential) are in 1-D and include hydrodynamic coupling. The lines are predictions from theory. Shown are a) a $\log(f^*) - \log(r_f)$, b) a $f^* - \log(r_f)$ and c) a $f^* - r_f$ plots. The closed symbols signify rates of loading with zero strength. The loading rate, r_f is in units of $f_0\nu_0$ and the force f is in units of f_0.

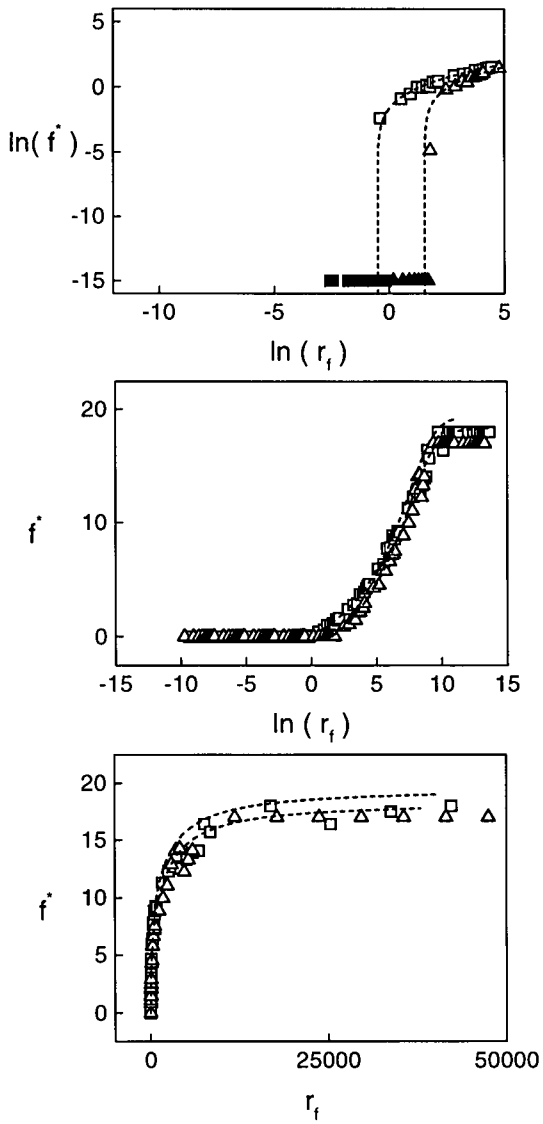

Figure 13.26: Strength of Inverse Power Law Bond in Three Dimensions.
Comparison of the strength of the inverse power law bond in 3-D without (□) and with (△) hydrodynamic coupling. The lines are predictions from theory. Shown are a) a $\log(f^*) - \log(r_f)$, b) a $f^* - \log(r_f)$ and c) a $f^* - r_f$ plots. The closed symbols signify rates of loading with zero strength.

universal logarithmic dependence of strength on loading rate in the fast regime. Further, the simulations expose the possibility of a critical rate, below which the bond has no strength by definition. Under force, the three dimensionality of a bond becomes hidden due to the strong focusing of the escape path along the direction of the applied force.

Early work on determining bond failure strength naively expected that the strength at which a bond fails would correspond to the steepest gradient in the bonding potential (Florin *et al.*, 1994; Lee *et al.*, 1994; Moy *et al.*, 1994). As such the loading rate was disregarded. As demonstrated experimentally in chapter 10 and through MC simulation in this chapter, the force loading rate is of paramount importance in bond strength measurements. In fact, the existence of a most frequent strength of a bond is a result of the ramped application of force.

All-atom, molecular dynamics (MD) simulations performed by Grubmüller *et al.* (Grubmüller *et. al.* , 1996) attempted to discern a rate dependent strength. Using the extreme rates required by MD and plotting a linear-linear plot (as in figure 13.26c), they found that the apparent strength weakly depended on loading rate. They extrapolated the strength to AFM loading rates and found good agreement with experiment. Further, a zero rate strength was found. Over the small range of extreme loading rates used ($\sim 10^{12}$ pN/s), the rate of the AFM ($\sim 10^{5}$ pN/s) is essentially zero. The erroneous weak dependence and zero rate strength are an artifact of the small range of loading rates examined. This underlines the importance of spanning several orders-of-magnitude in force loading rate, both computationally and experimentally.

13.4 Small-Number-of-Atom Simulation

The two-atom simulations of the previous sections provide an easy system for the verification of the theory of Chapter 12. They are a platform in which a well defined bonding

potential can be examined. The question arises as to how to develop a SMC simulation that more closely approximates the weak binding of two large (nm in size) molecules while retaining the simplicity to span many orders in magnitude of the loading rate.

In some real systems, the binding occurs through a binding pocket that may extend over several nanometers. The binding occurs through the proximity of the many atoms of the *key* of one molecule with the many atoms of the *lock* binding pocket on the opposing molecule. The pocket has its own flexibility that will effectively renormalize the potential seen by the *key*. Also, flaps and loops extraneous to the pocket can add to steric effects that are hard to take into account analytically. Klaus Shulten and co-workers recently performed an all-atom MD simulation of the driven dissociation of biotin from avidin (Izrailev *et al.*, 1997). The potential energy profile can be obtained from the positions of the biotin throughout its removal from the binding pocket (kindly provided by Klaus Shulten and co-workers, Beckman Institute, University of Illinois, from unpublished data pertaining to the paper (Izrailev *et al.*, 1997)). The soft spring used to extract the biotin in the simulation of Izrailev, *et al.*, will only minimally bias the potential.

The binding potential was calculated directly in the MD simulation of Izrailev *et al.* for a particular trajectory of the biotin out of the binding pocket as shown in figure 13.27a. There existed large, fast fluctuations in energy as a function of the position. Adjacent averaging of the potential with a 20 ps window in time smoothed the fast modes and leaved a much simpler looking dual well potential that was modeled using quadratic fits to the wells and spline interpolation in between, as displayed in figure 13.27b.

To handle multiple wells and to effectively pre-average over the fast modes, which would average out in the slower extraction of the biotin, a coarse, simple model of a multiple well binding pocket was constructed. This simple model took less computational run time than a full MD simulation and thus allowed a large span of loading rates to be explored in bond breakage tests. This simple model, termed a *small-number-of-atom*,

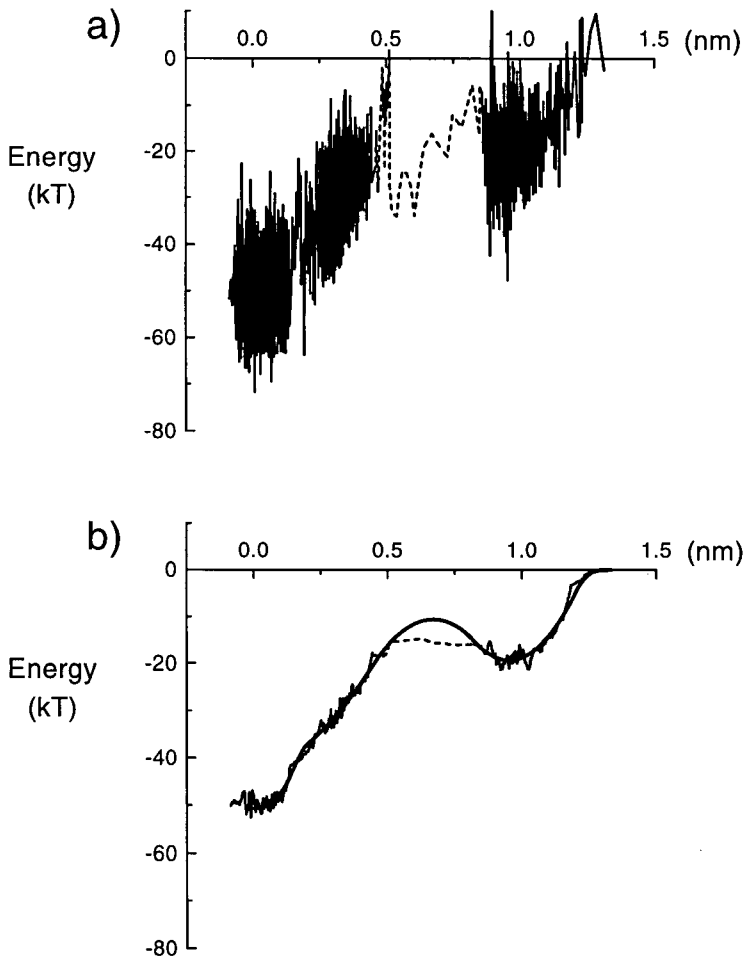

Figure 13.27: Potential Energy Profile for the Avidin-biotin System.
Generated by an all atom simulation of the driven dissociation of the biotin-avidin system (kindly provided by Klaus Shulten and co-workers, Beckman Institute, University of Illinois). Averaging out the local fast fluctuations in energy yields a smooth, dual well potential. Dashed lines denote interpolated areas with too few statistics to be calculated.

consisted of a can of 4 levels, each with 6 atoms, arranged in a hexagonal pattern. A 25^{th} atom plugged the bottom of the can and is anchored via a spring to its equilibrium point. The can is shown in figure 13.28. The can atoms were attached by Hookean springs between nearest neighbors around the can surface (cubic bonding).

A test particle is placed in the can and is allowed any type of weak interaction with the atoms of the can. Thus, different energies of interaction can be chosen between the test atom and each level of the can. This allows the user to build a multi-well potential landscape. The spring constant between can elements sets the fluctuation of the can (*i. e.* sets the effective temperature). In the following demonstrations, the test atom had an inverse power law interaction with the atoms of the can. The interaction was A/r^4 where r was the center-to-center distance between the test particle and any can particle, normalized to the diameter of a can particle, and the well depth at a distance of one diameter, set through A, was 3 k_BT for the bottom ring, 2 k_BT for the next closest ring and k_BT for the remaining top two rings.

The binding potential of the can $E(x)$ was calculated from the probability, $P(x)$, of finding the test atom at a position x through $E(x) = -\ln(P(x))$. Figure 13.29 shows a zero temperature potential created by the can (dashed line). In this configuration, the can atoms were stationary in the well defined initial cylindrical geometry of the can. The test particle was allowed to diffuse in the can for 100,000,000 steps. Figure 13.29 also shows the effect of increasing temperature (*i. e.* softening the springs) (solid line). There was a softening of the inner well and an increase in the main barrier height. The increase in barrier height was consistent with an increase in fluctuations around the mouth of the pocket. The test atom was sterically restricted from this region at times due to a closing of the top ring. As result, the particle would rather reside in the inner well.

Figure 13.30 shows the effect of freezing the can into a position that is a fluctuation about the starting position, in this case, the zero temperature configuration. The can

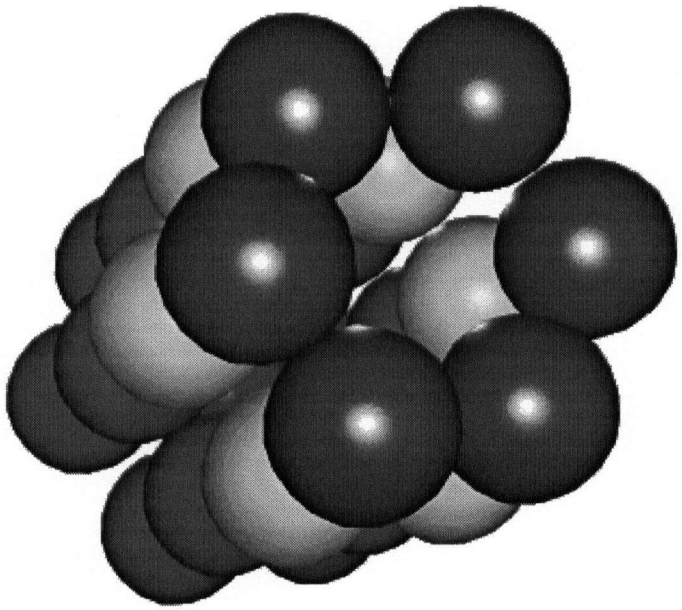

Figure 13.28: Geometry of Extended Simulation.
The 25 *atoms* shown form a can of hexagonal geometry. Ideal springs hold nearest neighbor atoms together giving the system vibrational freedom. Each of the can atoms can have a distinct interaction with a test particle placed inside the can (not shown).

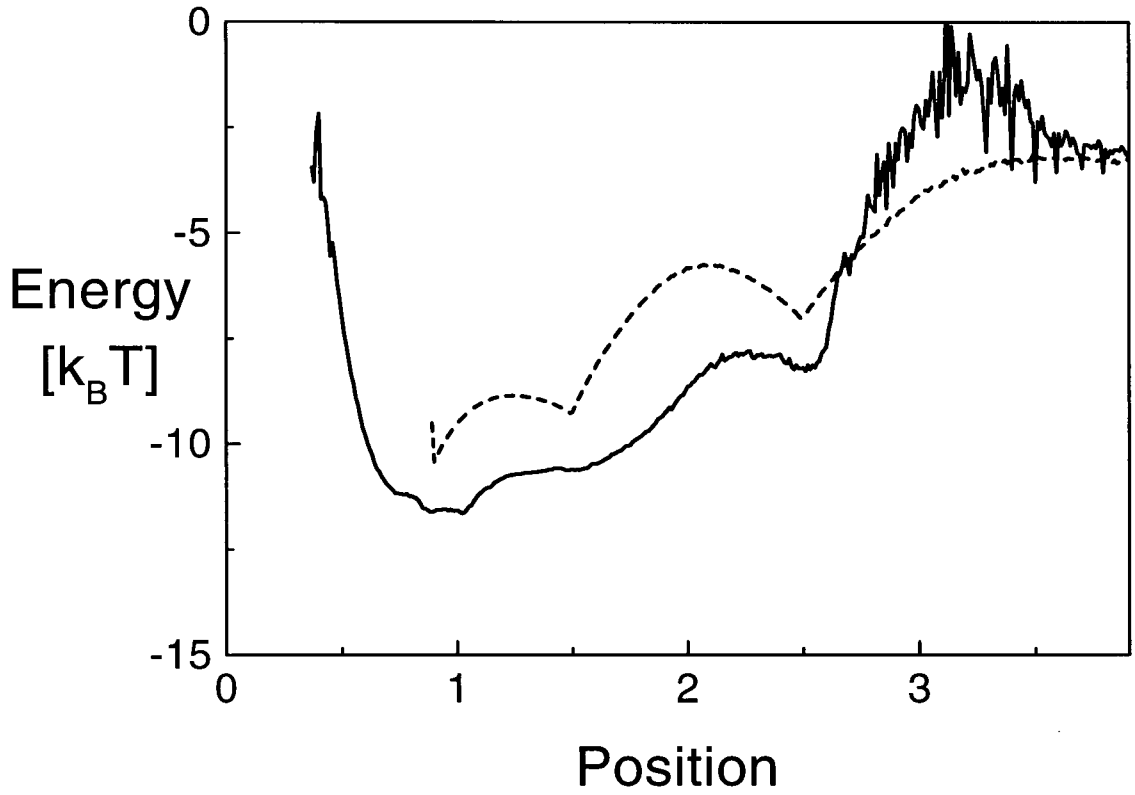

Figure 13.29: Renormalization of Potential by Fluctuations.
Frozen (dashed) and finite temperature (solid) approximations to the potentials of a small number of atom simulation with differential bonding potentials between the test particle and the rings of the simulation. By frozen it is meant that the can atoms were held stationary in their initial, well defined cylindrical geometry. Note the increase in barrier height in the central region due to fluctuations in the finite temperature simulation. The position is in units of the diameter of an atom of the can.

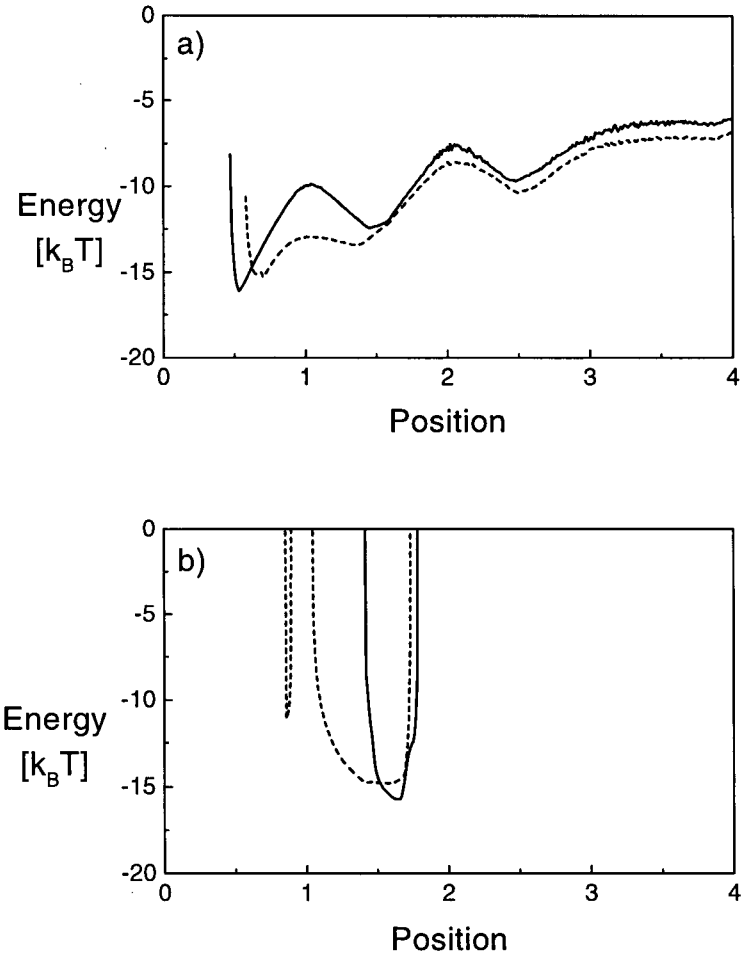

Figure 13.30: Randomly Selected Configuration Potentials.
Four different potentials due to randomly selected configurations about a starting configuration, the frozen potential of figure 13.29 . In a) two cases show a close correspondence to the starting frozen potential of figure 13.29. In b) two other cases present infinite barriers to the test particle's escape due to the frozen fluctuation.

simulation was run for a period of time (100,000 simulation steps) to allow the can to fluctuate. The can was then trapped into a random configiration and the its potential energy profile determined. In figure 13.30a, variations are found from the zero temperature starting potential (two such cases shown). Figure 13.30b shows that some fluctuations freeze in infinite barriers to the particles escape (two such cases shown). Extraction of the particle from such infinite barrier frozen configurations was impossible. Allowing fluctuation during extraction removed such anamolous barriers as in figure 13.29.

The renormalization effect of the fluctuations will mostly be absent in MD simulations done at extreme speeds. The back bone of an extended molecule will not be able to relax during the nanosecond of run time through which the bond must rupture. Hence, the MD bond failures are an approximation to the strength of the bond in a nearly *frozen* fluctuation about the starting position, taken from x-ray data.

Figure 13.31 shows the strength during bond failure from the frozen and finite temperature simulations of figure 13.29. Note the shift in the curves translates into a change in barrier energy of 2 k_BT. This corresponds to the increase in the energy barrier at the position of the center of the outermost ring of the can (at a position of about 3 can atom diameters on figure 13.29) region due to the inclusion of fluctuations in the finite temperature simulations.

The results of the small-number-of-atom simulation underline the importance of fluctuations and the rate of loading on the results obtained from the computational experiments. Comparison between ultra-fast all atom molecular dynamics simulations and laboratory time scale experiments requires caution. The small-number-of-atom simulation allows comparison over a large range of loading rates. Study of the effects of fluctuation induced steric effects can be done for a variety of potentials. Also, simple changes to the can allows one to evaluate the effects of extraneous flaps and loops to bonding potentials, thus more closely approximating an actual bonding situation, but

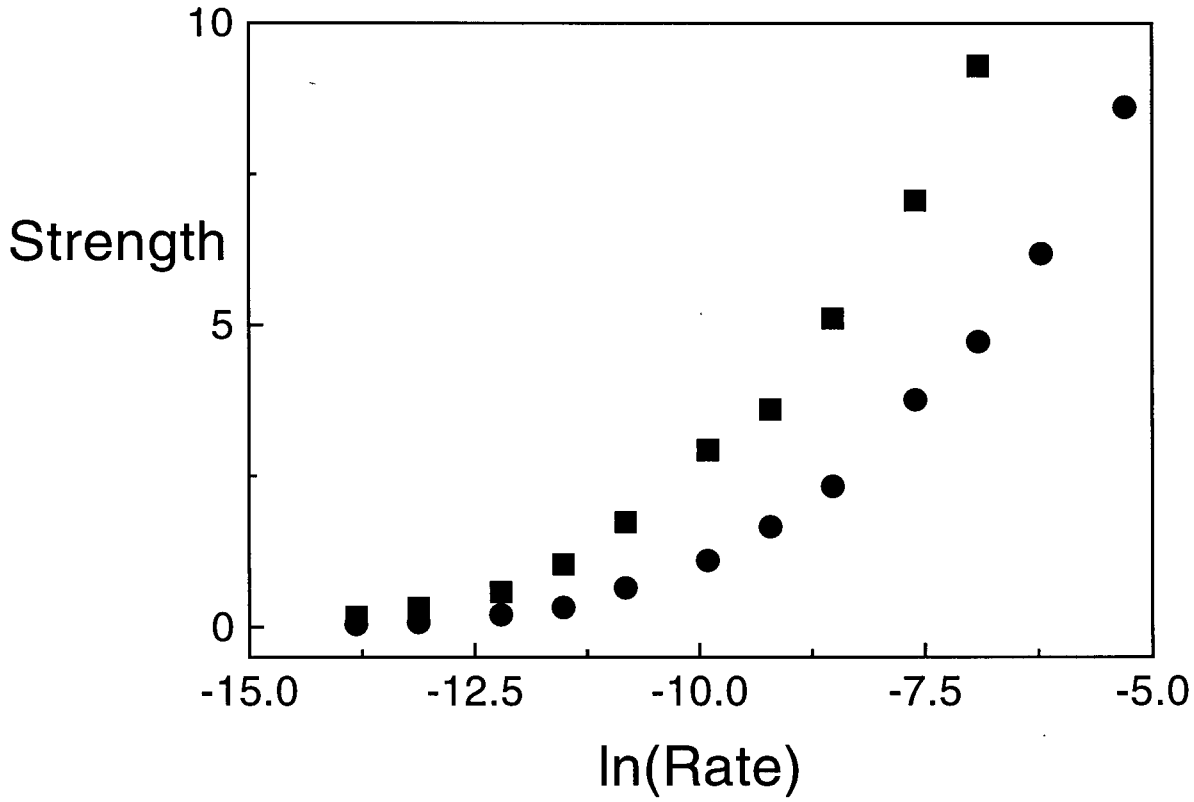

Figure 13.31: Comparison of Strength at Frozen and Finite Temperatures.
Strength to remove the test particle from the frozen (circles) and finite temperature (squares) simulation. The shift in rate for a given strength implies an increase in barrier height of 2 k_BT for the finite temperature simulation (as seen in at a position of 3 can atom diameters figure 13.29). Strength is in units of k_BT/a and the loading rate is in units of $k_BT/a\Delta t$ where a is a can atom diameter and Δt is an arbitrary time scale.

retaining a simplicity to span a wide range of loading rates.

Chapter 14

Multiple Bond Failure

One can easily extend the theory for single bond failure to the realm of multiple bonding. From chapter 12, the offrate of any single bond follows the general form

$$\nu = \nu_0 g(f) e^f \tag{14.66}$$

where f is made dimensionless by the thermal force scale f_β and $g(f)$ depends on the bonding potential, *e. g.*

$$g(f) = \begin{cases} \sqrt{f} & \text{(IPL)} \\ f & \text{(HW)} \end{cases} \tag{14.67}$$

for the inverse power law (IPL) and harmonic well (HW) geometries. The probability density for bond failure at a time, t, is set as the product of the offrate, $\nu(t)$ and the survival probability $e^{\int_0^t \nu(t')dt'}$ as

$$P(t) = \nu(t) e^{-\int_0^t \nu(t')dt'} \tag{14.68}$$

Thus if the load is increased linearly in time $f = \dot{f}t$, the probability density for failure at a force f is given by

$$P(f) = \frac{\nu(f)}{\dot{f}} e^{-\int_0^f \nu(f')df'/\dot{f}} \tag{14.69}$$

The naive view of multiple bond failure is that n bonds fail with an n-fold increase in strength. Due to the stochastic nature of bond rupture, the time dependence of the failure is essential. Three simple scenarios will be examined for failure of multiple bonds: 1) serial bonding, serial failure — like a string of bonds where a single bond failure ruptures

the linkage, 2) parallel bonding, sequential failure — a field of bonds that rupture like a zipper unzips, 3) parallel bonding, random deletion — a field of bonds that all share the load equally. Note that in the case 3) rebonding of already failed bonds has not been taken into account. This assumption is made considering that under force the bonding species are stretched prior to failure. After failure, there recoil would lessen the likelihood of rebonding. Each allowed situation has a different effect on the adhesive strength. These effects will be manifested through shifts in the peak strength $f^\star$ and in changes to the width of the probability distributions. Each of the three bonding scenarios will be considered separately in the next sections. The consequences and applicability of each scenarios are discussed.

14.1 Serial Loading — Serial Failure

The case of a series of weak physical bonds beginning and ending with a single strong bond occurs frequently in experimental situations. Streptavidin-biotin bond strength measurements have been performed by bonding a biotinylated molecule to both the force probe tip and substrate base (Florin *et al.*, 1994; Lee *et al.*, 1994; Moy *et al.*, 1994; Merkel *et. al.*, 1998). Here a streptavidin or avidin molecule bridging biotins linked to opposing sides (streptavidin and avidin both have four biotin binding pockets). The system consists of two equal bonds that can break and sever the linkage. The question arises as to what the strength of such a series implies about the single bond under investigation.

Consider a series of n identical bonds. The rate of loading is equal for all bonds along the chain. Failure occurs as any single bond dissociates. As such the frequency of failure of the chain is increased n-fold. The probability density for failure at a force f is given by

$$P(f) = (n\nu(f)/\dot{f}) \exp(-1/\dot{f} \int_0^f n\nu(f')df') \tag{14.70}$$

The factor n can be associated with the fundamental frequency ν_0 contained in $\nu(f)$. The result is the same as expected for the single bond failure with the fundamental frequency increased n-fold. This shifts the unitless rate to $r_f = \dot{f}/(n\nu_0 f_\beta)$. Figure 14.32 shows the consequence of this for a typical set of parameters using the frequency of failure $\nu(f) = \nu_0 f/f_\beta \exp(f/f_\beta)$ as an example.

Thus a set of experiments on a chain of n identical bonds will be indistinguishable from a single bond failure except that the fundamental frequency will be increased n-fold. With no *a priori* knowledge of the fundamental frequency this effect will be unnoticed and it will be assumed that the single bond is weaker at a given rate of loading than in reality.

14.1.1 Molecular Switch

A special case of the serial geometry is that of 2 non-identical bonds in series. Normalizing all variables by the parameters of bond 1 $(\nu_{01}, f_{\beta 1})$, the probability densities for failure of either bond is given by

$$P(f) = \frac{\nu_1(f) + \nu_2(f \cdot f_{12})/\nu_{12}}{\dot{f}} \exp\left(-1/\dot{f} \int_0^f (\nu_1(f') + \nu_2(f' \cdot f_{12})/\nu_{12})\, df'\right) \quad (14.71)$$

introducing the ratio of thermal forces $f_{12} \equiv f_{\beta 1}/f_{\beta 2}$ and frequencies $\nu_{12} \equiv \nu_{01}/\nu_{02}$. Of interest is which bond will fail first during loading. If $\nu_{12} \gg 1$ and $f_{12} \ll 1$, then bond 1 is weaker than bond 2 at all rates and bond 1 will always be the dominant bond to dissociate. If $\nu_{12} \gg 1$ and $f_{12} \gg 1$, then the weaker bond at slow rates of loading is bond 1 but at high rates is bond 2. There is a rate dependent crossover as to which bond is more likely to fail.

Figure 14.33 shows the crossover in strength for a force dependence of the frequency of $\nu(f) = \nu_0 f/f_\beta \exp(f/f_\beta)$ for both bonds. At low rates, bond 1 is the dominant bond to fail. The probability distribution of the failure strength of the system is shown in

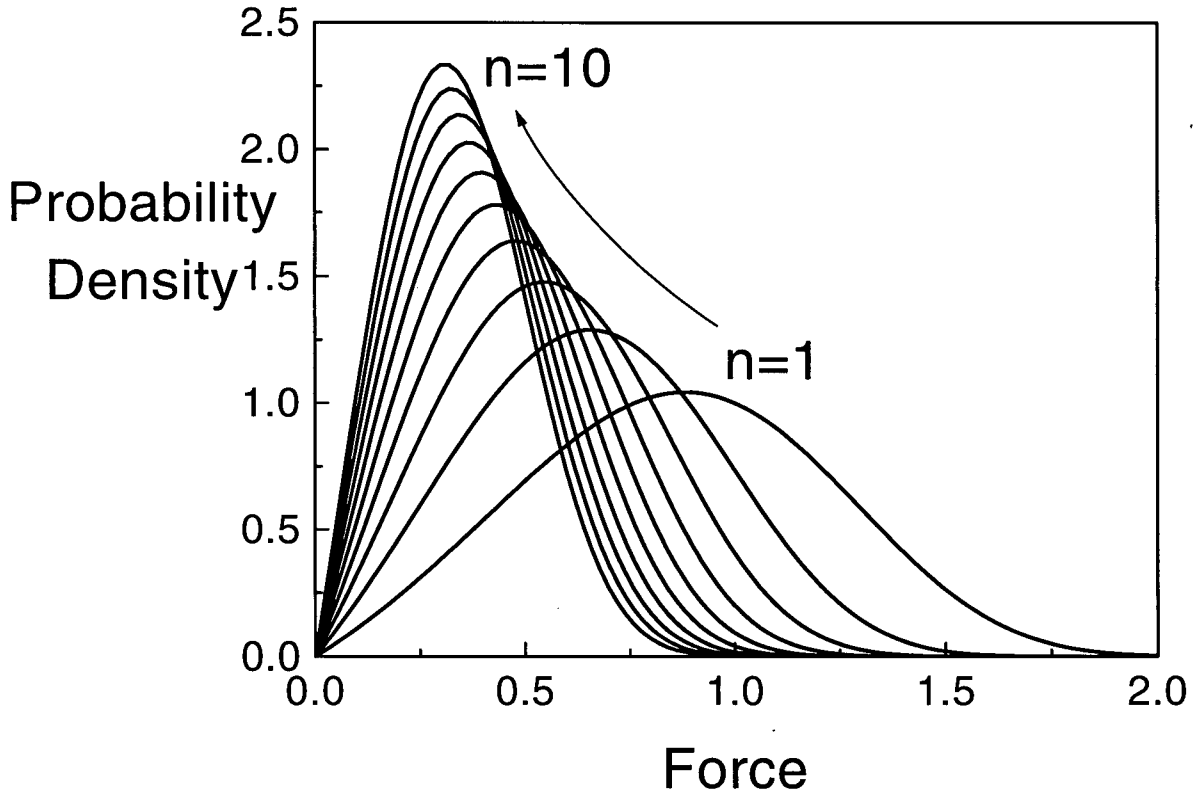

Figure 14.32: Strength Probability Density for Failure of Serial Bonds.
As the number of identical bonds, n, increases, the strength of the chain weakens. Force is in units of the thermal force, f_β. The example uses a frequency of failure that follows $\nu(f) = \nu_0 f/f_\beta \exp(f/f_\beta)$

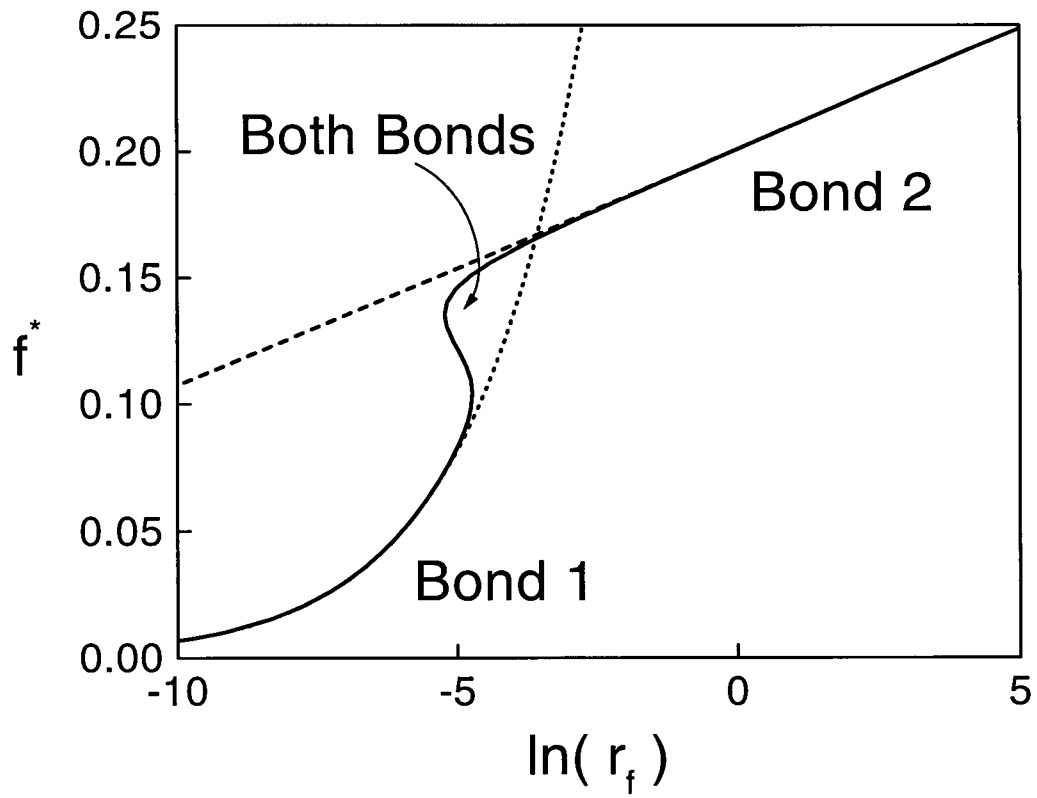

Figure 14.33: Strength of a Molecular Switch.
Shown is the strength, $f^\star$ in units of $f_{\beta 1}$, as a function of the loading rate, r_f in units of $f_{\beta 1}\nu_{01}$, of bond 1 (dotted), bond 2 (dashed) and a chain of both bonds. At low loading rates, bond 1 fails most likely. At high loading rates, bond 2 fails most likely. The crossover region can smoothly or discontinuously (as shown) change between the two bonds. The force dependence of the frequency for both bonds was set to $\nu(f) = \nu_0 f/f_\beta \exp(f/f_\beta)$.

figure 14.34 where at low rates a simple peak is formed due to bond 1. At high rates, bond 2 will be the dominate bond to dissociate as predicted in figure 14.33. The strength probability distributions in figure 14.34 at high rates also show a simple, single peak as a result of the failure of bond 2.

In the crossover region, determination of which bond fails is non-trivial. At some values of the parameters f_{12} and ν_{12} the strength, defined as a peak in the probability distribution, continues smoothly at low rates from following bond 1 to that of bond 2 at high rates. At other values of the parameters there exists a *two-phase* region where two peaks coexist in the strength probability density as in figure 14.34.

Likening which bond fails to a thermodynamic transition where the phase is represented by the bond most representative of the visible peak, one can obtain a $\ln(f_{12})$-$\ln(\nu_{12})$-$\ln(r_f)$ phase diagram as in figure 14.35. The figure also shows two slices through the phase diagram: b) at constant f_{12} and c) at constant ν_{12}, to aid in viewing the three dimensional phase diagram. The extremal regions of the plot along the r_f axis are easily attributed to a single bond.

Inside the wing shaped boundary of figure 14.35 the strength histogram has two peaks indicating the two-phase region. Thus, as the rate is increased, if the parameters go through this two-phase region, it is like a first order phase transition. If the parameters are such that the two phase region is bypassed, then there is a second order transition in which the strength cannot be assigned to either bond through the transition region.

The rate-dependent switch can be implemented by nature as a rate of loading monitor. Two adherent bodies can have a binary switch to determine if separation occurs with rates of loading greater or less than a value predetermined by the adhesion molecule's physical properties. An internal signal pathway could be activated to repair damage due to extreme separation rates.

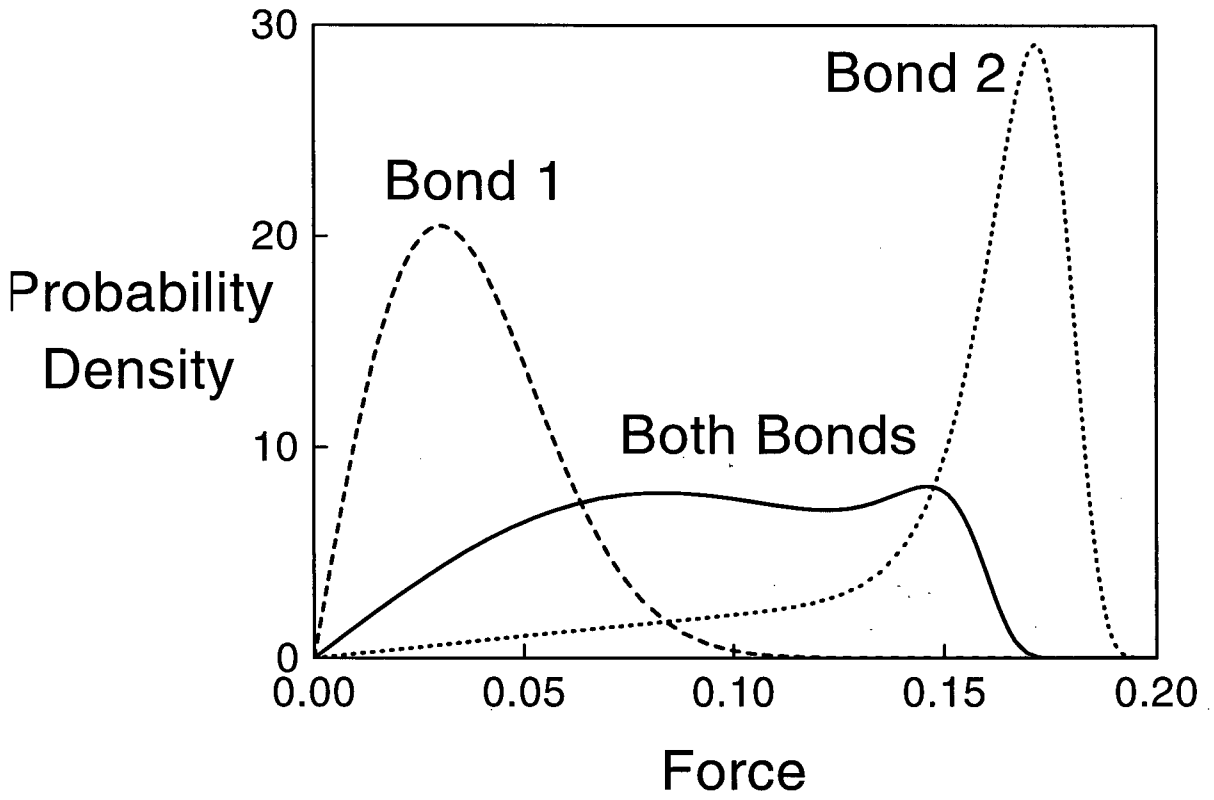

Figure 14.34: Strength Probability Density for a Molecular Switch.
At low loading rates, bond 1 fails most likely. At high loading rates, bond 2 fails most likely. At the crossover rate, a *two phase* region may occur where two peaks are visible in the probability density. Force is in units of the thermal force, $f_{\beta 1}$. The force dependence of the frequency for both bonds was set to $\nu(f) = \nu_0 f/f_\beta \exp(f/f_\beta)$.

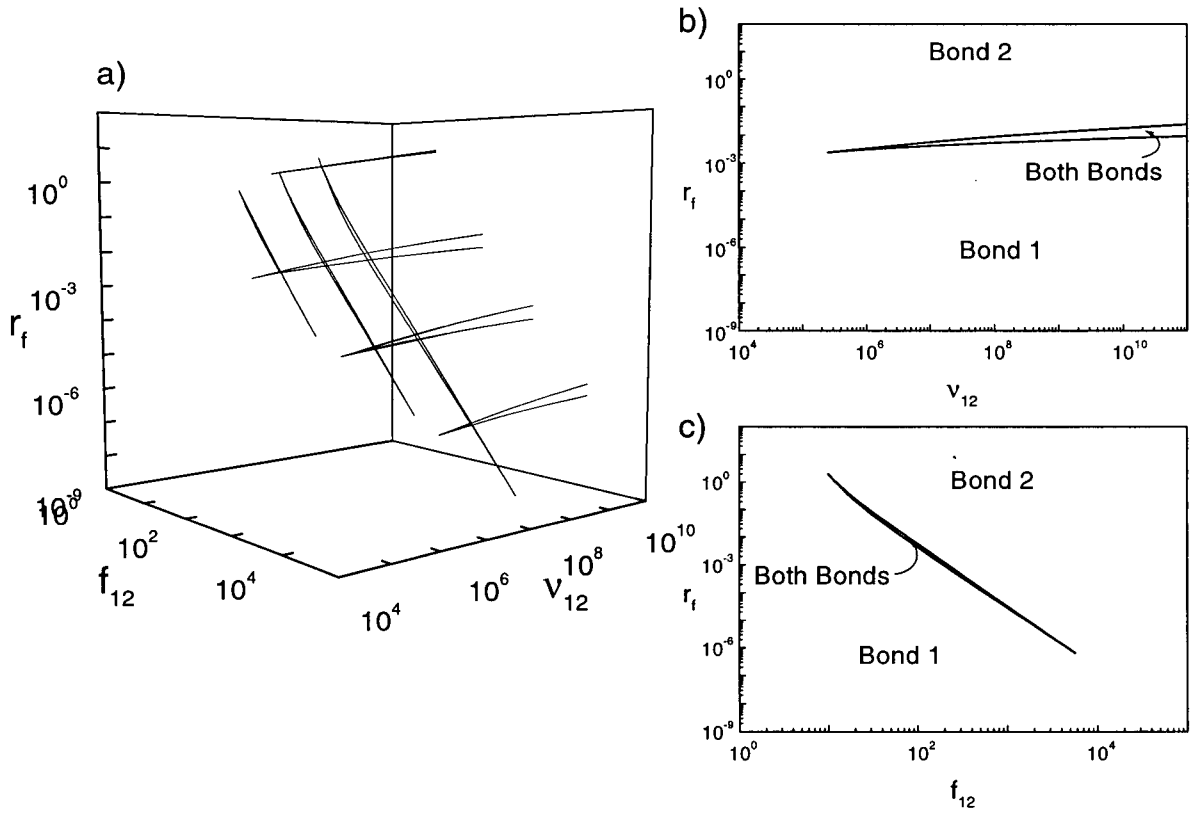

Figure 14.35: Phase Diagram of the Molecular Switch.
a) $\ln(f_{12})$-$\ln(\nu_{12})$-$\ln(r_f)$ phase diagram with b) constant ratio of thermal forces f_{12} and c) constant ratio of frequencies ν_{12} slices shown for clarity. Trajectories that traverse the wing structure undergo a first order transition between bonds. Trajectories that bypass the *two phase* region undergo a continuous, second order transition between bonds. The loading rate, r_f is in units of $f_{\beta 1}\nu_{01}$. The force dependence of the frequency for both bonds was set to $\nu(f) = \nu_0 f/f_\beta \exp(f/f_\beta)$.

14.2 Parallel Loading — Random Deletion

Consider the case where there are n individual bonds bridging a gap between a probe and substrate. Assume that all bonds are identical and loaded equally and simultaneously. Experimental procedures driving a probe tip forcibly into a softer substrate may form such patches upon retraction (Florin *et al.*, 1994; Moy *et al.*, 1994; Williams *et al.*, 1996). Initially, the load on each bond is $1/n$ of the total applied load but as the bonds are randomly deleted by failure, the load on the remaining bonds increases proportionately. The force measured experimentally is the force reached as the final bond dissociates. As each bond fails, the load on the remaining bonds increases accordingly. For n bonds, the probability of the final bond rupturing at force f is the joint density

$$P_N(f) = \int_{f_1=0}^{f} df_1 \cdots \int_{f_{N-1}=f_{N-2}}^{f} df_{N-1} \frac{N\nu(f_1/N)}{\dot{f}} \exp\left(-\int_0^{f_1/N} N\nu(f')df'/(\dot{f}/N)\right) \cdots \frac{\nu(f_N)}{\dot{f}} \exp\left(-\int_{f_{N-1}}^{f} \nu(f')df'/\dot{f}\right) \quad (14.72)$$

Figure 14.36 displays the effect of increasing bond number on the probability density for a force dependence of the frequency of $\nu(f) = \nu_0 f/f_\beta \exp(f/f_\beta)$. As expected, the predicted strength increases with number of bonds. It does not however increase linearly as the number of bonds. It is wrong to expect that n bonds that fail in parallel will have a strength n times that of an individual bond. The complete loading history of the final bond has to be considered. The width of the peak is thin relative to its strength, consistent with the strength being determined by the last bond that fails, regardless which bond it is.

14.3 Parallel Loading — Sequential Failure

The last configuration considered is a set of bonds bridging between a probe and substrate in the parallel geometry of the last section that fail as a zipper would unzip. Peeling

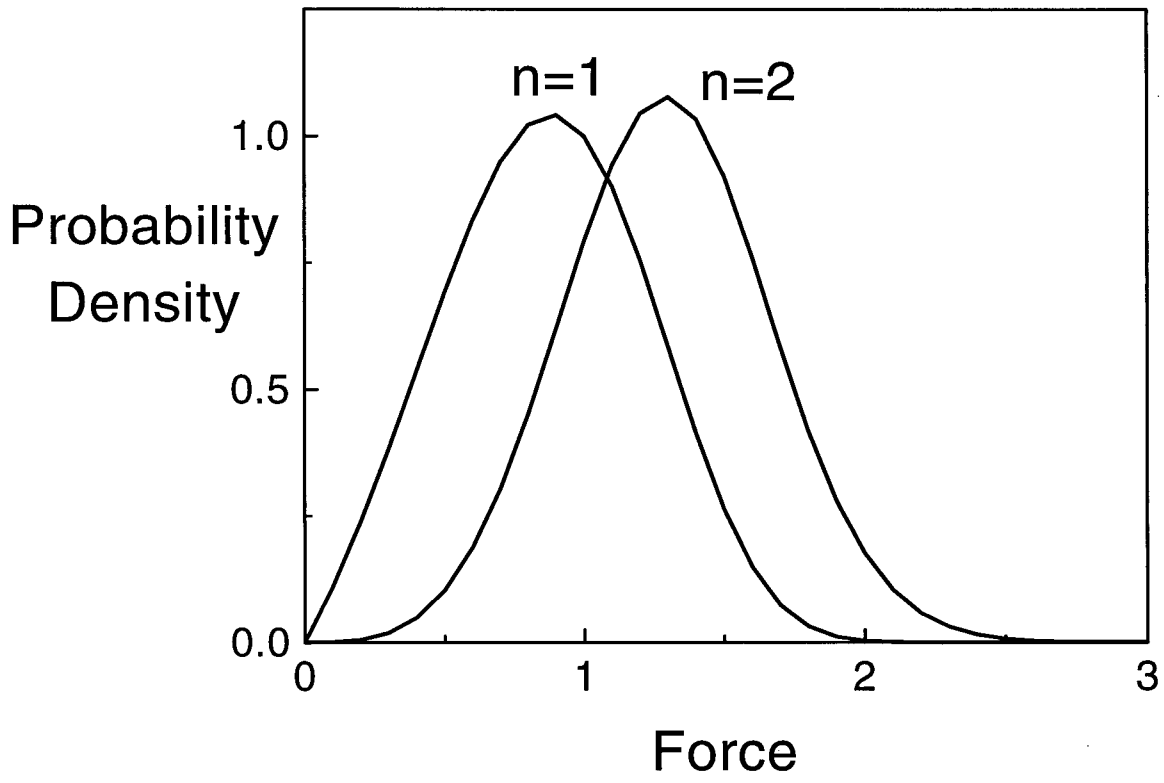

Figure 14.36: Parallel Failure of a Field of Bonds.
An increase in the number of parallel bonds that are randomly deleted increases the strength of the system but thins the distribution relative to the strength. The increase in strength is not a simple multiple of the number of bonds formed. Force is in units of the thermal force, f_β. The force dependence of the frequency $\nu(f) = \nu_0 f/f_\beta \exp(f/f_\beta)$ was used.

an adherent body from a substrate involves this mechanism. A slanted or pyramidal probe adherent through point contacts to a flat substrate will also contain bonds that fail serially. The characteristic of this configuration is that a single bond takes the entire load until its failure. Then a neighboring bond takes the entire load (neglecting recoil of the force probe after the first bond fails).

The probability density for n identical bonds, for failure of the last bond, defining the strength, at a force f is

$$P_N(f) = P_1(f)/\dot{f}^{(N-1)} \int_{f1=0}^{f} df_1 \cdots \int_{f_{N-1}=0}^{f} df_{N-1} \nu(f_1) \cdots \nu(f_{N-1}) \tag{14.73}$$

where $P_1(f)$ is the probability density for a single bond failure. For a harmonic bonding potential this is

$$P_N(f) = P_1(f)/r_f^{(N-1)} \cdot (f \cdot \exp(f) + 1 - \exp(f))^{(N-1)}/(N-1)! \tag{14.74}$$

Figure 14.37 displays the effect of the number of bonds on the force at dissociation probability.

The maximum in the probability distribution only slightly increases as the number of bonds increase. The striking feature of the distribution is the thinning as the number of bonds increase. The breadth of the distribution combined with the peak strength is a signature of a multiple bond peeling process.

14.4 Summary

The complex nature of bond failure in the presence of multiple bonds presents complications to the analysis of bond strength. The width of the bond strength probability distributions, more than the strength, yields a signature of parallel multiple bonds. A thinning of the peak with respect to the strength is a sign of parallel multiple bonds.

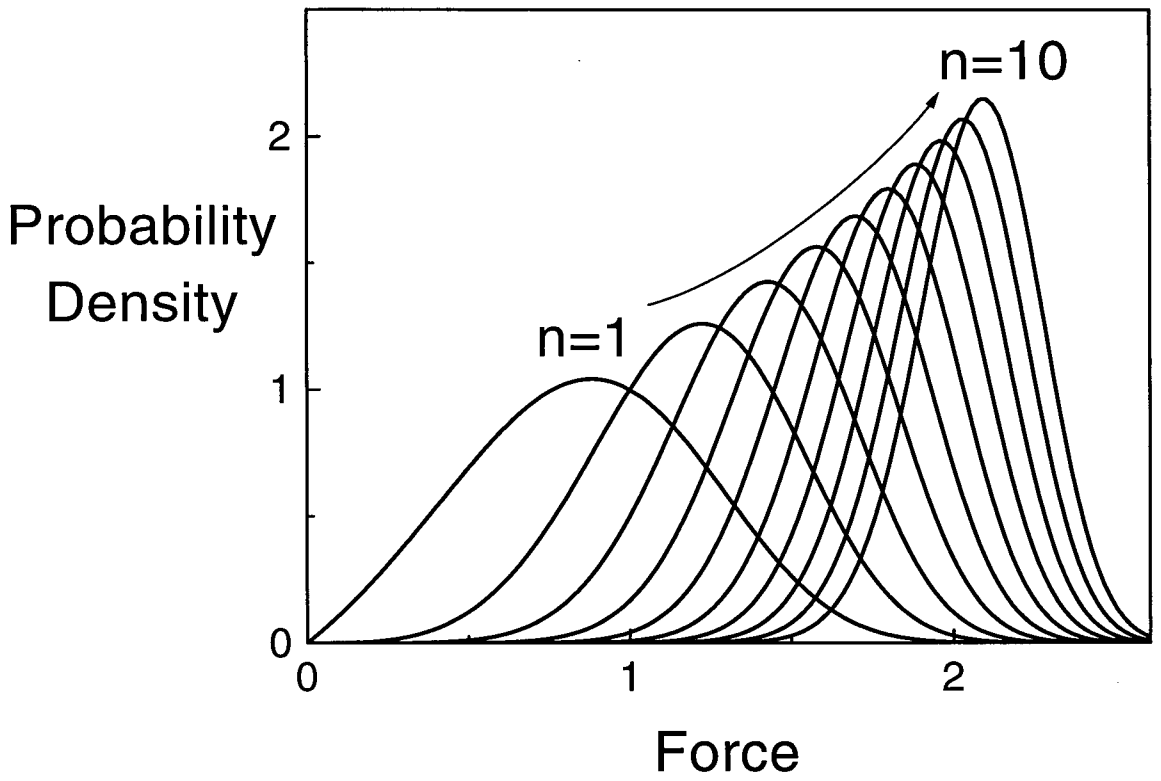

Figure 14.37: Sequential Failure of a Field of Bonds.
A slight increase in strength is seen as the number of bonds that fail in sequence increases. Thinning of the peak signifies the parallel geometry. Force is in units of the thermal force, f_β. The force dependence of the frequency $\nu(f) = \nu_0 f/f_\beta \exp(f/f_\beta)$ was used.

For bonds linked in serial, caution must be taken in determining the bond that is failing. The bond that is weakest at one rate of loading may not be weakest at another rate of loading. The change in strongest bond with rate of loading when two bonds are present defines a molecular switch that monitors the rate of loading. A cell can monitor its separation from an adjoining cell through a molecular switch of this type.

Chapter 15

Conclusions

The measurement of the strength of weak molecular bonds has been thoroughly studied. Until now, groups have measured bond strength as a unitary value, independent of the measurement method (Evans *et al.*, 1991; Florin *et al.*, 1994; Lee *et al.*, 1994; Moy *et al.*, 1994; Williams *et al.*, 1996). Bond dissociation is a far from equilibrium process and is thus time dependent. As such, the rate of application of force in any experimental technique becomes an important determinant of the strength of the linkage under study.

The application of force to aid in bond dissociation tends to tilt the energy landscape, thus speeds up the rate of dissociation. Applied force may have a three-fold effect — 1) to decrease the bonding length, 2) to lower the barrier energy and 3) to thin the barrier along the reaction coordinate. The effects due to force combine to produce three regions of loading rate dependent strength. At low loading rates there can be a critical loading rate, exposed through smart Monte Carlo simulation, below which the strength, defined as the most probable force of failure, vanishes. Above the critical loading rate, a slow-loading regime displays a polynomial dependence of loading rate on strength. A universal fast regime is entered where the drop in barrier height dominates the likelihood of dissociation, causing a logarithmic dependence of loading rate on strength. As the rate of loading is further raised, an ultrafast regime is entered where the barrier is quickly overwhelmed and any increase in force is due to dissipative effects. Such a regime is exposed in a simulation in which the transition state is stationary.

Monte Carlo simulations based on the Langevin equation verify these predictions over

8 orders of magnitude in loading rate for several bonding potentials. Furthermore, simulation demonstrates the effect of dimensionality. As the dimension of the binding space is increased, the critical rate increases. At higher loading rates, the one dimensional theory fits the three dimensional simulation exposing that the application of tension focuses the escape along the direction of the force. Coupling the bonded particles hydrodynamically tends to have the similar effect of increasing the dimensionality, increasing the critical loading rate.

Knowledge of the rate dependence of strength of molecular linkages demands an experimental apparatus with pico-Newton sensitivity and a wide range of easily accessible loading rates. The two instruments of Part I have the required control and range to perform a force spectroscopy on a linkage under study. Through this a window into the binding potential is opened.

Taken together, a new view of strength in weak biochemical linkages appears. The strength is a dynamic characteristic of the bond. Experimental protocol must exploit this to determine the underlying potential. This is not limited to the failure of two linked but distinct molecules. Recent work has been done to unfold the muscle protein titin (consisting of 244 nearly identical Ig-like and fibronectin-like domains that can individually unfold under stress to lengthen the protein by $\sim$ 30 nm) under tension (Kellermayer *et al.*, 1997; Rief *et al.*, 1997; Tskhovrebova *et al.*, 1997). In such a system, the folded Ig domain of titin is stabilized by a hydrogen bond network between 7 β strands. The unfolding is mediated by the failure of the hydrogen bonds between strands (Lu *et. al.*, 1998). This can be modeled as the failure of the hydrogen bonds, although account must be taken of the multiple bonding pattern and for any mechanical advantage that can be gained through the unfolding of the structure. A logarithmic rate dependence in the strength required to unfold individual titin domains was demonstrated.

Bibliography

[1] Ashkin, A., Schutze, K., Dziedzic, J. M., Euteneuer, U. and Shliwa, M. (1990) Force Generation of Organelle Transport Measured in vivo by an Infrared Laser Trap. *Nature* **348**, 346–348.

[2] Batchelor, G. K. (1976) Brownian Diffusion of Particles with Hydrodynamic Interaction. *J. Fluid Mech.* **74**, 1–29.

[3] Bell, G. (1978) Models for the Specific Adhesion of Cells to Cells. *Science* **200**, 618–627.

[4] Binnig, G., Quate, C. F. and Gerger, Ch. (1986) Atomic Force Microscope. *Phys. Rev. Let.* **56**, 930–933.

[5] Boal, D. H. (1994) Computer Simulation of a Model Network for the Erythrocyte Cytoskeleton. *Biophys. J.* **67**, 521–529.

[6] Bull, B. S., Weinstein, R. S. and Korpman, R. A. (1986) On the Thickness of the Red Cell Membrane Skeleton: Quantitative Electron Microscopy of Maximally Narrowed Isthmus Regions of Intact Cells. *Blood Cells* **12**, 25–42.

[7] Chilkoti, A. and Stayton, P.S. (1995) Molecular Origins of the Slow Streptavidin-Biotin Dissociation Kinetics. *J. Am. Chem. Soc.***117**, 10622–10628.

[8] Derjaguin, B (1934). *Kolloid-Z.* **69**, 155.

[9] Doi, M. and Edwards, S.F. (1986) *Theory of Polymer Dynamics*, Clarendon Press, Oxford.

[10] Doll, J. D. and Dion, D. R. (1976) Generalized Langevin Equation Approach for Atom/Solid-Surface Scattering: Numerical Techniques for Gaussian Generalized Langevin Dynamics. *J. Chem. Phys.* **65**, 3762–3766.

[11] Ermak, D. L. (1975a) A Computer Simulation of Charged Particles in Solution. I. Technique and Equilibrium Properties. *J. Chem. Phys.* **62**, 4189–4196.

[12] Ermak, D. L. (1975b) A Computer Simulation of Charged Particles in Solution. II. Polyion Diffusion Coefficient. *J. Chem. Phys.* **62**, 4197–5003.

[13] Evans, E. A. (1973a) A New Material Concept for Red Cell Membranes. *Biophys. J.* **13**, 926–940.

[14] Evans, E. A. (1973b) New Membrane Concept Applied to the Analysis of Fluid Shear and Micropipet Deformed Red Blood Cells. *Biophys. J.* **13**, 941–954.

[15] Evans, E. and Skalak, R. (1980) Mechanics and Thermodynamics of Biomembranes. CRC Press, Boca Raton, Florida, USA. 254 pp.

[16] Evans, E. A. (1983) Bending Elastic Modulus of Red Cell Membrane derived from Buckling Instability in Micropipet Aspiration Tests. *Biophys J.* **43**, 27–30.

[17] Evans, E., Berk, D. and Leung, A. (1991) Detachment of Agglutinin Bonded Red Blood Cells: I. Forces to Rupture Molecular-point Attachments. *Biophys. J.* **59**, 838–848.

[18] Evans, E., Merkel, R., Ritchie, K., Tha, S. and Zilker, A. (1994) Picoforce Method to Probe Submicroscopic Actions in Biomembrane Adhesion. *In* Studying Cell Adhesion. P. Bongrand, P. M. Claesson and A. S. G. Curtis editors. Springer-Verlag, Berlin. 125–140.

[19] Evans, E., Ritchie, K. and Merkel, R. (1995) Sensitive Force Technique to Probe Adhesion and Structural Linkages at Biological Interfaces. *Biophys J.* **68**, 2580–2587.

[20] Evans, E. and Ritchie, K. (1997) Dynamic Strength of Molecular Adhesion Bonds. *Biophys J.* **72**, 1541–1555.

[21] Eyring, H. (1935) The Activated Complex in Chemical Reactions. *J. Chem. Phys* **3**, 107–115.

[22] Finer, J. T., Simmons, R. M. and Spudich, J. A. (1994) Single Myosin Molecule Mechanics: Piconewton Forces and Nanometre Steps. *Nature* **368**, 113–119.

[23] Fischer, T. M. (1988) Role of Spectrin in Cross Bonding of the Red Cell Membrane. *Blood Cells* **13**, 377–394.

[24] Florin, E.-L., Moy, V. T. and Gaub, H. E. (1994) Adhesive Forces Between Individual Ligand-receptor Pairs. *Science* **264**, 415–417.

[25] Grubmuller, H., Heymann, B. and Tavan, P. (1996) Ligand Binding: Molecular Mechanics Calculation of the Streptavidin-biotin Rupture Force. *Science* **271**, 997–999.

[26] Hänggi, P., Talkner, P. and Borkovec, M. (1990) Reaction-rate Theory: Fifty Years After Kramers. *Rev. Mod. Phys.* **62**, 251–341.

[27] Hoh, J. H., Cleveland, J. P., Prater, C. B., Revel, J.-P. and Hansma, P. K. (1992) Quantized Adhesion Detected with the Atomic Force Microscope. *J. Am. Chem. Soc.* **114**, 4917—4918.

[28] Ishijima, A., Doi, T., Sakurada, K. and Yanagida, T. (1991) Sub-piconewton Force Fluctuations of Actomyosin in vitro. *Nature* **352**, 301–306.

[29] Israelachvili, J. N. and Adams, G. E. (1978) Measurement of Forces between Two Mica Surfaces in Aqueous Electrolyte Solutions in the Range 0–100 nm. *J. Chem. Soc. Faraday Trans. I* **74**, 975–1001.

[30] Izrailev, S., Stepaniants, S., Balsera, M., Oono, Y. and Shulten, K. (1997) Molecular Dynamics Study of Unbinding of the Avidin-biotin Complex. *Biophys. J.* **72**, 1568–1581.

[31] Kellermayer, M., Smith, S., Granzier, H., and Bustamante, C. (1997) Folding-Unfolding Transition in Single Titin Modules Characterized with Laser Tweezers. *Science* **276**, 1112–1116.

[32] Kuo, S. C. and Sheetz, M. P. (1993) Force of Single Kinesin Molecules Measured with Optical Tweezers. *Science* **260**, 232–234.

[33] Kramers, H. A. (1940) Brownian Motion in a Field of Force and the Diffusion Model of Chemical Reactions. *physica (Utrecht)* **7**, 284–304

[34] Landau, L. D. and Lifshitz, E. M. (1986) *Theory of Elasticity,* 3rd *Edition.* Pergamon Press, Willowdale, Ontario, Canada.

[35] Lee, G. U., Kidwell, D. A. and Colton, R. J. Sensing Discrete Streptavidin-biotin Interactions with Atomic Force Microscopy. *Langmuir* **10**, 354–357.

[36] Lu, H., Isralewitz, B., Krammer, A., Vogel, V. and Schulten K (1998) Unfolding of Titin Immunoglobulin Domains by Steered Molecular Dynamics Simulation. *Biophys. J.* (In press).

[37] Merkel, R., Nassoy, P., Leung, A., Ritchie, K. and Evans, E. (1998) Using Dynamic Force Spectroscopy to Explore Energy Landscapes of Receptor-Ligand Bonds. (*In preparation*).

[38] Metropolis, N. and Ulam, S. (1949) The Monte Carlo Method. *J. Am. Stat. Ass.* **44**, 335–341.

[39] Metropolis, N., Rossenbluth, A. W., Rossenbluth, M. N., Teller, A. H. and Teller, E. (1953) Equation of State Calculations by Fast Computing Machines. *J. Chem. Phys.* **21**, 1087–1092.

[40] Mohandas, N. and Evans, E. (1994) Mechanical Properties of the Red Cell Membrane in Relation to Molecular Structure and Genetic Defects. *Annu. Rev. Biophys. Biomol. Struct.* **23**, 787–818.

[41] Moy, V. T., Florin, E.-L. and Gaub, H. E. (1994) Intermolecular Forces and Energies Between Ligands and Receptors. *Science* **266**, 257–259.

[42] Nassoy, P., Bastos, D., Leung, A. and Evans, E. (1998) Chemical Design of Probe Tips to Test Adhesion Molecules. (*In preparation*).

[43] Rädler, J. and Sackmann, E. (1992) On the Measurement of Weak Repulsive and Frictional Colloidal Forces by Reflection Interference Contrast Microscopy. *Langmuir* **8**, 848–853.

[44] Rädler, J. and Sackmann, E. (1993) Imaging Optical Thicknesses and Separation Distances of Phospholipid Vesicles at Solid Surfaces. *J. Phys. II France* **3**, 727.

[45] Radmacher, M., Tillmann, R. W., Fritz, M., Gaub, H. E. (1992) From Molecules to Cells: Imaging Soft Samples with the Atomic Force Microscope. *Science* **257**, 1900–1905.

[46] Rief, M., Gautel, M., Oesterhelt, F., Fernandez, J. M. and Gaub, H. E. (1997) Reversible Unfolding of Individual Titin Immunoglobulin Domains by AFM. *Science* **276**, 1109–1112.

[47] Rosebury, F. (1965) *Handbook of Electron Tube and Vacuum Techniques.* Addison-Wesley, Reading, MA, USA

[48] Rossky, P. J., Doll, J. D. and Friedman, H.L. (1978) Brownian Dynamics as Smart Monte Carlo Simulation. *J. Chem. Phys* **69**, 4628–4633.

[49] Savage, M. D., Mattson, G., Desai, S., Nielander, G. W., Morgensen, S. and Conklin, E. J. (1992) *Avidin-Biotin Chemistry: A Handbook.* Pierce Chemical Company, USA.

[50] Shaklai, N., Yguerabide, J. and Ranney, H. M. (1977) Interaction of Hemeglobin with Red Blood Cell Membranes as Shown by a Fluorescent Chromophore. *Biochem.* **16**, 5585–5592.

[51] Steck, T. L. (1974) The Organization of Proteins in the Human Red Blood Cell Membrane. *J. Cell Biol.* **62**, 1–19.

[52] Tskhovrebova, L., Trinick, J., Sleep, J. and Simmons, R. (1997) Elasticity and Unfolding of Single Molecules of the Giant Protein Titin. *Nature* **387**, 308–312.

[53] Turq, P., Lantelme, F. and Friedman, H. L. (1977) Brownian Dynamics: Its Application to Ionic Solutions. *J. Chem. Phys.* **66**, 3039–3044.

[54] Waugh, R. and Evans, E. A. (1979) Thermoelasticity of the Red Blood Cell Membrane. *Biophys. J.* **26**, 115–132.

[55] Williams, J. M., Han, T. and Beebe, Jr., T. P. (1996) Determination of Single-bond Forces from Contact Force Variances in Atomic Force Microscopy. *Langmuir* **12**, 1291–1295.